DOE/ER/14180--2

DE93 009759

APPLICATION OF MAGNETOMECHANICAL HYSTERESIS MODELING OF MAGNETIC TECHNIQUES FOR MONITORING NEUTRON EMBRITTLEMENT AND BIAXIAL STRESS

FIRST YEAR REPORT
June 1991 - June 1992

M.J. Sablik, H. Kwun, G. L. Burkhardt,
W.L. Rollwitz and D.G. Cadena

Southwest Research Institute
San Antonio, TX 78228-0510

January 31, 1993

PREPARED FOR THE U.S. DEPARTMENT OF ENERGY
UNDER GRANT NUMBER DE-FG05-91ER14180

DOE/ER/14180-2

APPLICATION OF MAGNETOMECHANICAL HYSTERESIS MODELING OF MAGNETIC TECHNIQUES FOR MONITORING NEUTRON EMBRITTLEMENT AND BIAXIAL STRESS

FIRST YEAR REPORT
June 1991 - June 1992

M.J. Sablik, H. Kwun, G. L. Burkhardt,
W.L. Rollwitz and D.G. Cadena

Southwest Research Institute
San Antonio, TX 78228-0510

January 31, 1993

PREPARED FOR THE U.S. DEPARTMENT OF ENERGY
UNDER GRANT NUMBER DE-FG05-91ER14180

EXECUTIVE SUMMARY

The objective of this project is to investigate experimentally and theoretically the effects of neutron embrittlement and biaxial stress on magnetic properties in steels, using various magnetic measurement techniques. If neutron embrittlement and biaxial stress can be measured via changes in magnetic properties, this should ultimately assist in safety monitoring of nuclear power plants and of gas and oil pipelines.

This first-year report addresses the issue of using magnetic property changes to detect neutron embrittlement. The magnetic measurements were all done on irradiated specimens previously broken in two in a Charpy test to determine their embrittlement. Measurements included: (1) hysteresis loop measurement of coercive force, permeability, and remanence; (2) Barkhausen noise amplitude; (3) higher order nonlinear harmonic analysis of a 1-Hz magnetic excitation; (4) magnetically-induced velocity change (MIVC) measurements; and (5) magabsorption measurements involving impedance changes in an RF coil due to the presence of an embrittled magnetic specimen. Specimens from the Indian Point 2 and DC Cook 2 reactors were used. More specimens were tested than in our earlier interim report. The study characterized many more specimens than in any previously reported study.

Our observations were that magnetic properties of the broken Charpy specimens from one of the reactors (D.C. Cook, 2) did not correlate well with fluence or embrittlement parameters, possibly due to metallurgical reasons. Correlation was better with the Indian Point 2 specimens, with the nonlinear harmonic amplitudes showing the best correlation (R^2~0.7). However, correlation was not good enough to sanction magnetic measurements on broken Charpy specimens as a method of measuring embrittlement.

The issue is not settled, however, because magnetic measurements would be useful only as a nondestructive test on unbroken specimens (so that the specimens could be reused later in surveillance capsules). In our tests, unbroken irradiated Charpy specimens were not used, and the Charpy impact produces residual stresses in the specimen which affect the magnetic properties in ways that cannot be easily tracked.

In addition, the Charpy test is a statistical test which extracts average embrittlement parameters for a set of specimens which individually are embrittled differently. This statistical variation in the specimens make it difficult to establish good correlation (R^2~0.9) between magnetic properties and embrittlement parameters. Finally, the magnetic properties of the individual specimens were not measured prior to irradiation, and thus no baseline measurements were available.

In the future, it is recommended that tests be done on unbroken irradiated Charpy specimens, for which magnetic characterization data prior to irradiation is available, if possible. The tests should include specimens from more reactors, with more fluence levels per reactor, and more specimens per fluence level.

The modeling was restricted to nonlinear harmonic amplitudes and Barkhausen noise amplitudes, but was able to produce one useful insight -- namely, that the magnetic property changes seen in the Indian Point data are similar to the magnetic changes that would be expected in the case of creep damage, suggesting that creep damage in steam pipes and neutron embrittlement in nuclear reactors are related problems.

Table of Contents

APPENDIX 1

Linear Correlation Coefficient

APPENDIX 2

Paper "Preliminary Studies of Magnetic NDE Techniques for Identifying Neutron Embrittlement of Pressure Vessel Steel", M. J. Sablik, H. Kwun, G. L. Burkhardt, and D. G. Cadena, from Proc. Quantitative NDE Conference, La Jolla, CA, July 1992.

APPENDIX 3

Paper "A Model for the Barkhausen Pulse Power Amplitude as a Function of Applied Field", M. J. Sablik, submitted to J. Appl. Phys., Jan. 1993.

LIST OF ILLUSTRATIONS

I. INTRODUCTION

This research project is investigating two areas of nondestructive evaluation (NDE) relating to safety in the energy industry:

> 1) the problem of nondestructively monitoring neutron embrittlement in nuclear pressure vessels; and
>
> 2) the problem of nondestructively detecting and quantifying high stress levels in gas and oil pipeline, where both hoop and longitudinal stresses coexist in a biaxial stress condition.

These research problems are important because of the need to ensure that failure of nuclear pressure vessels or of oil and gas pipeline does not occur.

In the case of problem (1), the steel nuclear pressure vessel is exposed to a spectrum of neutrons from the core of the reactor. It is the high energy (>1MeV) neutron irradiation, which over a long period of time, makes the steel brittle and susceptible to failure.[1] To monitor embrittlement, specimens of the reactor vessel steel are put in capsules which are hung between the pressure vessel wall and the thermal shield surrounding the core region of the reactor.[2] During reactor maintenenace periods, some of these specimens are removed and subjected to destructive "Charpy" tests[3] to determine the degree of their embrittlement. Since Charpy tests consume these specimens, a large number of specimens, sufficient to last over the expected design life of the vessel, are made at the time of plant construction and are installed in the reactor. If a nondestructive test were available, the tested specimens could be used again after the testing, and the surveillance program could be conducted more cost-effectively. The lifetime of the reactor could potentially be extended so long as the Charpy specimens, tested nondestructively after each operation period, do not exhibit dangerous embrittlement. Also, the nondestructive test could potentially be done on site.

In the case of problem (2), ground shifting can occur around pipeline due to settling or due to freezing and thawing as in Alaska or due to earthquakes as in California. This can cause high stress in pipeline which may endanger the safety of the line.[4] Also, exposed pipeline, uncovered due to shifting desert sands or due to wave action underwater in bays, is subject to stress due to unanticipated unsupported weight and can either potentially fail of its own accord or be a snag for a passing vehicle or ship, which can pull on it until it breaks.[5] Such a snagging has already resulted in an explosion and loss of life.[5] Nondestructive test methods are needed for evaluation of stress developed in pipeline. This pipeline stress is biaxial (i.e., stress is in both circumferential and longitudinal directions).

The approach in this project is to evaluate several magnetic NDE techniques as to their utility in monitoring or measuring the two conditions - neutron embrittlement and biaxial stress. This involves experimentally applying the magnetic NDE techniques to the conditions of interest and evaluating the sensitivity of the techniques. It also involves physical interpretation of the experimental data based on application of the magnetomechanical hysteresis model[6,7] to the NDE techniques and conditions of interest. Development and use of the model will assist in better design of the techniques and in understanding how to use the detection methods to best advantage. It will

also help explain why one technique might be more sensitive than another.

The magnetic NDE techniques[8-10] that are being applied in this project are:

(1) magnetic hysteresis loop analysis;[10-12]

(2) nonlinear harmonics,[6, 8, 13-16] i.e. analysis of the fundamental and higher order harmonics of the hysteresis loop;

(3) Barkhausen noise analysis;[8,10,17-21]

(4) magnetically induced velocity change of ultrasonic waves (MIVC);[8,22-27]

(5) magabsorption;[9,28]

These techniques have all been used for material characterizations and for residual stress measurements, though not necessarily for biaxial stress situations. Of these techniques, primarily Barkhausen noise analysis has been used for studies of neutron irradiation damage.[29-33]

Since this report is on monitoring neutron embrittlement nondestructively, we focus in detail on the use of the magnetic techniques for that purpose. In the work of Buttle et al,[29-31] Barkhausen studies were done on iron but not pressure vessel steel embrittled at reactor pressure vessel wall temperatures, viz. 550°F (290°C).[1,2,34] In the work of Kwon and Ono,[32] a much smaller sample set was involved than used in our study. Preliminary studies of magabsorption monitoring of embrittled pressure vessel steels were completed many years ago at SwRI[33], which indicated a correlation between neutron embrittlement and magabsorption. However, all the irradiated samples used were subject to the same single period of neutron irradiation. Finally, changes in hysteresis loop properties[35] like coercivity[36], initial magnetization curve[36], permeability[37], and saturation remanence[38], have been studied for cases of neutron-damaged ferromagnetic specimens, not necessarily for pressure vessel steel or a large sample set. An unreported study on Barkhausen studies of pressure vessel steel is presently ongoing in Britain, but is not yet reported.[39] In addition, application of the magnetoacoustic emission technique to neutron embrittlement has been investigated,[29-32] but again in studies limited in scope.

What has been needed is a much more systematic study on utilization of magnetic NDE methods for measuring embrittlement in pressure vessel steels. Our study, as reported here, is much more comprehensive and systematic than any reported up to now.

The present report details work accomplished in the first year of a three-year research project. During the first year the focus was entirely on the neutron embrittlement problem, which is therefore the almost exclusive subject of this report. In the second year, the focus will shift to the biaxial stress problem, and we shall outline project work and anticipated work in a separate interim report for that part of the project.

II. BACKGROUND ON NUCLEAR POWER PLANT SURVEILLANCE TESTING

At reactor startup time, unbroken Charpy specimens are positioned in capsules inside the pressure vessel in the space between the pressure vessel wall and the thermal shield which surrounds the core region. (See Fig. 1). The capsules are attached radially to the outer surface of the thermal shield rather than to the vessel surface, where fast neutron fluence is one-third less than at the shield. The capsules are immersed in water coolant at high pressure (>2000 psi) and high temperature (550°F, or equivalently, 290°C). The vertical position of the capsules is in the "beltline" region of the cylindrical reactor on the same line as the middle of the core region.

A single capsule is removed during reactor shutdown service periods (spaced about 3 years apart). Specimens in each capsule are labeled by the number of effective full power years (EFPY) that the capsule was in service. A considerable number of dosimeters of different types are positioned inside the capsule along the entire length of capsule. These dosimeters plus the relative geometry of the fuel rods and capsule position allow the computation of average accumulated neutron irradiation per cm^2 or neutron fluence (in neutrons/cm^2) for each type of test specimen.

Test specimens are typed by whether the specimen roll axis is parallel (Transverse (T) specimen) or perpendicular (Longitudinal (L) specimen) to the Charpy notch. In some cases, the specimens are also typed by relative position inside the capsule (i.e. at top, middle, or bottom of capsule, in which case they are labeled with different average fluences). Also, specimens are classified according to whether they are (1) plate specimens (made of the same steel as the pressure vessel plates), (2) weld specimens having weld material identical to that between plates in the pressure vessel or (3) HAZ specimens made of heat-affected material identical to the "heat affected zone" surrounding a weld. In this project, we have used only plate specimens.

Fluences are given only for fast neutrons with energies greater than 1MeV. Thus, neutron damage is correlated with fast neutron fluence, and not overall fluence including thermal neutrons.

Charpy test specimens are machined carefully according to ASTM specifications.[3] The unbroken specimens are 100 mm long with a square cross-section 10 mm on a side. The notch at mid-length is V-shaped at 45° and rounded to a 0.25 mm radius. Figure 2 shows the geometry. When the Charpy specimens are removed from the reactor, they are broken in half at the notch during the Charpy test.

The Charpy test is a standard ASTM test[3] for monitoring degradation of the fracture toughness of the irradiated reactor steel. In this test, the sample is put on an anvil and a specified weight mg is swung from a specified pendulum height h_o into the specimen in such a way that it hits the specimen when it is exactly vertical. The sample fractures, starting at the V notch. The energy given to the sample during fracture is defined as its fracture toughness. This energy is measured by the height h_f to which the pendulum rises after it hits the sample, with the energy being given by $mg\,(h_o - h_f)$. If a steel sample has been irradiated with neutrons, its fracture toughness will have decreased depending on the amount of cumulative neutron fluence to which it has been exposed.

There are two types of fracture - ductile fracture and brittle fracture.[1,40] In the case of ductile fracture, the fracture usually involves necking and then tearing whereas in brittle fracture, the fracture is a crystallographic type of cleavage. At lower temperature, the fracture tends to be brittle fracture and at higher temperatures, the fracture is ductile fracture. The energy required for 100% ductile

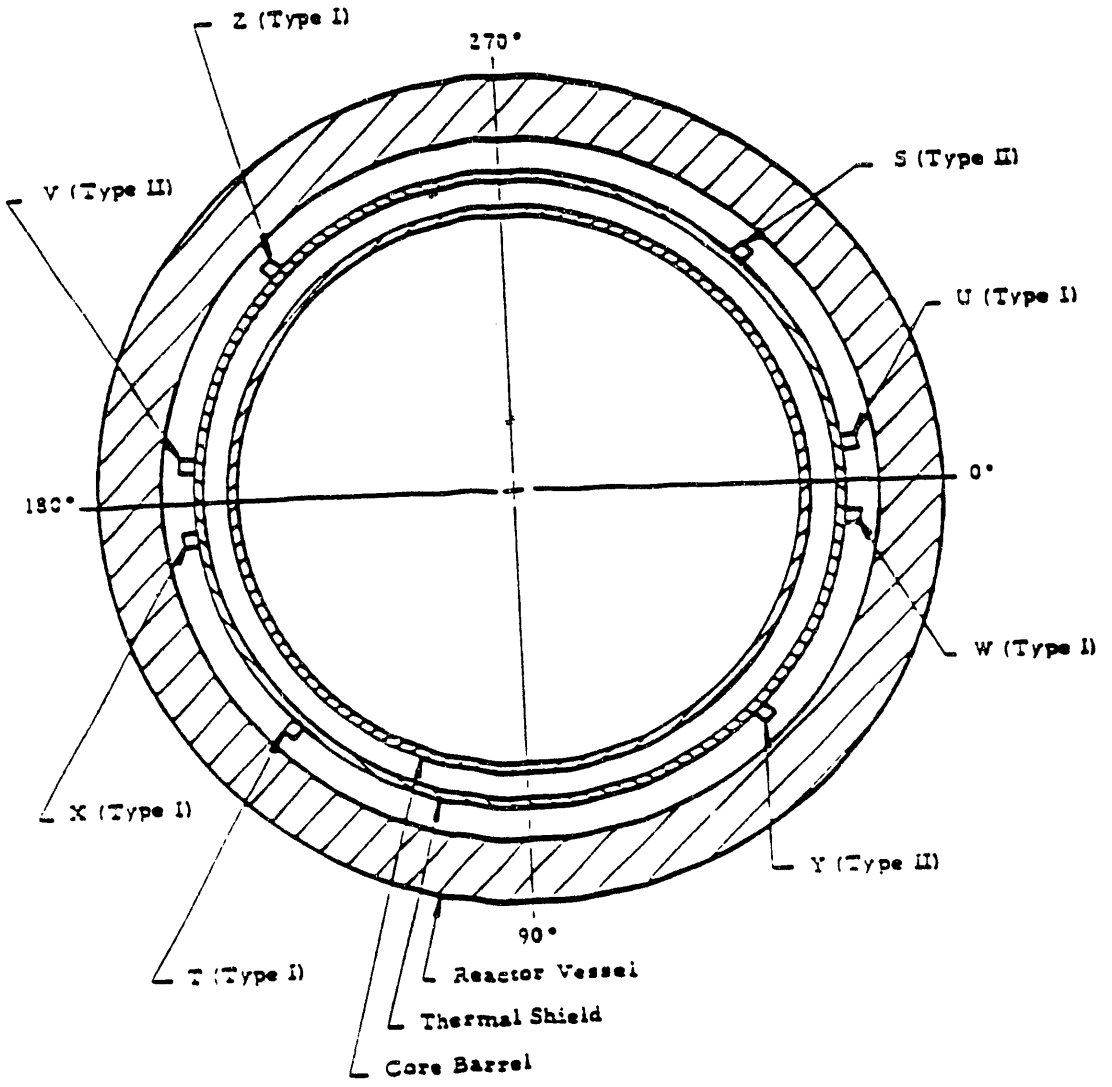

Fig. 1. Arrangement of surveillance capsules in a pressure vessel (after Ref. 2).

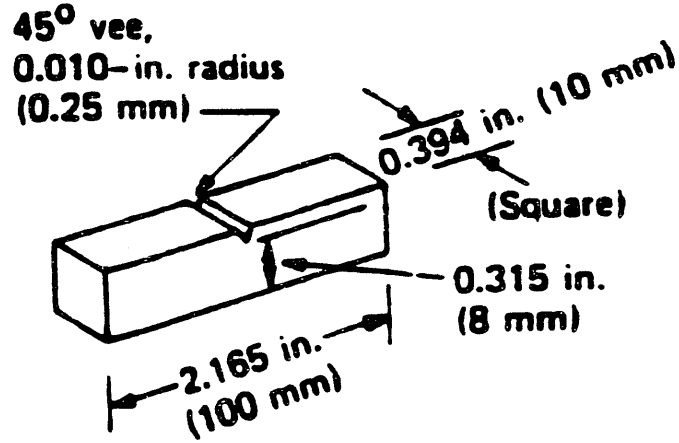

Fig. 2. Diagram of a Charpy specimen machined to specifications [after Ref. 3]

fracture is called the upper shelf energy (USE), whereas the energy for 100% brittle fracture is the lower shelf energy (LSE). Neutron irradiation has the effect of decreasing the USE.[1,40] When both fracture toughness and USE are decreased, the danger of brittle fracture of the vessel during an emergency cooling of the reactor becomes greater.

Fig. 3 shows typical sets of Charpy data for specimens taken from a single capsule.[1] The data is for A-302B plate steel, typical of many reactor pressure vessels. The Charpy impact energy or fracture toughness (either in ft. - lb. or kg-m) is obtained for each Charpy sample from a specimen set, but where the temperature on impact for each sample is changed from sample to sample. The result is a curve which looks like a sloping step. The upper plateau of the curve at high temperatures corresponds to the upper shelf energy (needed for 100% ductile fracture). Note that the transition zone of mixed brittle-ductile fractures is fairly wide in terms of temperature or Charpy impact energy. Note too that it takes less energy to break a brittle specimen.

Fig. 3 also shows how a Charpy curve changes after Charpy samples from the same batch of steel have been irradiated, in this case to 3×10^{19} n/cm^2 of fluence.[1] The tendency is for the transition region to shift to higher temperatures (making the samples more brittle at a given temperature); also the upper shelf energy tends to decrease (requiring less energy for ductile fracture). One parameter that can be used as a measure of neutron embrittlement is the temperature shift of the Charpy curve at a given energy (taken by ASTM standards to be 60 ft-lb, or roughly the energy for 50% brittle - 50% ductile fracture). The temperature shift at 60 ft.-lbs is usually designated as ΔT_{NDT} or RT_{NDT}. (NDT stands for "nil ductility transition", referring to the transition at which ductile fracture no longer dominates the fracture type; T_{NDT} is the nil ductility transition temperature; and R stands for "reference" and refers to temperature shift at the reference energy of 60 ft-lb.) Another parameter that can be used as a measure of embrittlement is the change in the upper shelf energy (Δ(USE)), which measures ease of ductile fracture at the higher temperatures. As the upper shelf energy shifts to lower energies after more and more irradiation, it is seen that the change Δ(USE) gets larger.

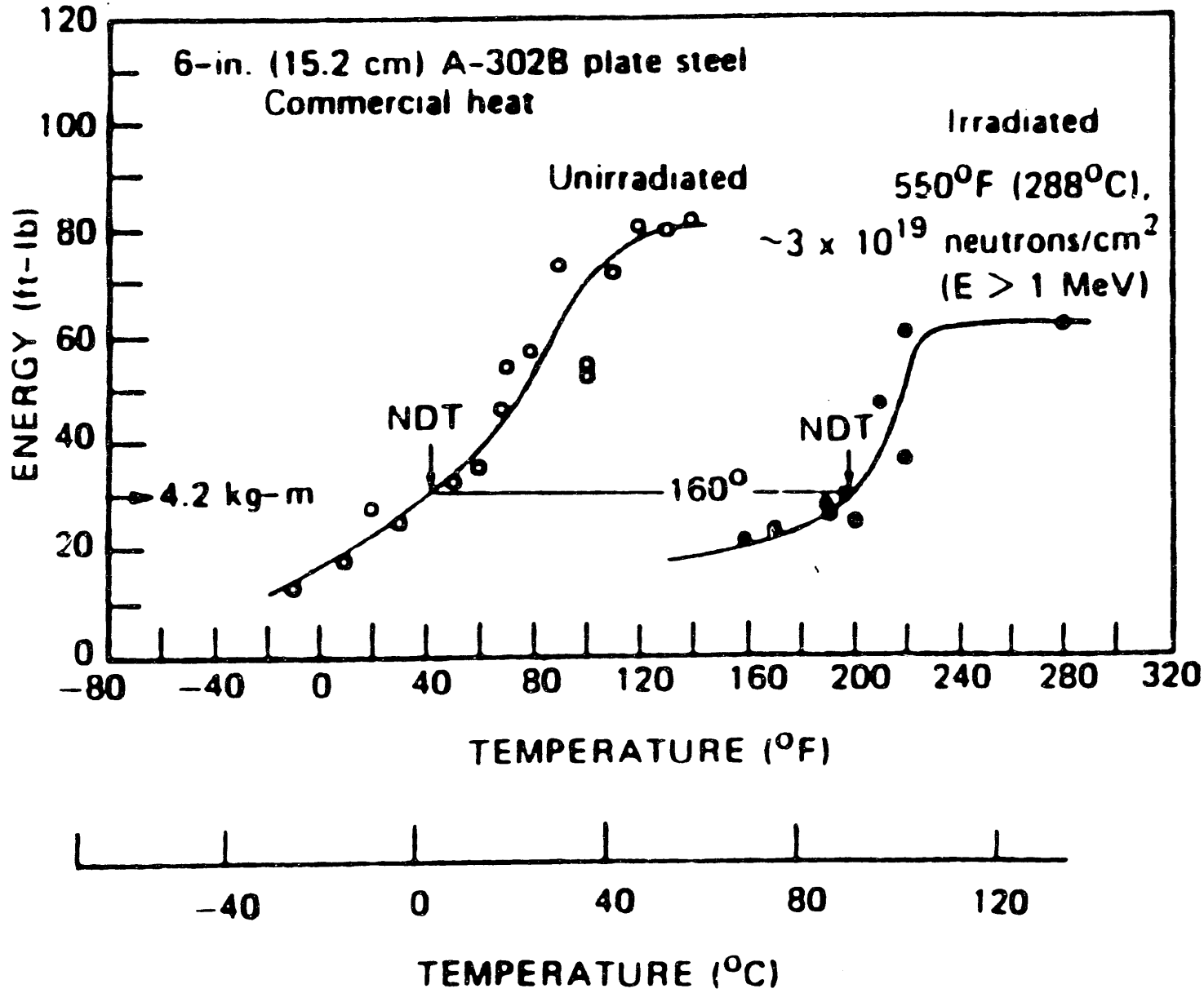

Fig. 3. Typical Charpy V impact data for irradiated A-302B plate steel. (after Ref. 1).

III MAGNETIC MEASUREMENTS ON NEUTRON-EMBRITTLED SPECIMENS AT SwRI

A. Specimens

In a hot-cell facility at Southwest Research Institute, many destructively-tested Charpy test specimens are kept and maintained. These specimens were obtained from neutron-irradiated capsules that had previously been inserted in various nuclear reactors around the country. These Charpy specimens have already been destructively tested, broken in two as part of the standard Charpy test procedure[3] previously performed at the Institute. From this bank of specimens, a set were selected that had been exposed to different fast neutron fluences (spanning an order of magnitude) from two reactors with pressure vessels of different metallurgy.

Table 1 shows Charpy data and average mechanical properties for SwRI Charpy specimens taken from the Indian Point Unit 2 reactor. Table 2 shows the same type of data for the D.C. Cook Unit 2 reactor. The Charpy data in the tables are also plotted in Figs. 4 and 5. Points 1, 2, and 3 are for data corresponding to plate specimens 2002-1, 2002-2, and 2002-3 from Indian Point Unit 2; points A and B correspond to longitudinal and transverse specimens from D.C. Cook Unit 2.

Fig. 4 is a plot of ΔT_{NDT} vs. neutron fluence, using data from the two reactors. Except for data from capsule V at Indian Point Unit 2 (denoted by point 2 at a fluence of 4.57×10^{18} n/cm^2), a monotonic increase with fluence is exhibited by the data. The deviant point is clearly exceptional since its fluence is small and its effective full power years (EFPY) are large, suggesting that perhaps due to its geometric position in the reactor, some of the faster neutrons may have been screened out, thereby decreasing the neutron damage. In fact, the deviant point was from a capsule which was designed to get a more screened exposure, corresponding to that seen by the pressure vessel itself, and thus should not be compared with the other points. It is also noted that whereas data points 3 from Indian Point shows a roughly linear increase with fluence, the D.C. Cook data tends to level off quite dramatically for points with the largest fluence. It was later determined that between the second and third maintenance periods for both D.C. Cook units, a low leakage core configuration was installed, screening off the much faster neutrons from the capsule, thereby decreasing embrittlement changes for the same amount of total fluence for neutron energies greater than 1 MeV. Clearly, embrittlement does not always correlate with the amount of fluence, and hence an NDE technique is needed if one desires not to do the destructive measurement needed to get ΔT_{NDT} and Δ(USE).

Fig. 5 is a plot of change in upper shelf energy vs. neutron fluence, again using data from the two reactors. In general, upper shelf energy does not correlate as well with fluence as transition temperature shift ΔT_{NDT}, but nevertheless similar trends are seen in this data as were seen in Fig. 4.

The experimental accuracy for the data in Table 1 for the Indian Point 2 reactor is estimated to be $\pm$ 5° in ΔT_{NDT} and $\pm$ 4 ft.-lbs in Δ(USE). The experimental accuracy for the D.C. Cook data is $\pm$ 5° in ΔT_{NDT} and $\pm$ 5 ft.-lbs in Δ(USE). Fluences are known to within $\pm$ 5%. Dosimetry analysis for determining fluence is performed according to a standard dosimetry analysis computer calculation.[41] The above error estimates refer to error in the mean of a group of samples, and not the error in the value for a specific sample. Each specific sample is assigned the mean value but its real value may in fact fluctuate well outside the range of error assigned to the value of the mean. Table 3 and Table 4 show the specimen chemical compositions and heat treatments for the Indian Point 2 and D.C. Cook 2 reactors respectively. Differences in chemical composition occur chiefly

TABLE 1. Indian Point 2 Reactor Data on Charpy Specimens

Capsule	*EFPY*	*Plate*	*Fluence*	*Δ(USE) Ft-Lbs*	*ΔT_{NDT} °C*	*.2% YS*	*Tensile Test Temp.*	*Young's Modulus*
T	1.42	2002-1	$2.93X10^{18}$	15	60	71.1	550	32.0
		2002-2	$2.93X10^{18}$	11	95	58.6	550	33.5
		2002-3	$2.55X10^{18}$	22	120	63.1	550	29.3
Y	2.34	2002-3	$4.72X10^{18}$	32.5	145	76.4	550	28.7
		2002-3	$4.72X10^{18}$	—	—	—	550	35.0
Z	5.17	2002-1	$1.2X10^{19}$	25	130	81.6	300	22.9
		2002-2	$1.2X10^{19}$	27	120	69.9	300	24.96
		2002-3	$9.6X10^{18}$	32	185	74.3	300	22.6
V	8.6	2002-2	$4.57X10^{18}$	6	80	65.3	75	25.5
		2002-2	$4.57X10^{18}$	—	—		550	18.5

TABLE 2. D.C. Cook Reactor Data on Charpy Specimens

Capsule	*EFPY*	*Plate*	*Fluence*	*Δ(USE) Ft-Lbs*	*ΔT_{NDT} °C*	*.2% YS*	*Tensile Test Temp.*	*Young's Modulus*
T	1.08	C5521-2L	$2.3X10^{18}$	16	55			
		C5521-2T	$2.3X10^{18}$	12	80	58.7	250	33.3
		C5521-2T	$2.3X10^{18}$	—	—		550	25.7
Y	3.24	5521-2L	$7.01X10^{18}$	24	90			
		5521-2T	$7.01X10^{18}$	18	100	72	210	27.5
		5521-2T	$7.01X10^{18}$	—	—		550	27.4
X	5.27	5521-2L	$1.0X10^{19}$	42	95			
		5521-2T	$1.0X10^{19}$	23	103	76	250	22.5
		5521-2T	$1.0X10^{19}$	—	—		550	28.3

Note: (2L → A, 2T → B)

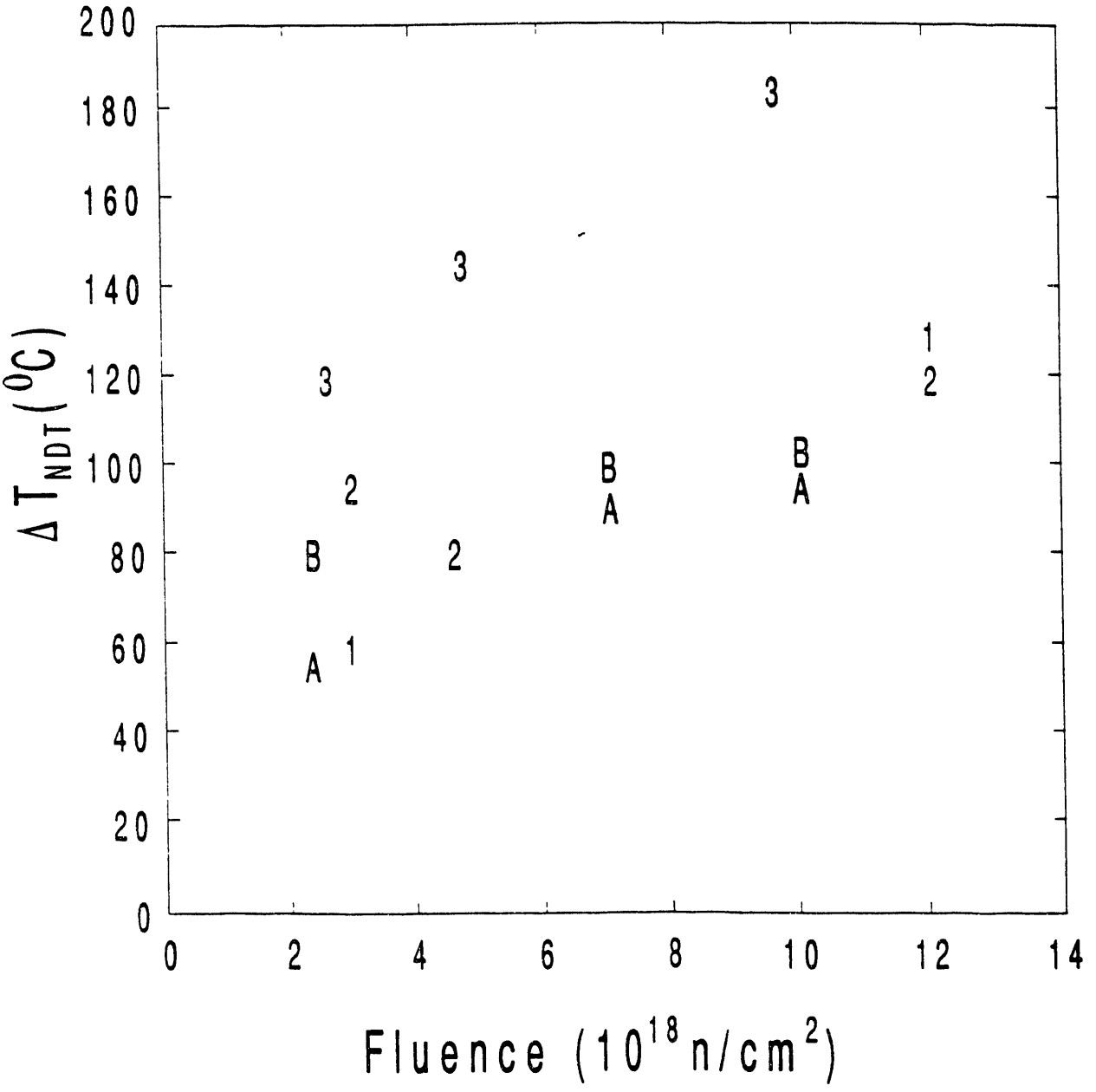

Fig. 4. Transition temperature shift ΔT_{NDT} vs. neutron fluence for specimens in Tables 1 and 2. A and B refer to longitudinal and transverse specimens for the D.C. Cook 2 reactor. 1, 2, and 3 refers to specimens from the Indian Point 2 reactor.

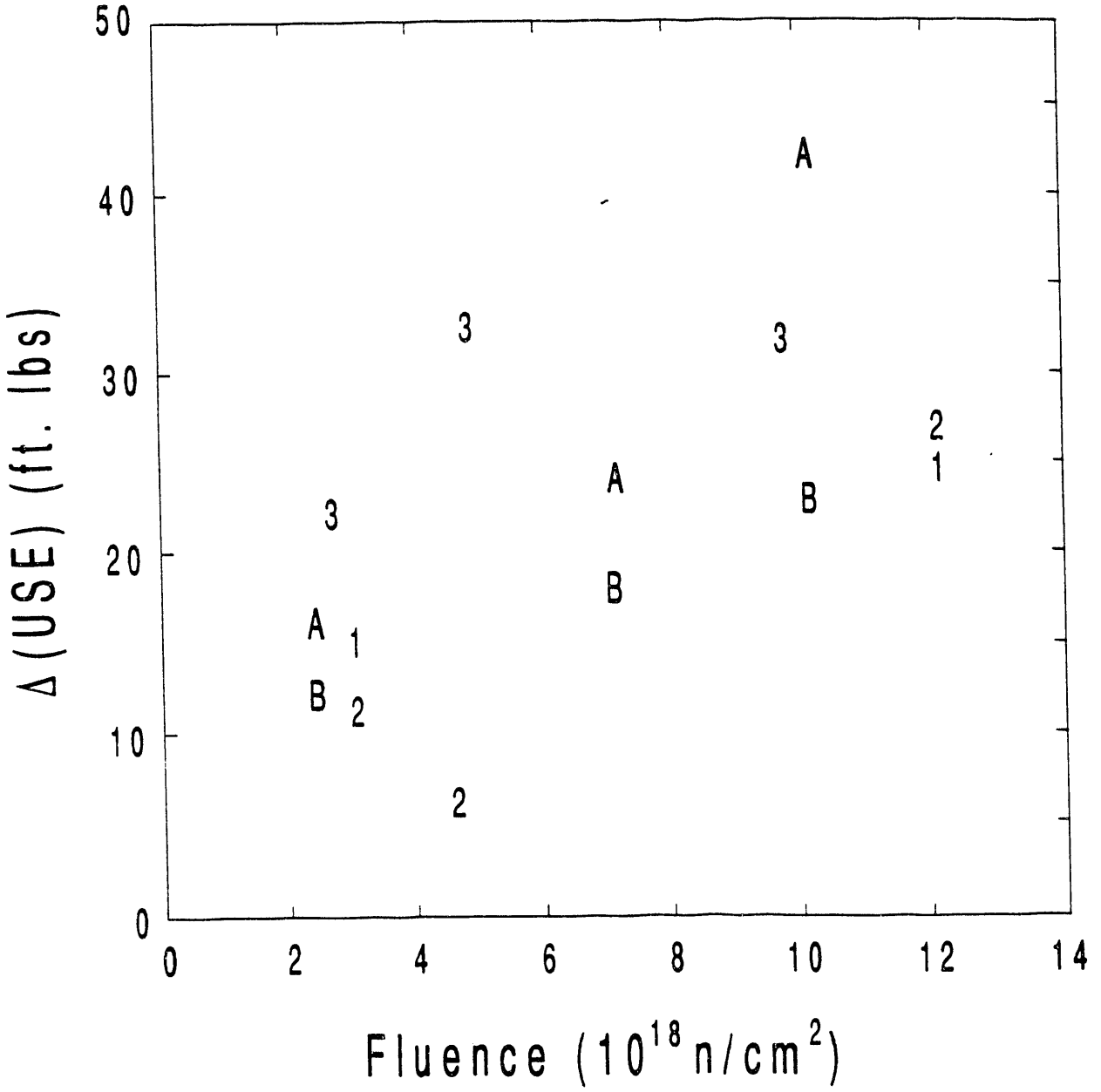

Fig. 5. Change in upper shelf energy Δ(USE) vs. neutron fluence for specimens described in Tables 1 and 2. A, B, 1, 2, and 3 are defined as in Fig. 5.

TABLE 3. Indian Point Unit No. 2 Pressure Vessel Plate Metallurgical Data

Combustion Engineering, Inc., furnished sections from three hot-formed 9-5/8" thick plates (B2002-1, B2002-2, and B2002-3) of SA 302 Grade B modified steel and a weldment joining two formed plates (B2002-1 and B2002-3) used in the fabrication of the Indian Point Unit No. 2 reactor pressure vessel intermediate shell course. These plates were produced by the Lukens Steel Company.

a. Chemical Analyses (Percent)

Plate No.	Lukens Heat No.	C	Mn	P	S	Si	Ni	Mo
B2002-1	B4688-2	0.20	1.28	0.010	0.019	0.25	0.58	0.46
B2002-2	B4701-2	0.22	1.30	0.014	0.020	0.22	0.46	0.50
B2002-3	B4922-1	0.22	1.29	0.011	0.018	0.25	0.57	0.46

b. Heat Treatment

The sections of formed shell plate material were heat treated by Combustion Engineering as follows:

1550° – 1650°F, 4 hours, Water Quenched

1225° ± 25°F, 4 hours, Air Cooled

1150° ± 25°F, 40 hours, Furnace Cooled to 600°F

The weldment was stress-relieved by Westinghouse as follows:

1150° ± 25°F, 19-3/4 hours, Furnace Cooled to 600°F

TABLE 4. Donald C. Cook Unit No. 2 Reactor Vessel Surveillance Materials

Heat Treatment History

Shell Plate Material:

Heated to 1700°F for 4-1/2 hours, water quenched.

Heated to 1600°F for 5 hours, water quenched.

Tempered at 1250°F for 4-1/2 hours, air cooled.

Stress relieved at 1150°F for 51-1/2 hours, furnace cooled.

Weldment:

Stress relieved at 1140°F for 9 hours, furnace cooled.

Chemical Composition (Percent)

Material	C	Mn	P	S	Si	Ni	Mo	Cu	Cr
Plate C-5521-2[a]	0.21	1.29	0.013	0.015	0.16	0.58	0.50	0.14	—
Plate C-5521-2[b]	0.22	1.28	0.017	0.014	0.27	0.58	0.55	0.11	0.072
Weld Metal[b]	0.11	1.33	0.022	0.012	0.44	0.97	0.545	0.055	0.068
Weld Metal[c]	0.08	1.42	0.019	0.016	0.36	0.96	—	0.05	0.07

(a) Lukens Steel analysis.
(b) Westinghouse analysis.
(c) Chicago Bridge and Iron analysis.

in sulfur, silicon, copper and chromium content. The Indian Point 2 plate steel is classified as a modified SA 302 Grade B steel, whereas D.C. Cook 2 steel is also classified as SA533 Grade B steel. The heat treatments also differ slightly, with the D.C. Cook 2 steel receiving an extra period at high temperatures followed by water quenching. The stress-relief period was also longer for the D.C. Cook 2 steel.

It was decided that test specimens corresponding to points 3 from Indian Point 2 be used for the magnetic measurements. It was also decided that specimens corresponding to points A (longitudinal specimens) from D.C. Cook 2 be also used for the magnetic measurements. The samples selected exhibited the closest correlation to linear behavior in Fig. 2 out of the specimen sets available. Again, these are broken Charpy specimens and are half the length depicted in Fig. 2.

B. Experimental Setups and Procedures

1. Measurement of Magnetic Hysteresis, Nonlinear Harmonics, and Barkhausen Noise

Measurements of (1) magnetic hysteresis parameters, (2) nonlinear harmonics, and (3) Barkhausen noise were made with appropriate instrumentation using a common magnetization arrangement and sensors. A block diagram of the magnetization and sensor arrangement and the instrumentation is shown in Figure 6 and a photograph of the actual setup is shown in Figure 7. A magnetizing coil and magnetic circuit were used to magnetize the specimens. The applied magnetic field was measured with a Hall effect sensor placed on the surface of the specimen; and the magnetic induction in the specimen, the nonlinear harmonics, and the Barkhausen noise (BN) were measured using an encircling sensing coil. The sensing coil was wound on a plastic coil form which slipped over each specimen. A plastic fixture was used to precisely position both the sensing coil and the specimens in the magnetic circuit. This plastic fixture is not seen in Fig. 7 because when in use, it obscures much of what is otherwise visible in the setup.

Hysteresis loops and harmonic amplitudes were measured using a sinusoidal 1Hz magnetizing waveform. A digitized hysteresis loop was stored for the purpose of the extracting magnetic parameters. Barkhausen noise amplitudes were measured with a triangular 0.5 Hz waveform (the triangular waveform provides approximately a linear change of the applied magnetic field in the region where Barkhausen noise is generated.) The signal from the sensing coil is amplified and then directed to (1) a spectrum analyzer for measuring the harmonics, (2) a Barkhausen noise detector which outputs a signal proportional to the envelope of the Barkhausen noise burst and measures the peak amplitude of the envelope, and (3) a hysteresis loop analyzer which generates the hysteresis loops from the sensing coil and Hall-effect sensor signals and determines the magnetic parameters from the loop generated.

Using the instrumentation illustrated in Figure 6, eight magnetic parameters, listed in Table 5, were measured from each sample. Except for Barkhausen noise peak amplitude, all the parameters were measured at four different levels of H_{max} to evaluate whether the magnetization level affects the correlations between the magnetic parameters and the fluence, Δ(USE), and ΔT_{NDT}. The approximate values of the applied H_{max} were, respectively, level 1 - 8 Oe, level 2 - 15 Oe, level 3 - 23 Oe, and level 4 - 41 Oe. All samples showed magnetic saturation at level 4. Note that the term "level" is used here because each level corresponded to a particular magnetizing current, and H_{max}

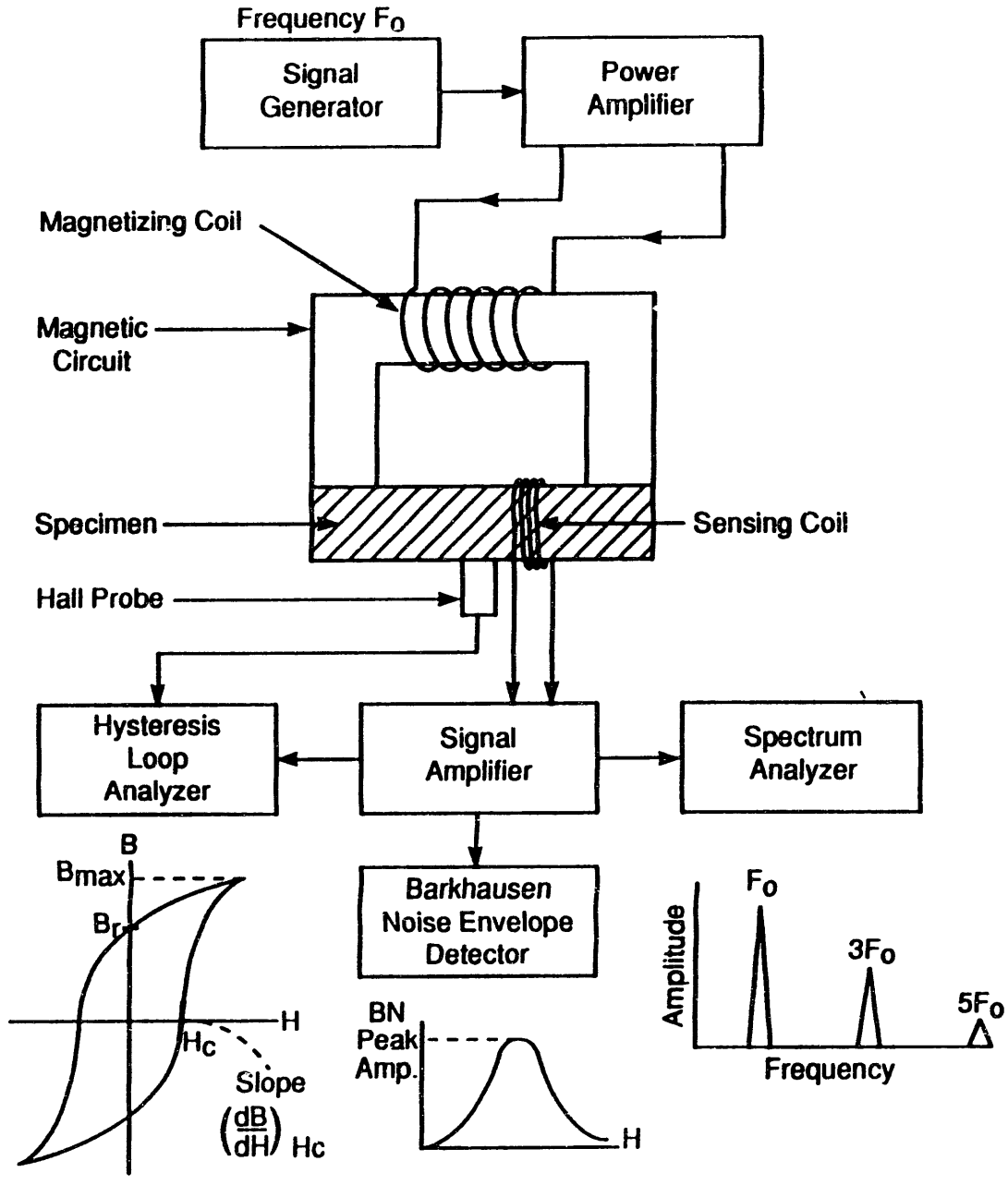

Fig. 6. Sensor and instrumentation arrangement for magnetic hysteresis, nonlinear harmonics, and Barkhausen noise measurements.

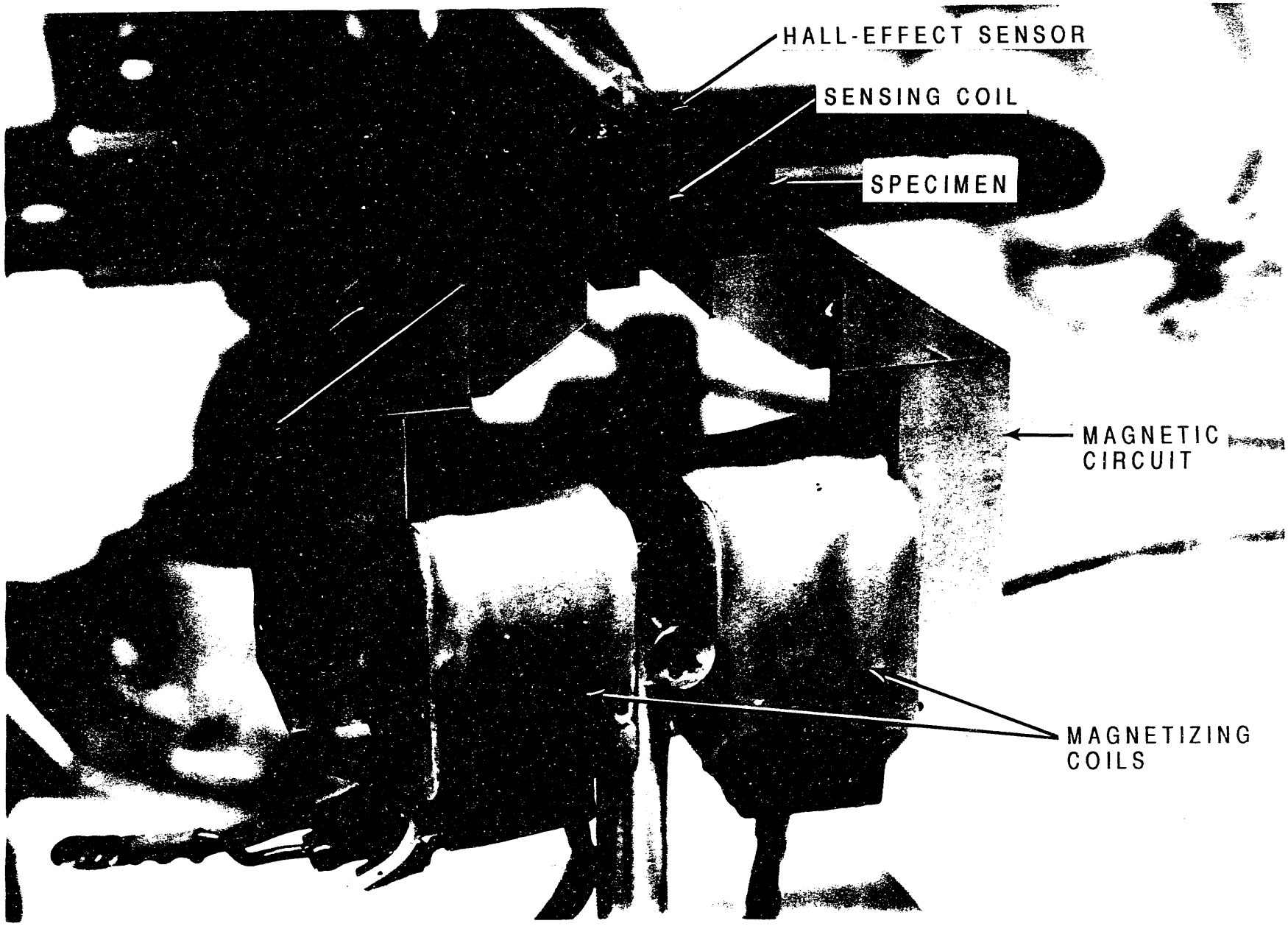

Fig. 7. Photograph of magnetic circuit, sensors, and specimen. A plastic fixture, not shown in the photograph, was used to precisely position the specimen into the magnetic circuit.

TABLE 5. Magnetic Parameters and Their Measurement Error

No.	*Magnetic Parameter*	*Measurement Error (%)*
1	F_0 — Fundamental Frequency Amplitude	+/- 0.9
2	$F_3 = 3F_0$ — Third Harmonic Amplitude	+/- 1.4
3	$F_5 = 5F_0$ — Fifth Harmonic Amplitude	+/- 1.5
4	H_c / H_{max}	+/- 3.1
5	B_r / B_{max}	+/- 1.7
6	B_{max} / H_{max}	+/- 3.6
7	dB / dH at H_c	+/- 11.4
8	Barkhausen Noise Peak Amplitude	+/- 0.8

actually varied slightly from sample to sample.

To determine the repeatability of the measurements, measurements were repeated five times using an unirradiated SA533B specimen obtained from Babcock and Wilcox. In each measurement, the sample was taken out of the plastic fixture and then repositioned. The experimental measurement error (100% x standard deviation/mean) based on these measurements is given in Table 5. The error values in the table represent those determined at H_{max} level 1. At higher H_{max} levels, the errors were proportionally smaller; and were reduced to approximately 1/3 of those given in the table at level 4. Except for the parameter dB/dH at H_c, the measurement error was within a few percent.

2. Measurement of Magnetically Induced Velocity Change (MIVC) of Ultrasonic Waves

Figure 8 shows a block diagram of instrumentation for measuring the magnetically induced velocity changes (MIVC) of ultrasonic waves. An electromagnet is used to apply a biasing magnetic field to a specimen, and the applied magnetic field is measured with a Hall effect probe. An ultrasonic transducer is used to transmit ultrasonic waves (either longitudinal or shear) and to detect signals reflected from the back surface of the specimen. The velocity change induced by the magnetization is then detected by measuring the shift in the arrival time of the received ultrasonic signal.

A photograph of the actual experimental setup is shown in Figure 9. For biasing magnet, the same magnetic circuit used for measuring magnetic hysteresis and nonlinear harmonics was also used. The ultrasonic transducer (5-MHz and 0.25-inch-diameters) was placed on the irradiated sample and kept in place by using a C-bracket and screw-loading arrangement. The bracket was made of aluminum and bolted to the magnetic core of the magnetic circuit. Both longitudinal- and shear-wave transducers (Panametrics type V110 and V156, respectively) were employed in the measurements. Honey was used as a couplant between the transducer and the irradiated sample to facilitate the transmission of ultrasonic energy through the transducer and specimen interface. The Hall probe was placed next to the transducer. The specimen face used for measurement was always the side on which the Charpy notch had been machined. This is consistent with the other magnetic measurements described earlier.

For measuring changes in the arrival time of the received ultrasonic waves, an MBS-8000 ultrasonics test systems (MATEC Instruments, Inc.) was employed. The MBS-8000 system is a specialized ultrasonic instrument capable of measuring small changes in transit time (or wave velocity) with an accuracy of a few parts per million. The changes in transit time were measured as a function of applied magnetic field while cycling the magnetic field at a rate of approximately 0.1 Hz. The instrumentation control, digitization of the transit-time and magnetic-field data, conversion of the acquired data to changes in velocity (relative to the velocity at zero applied magnetic field), and an x-y plot and display of the MIVC data were performed using a personal computer.

3. Measurement of Magabsorption

Magabsorption involves measurement of the change in the impedance of an rf coil coupled to a ferromagnetic material in a bias magnetic field. The bias field is varied cyclically using an electromagnet so that the rf impedance changes as the bias field changes. The magabsorption

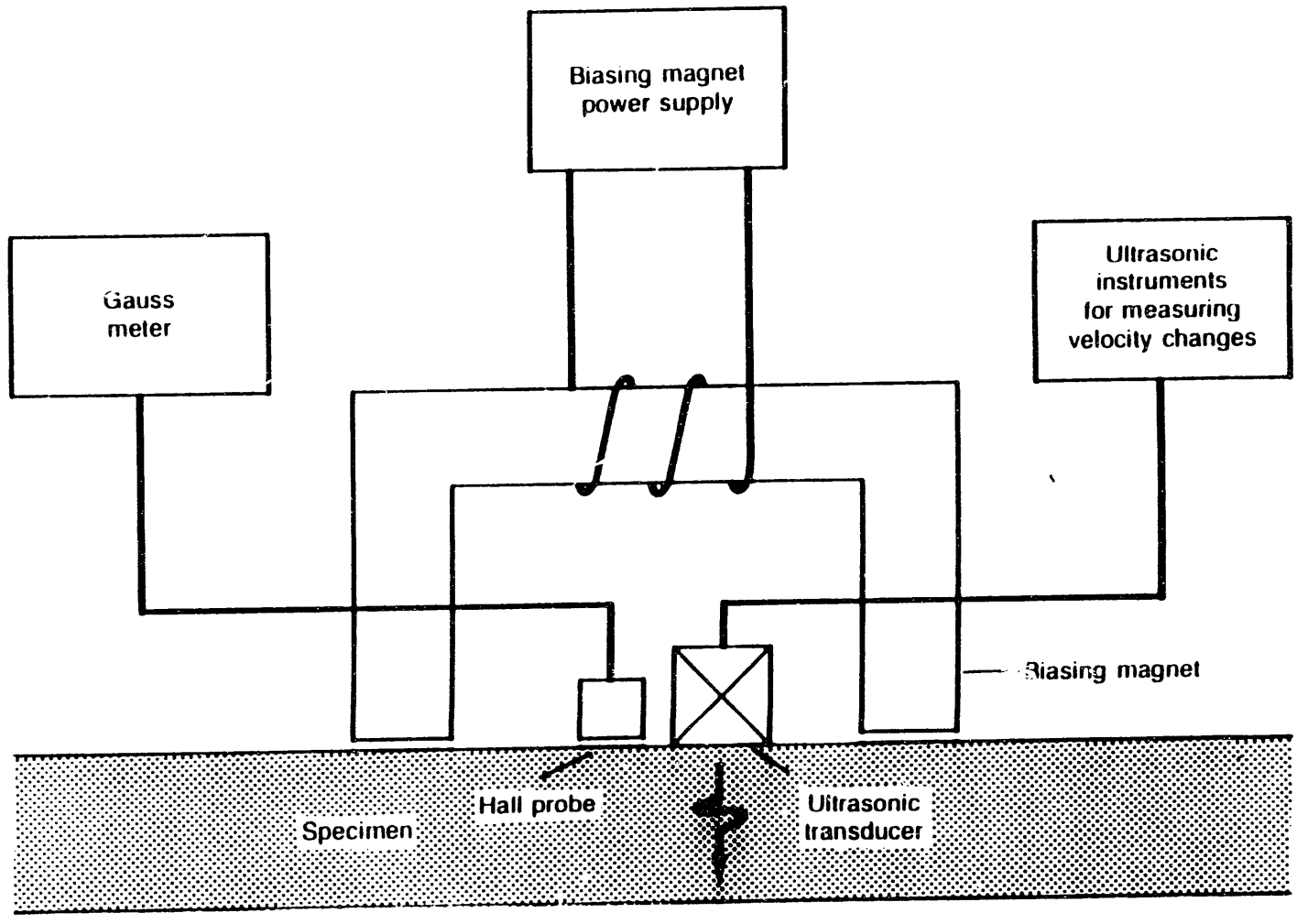

Fig. 8. Block diagram of instrumentation for measuring MIVC for ultrasonic waves

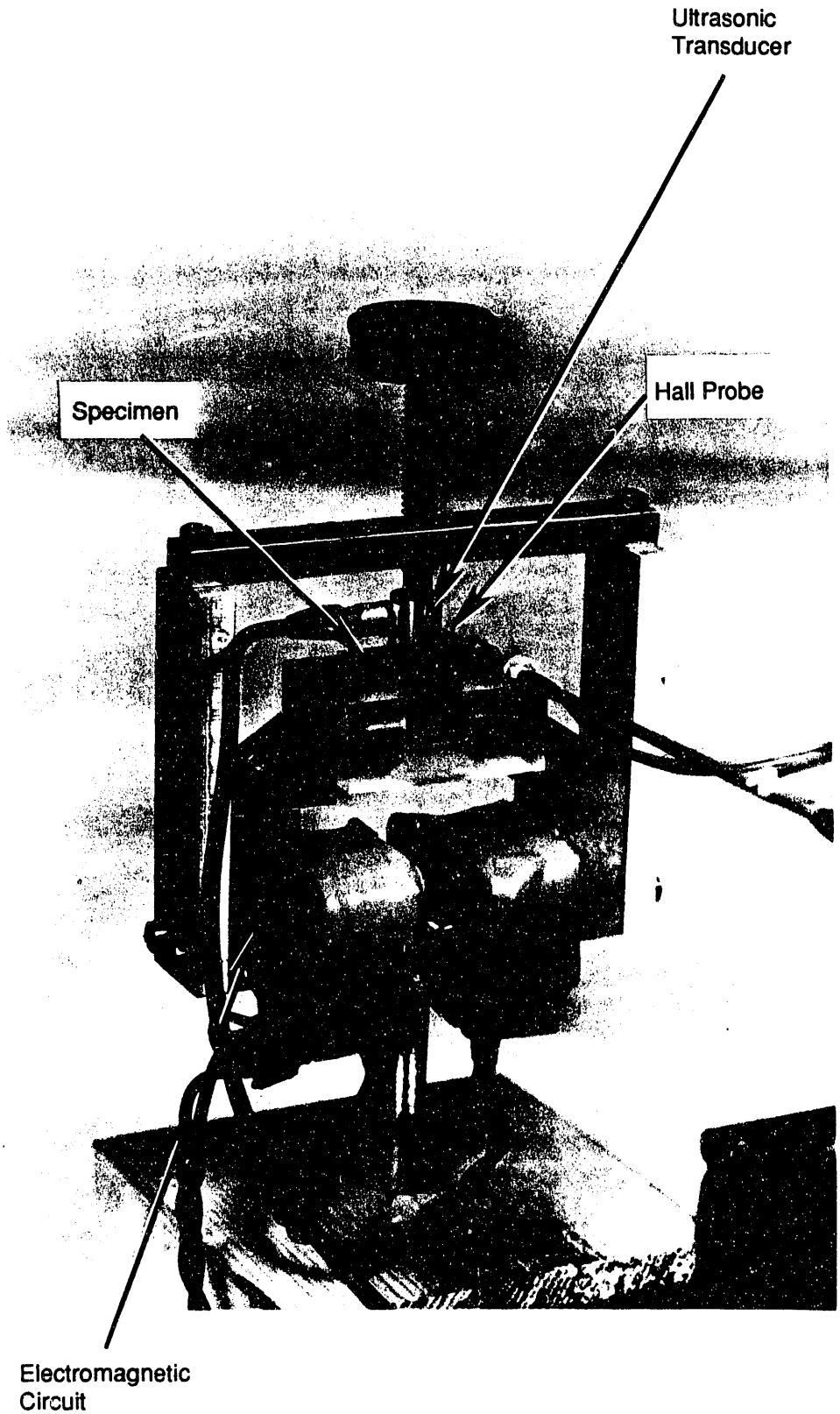

Fig. 9. Photograph of experimental setup for measurement of MIVC

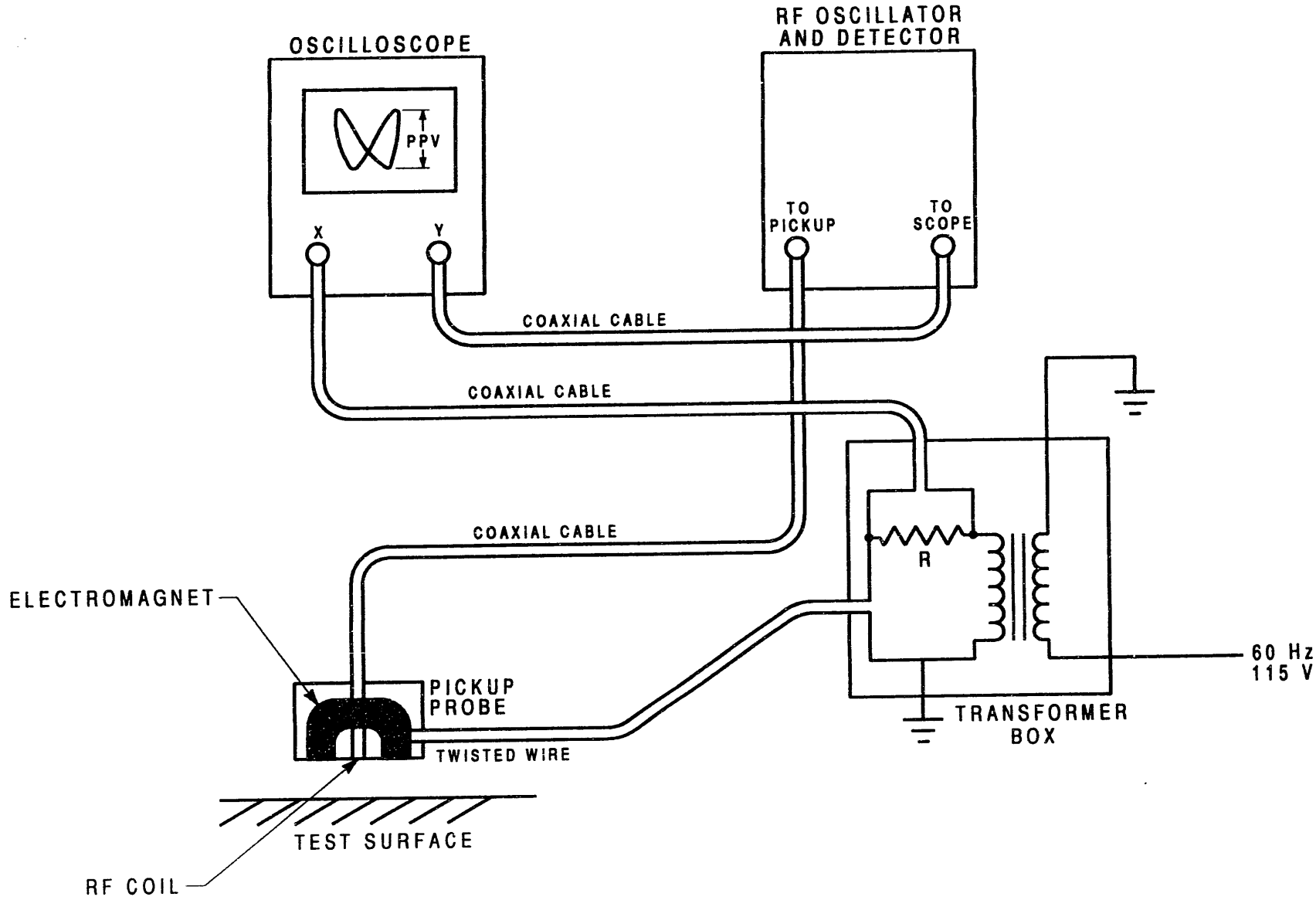

Fig. 10. Magabsorption circuit used on this project.

voltage signal associated with the changing rf impedance traces out a butterfly-shaped hysteresis loop when plotted against the input ac current applied to the electromagnet. The butterfly-like loop arises because the rf impedance depends on the a.c. permeability. For magnetic hysteresis, the permeability dM/dH is always positive for both positive and negative H. Hence, there is reflective symmetry rather than inversion symmetry in the magabsorption hysteresis, and hence a butterfly-shaped loop. Details on these effects may be found in ref. 9 or ref. 28.

The magabsorption circuit that was used for the measurements on this project is depicted in Fig. 10. The pickup probe shown in the figure consists of (1) an electromagnet to produce the 60 Hz bias magnetic field and (2) an rf coil between the electromagnet pole pieces. The rf coil has approximately 250 millihenries inductance and carries a rf signal of 225 kHz modulated by a 60 Hz component which is produced by the bias magnetic field in the presence of nearby ferromagnetic material. The rf signal is demodulated by the rf detector and the resulting 60 Hz magabsorption signal that is extracted is sent to an oscilloscope on which the butterfly-shaped hysteresis loop is displayed. The y-input to the oscilloscope is the magabsorption signal. The x-input is the voltage across a 5-Ω resistor through which the bias-field-producing 60 Hz input current is sent. Typical magabsorption hysteresis loops are seen in Fig. 11.

In this experiment, the probe was positioned on the broken Charpy specimen with its bias magnetic field parallel to or perpendicular to the long axis of the specimen and always on the side containing the Charpy notch. Different peak-to-peak voltages resulted for the butterfly loop signal depending or whether the parallel or perpendicular case were being examined. Digitized peak-to-peak voltage for both parallel and perpendicular cases were read directly from the output display of the oscilloscope. The different peak-to-peak voltages were tabulated for each specimen, and analysis was performed later to see if there was any correlation between the peak-to-peak voltage and embrittlement.

C. Experimental Results and Discussion

1. Results from Hysteresis Data, Nonlinear Harmonics, and Barkhausen Noise

Specimens for three different levels of neutron fluences were examined from each of the two reactors. A set of five broken Charpy specimens were tested for each level of neutron fluence. In all 30 specimens were tested. This is twelve more specimens than were tested at the time of the interim report DOE/ER/14180-1 (Jan. 1992).

Digitized results obtained from hysteresis loops and corresponding nonlinear harmonic and Barkhausen noise (BN) measurements were evaluated using statistical techniques in order to determine how well the magnetic data values correlated with fluence, Δ(USE), and ΔT_{NDT}. The R^2 value, which is the square of the correlation coefficient (see Appendix 1), was determined for each parameter as a measure of this relationship, and the results are shown in Table 6. The R values of +1 or -1 indicate perfect correlation with positive and negative slopes of the fit respectively, and the correlation decreases as the R values approach zero, with a zero value indicating no correlation. Note that 7 of the magnetic parameters were measured at 4 different magnetization levels; for BN, only one magnetization level was used.

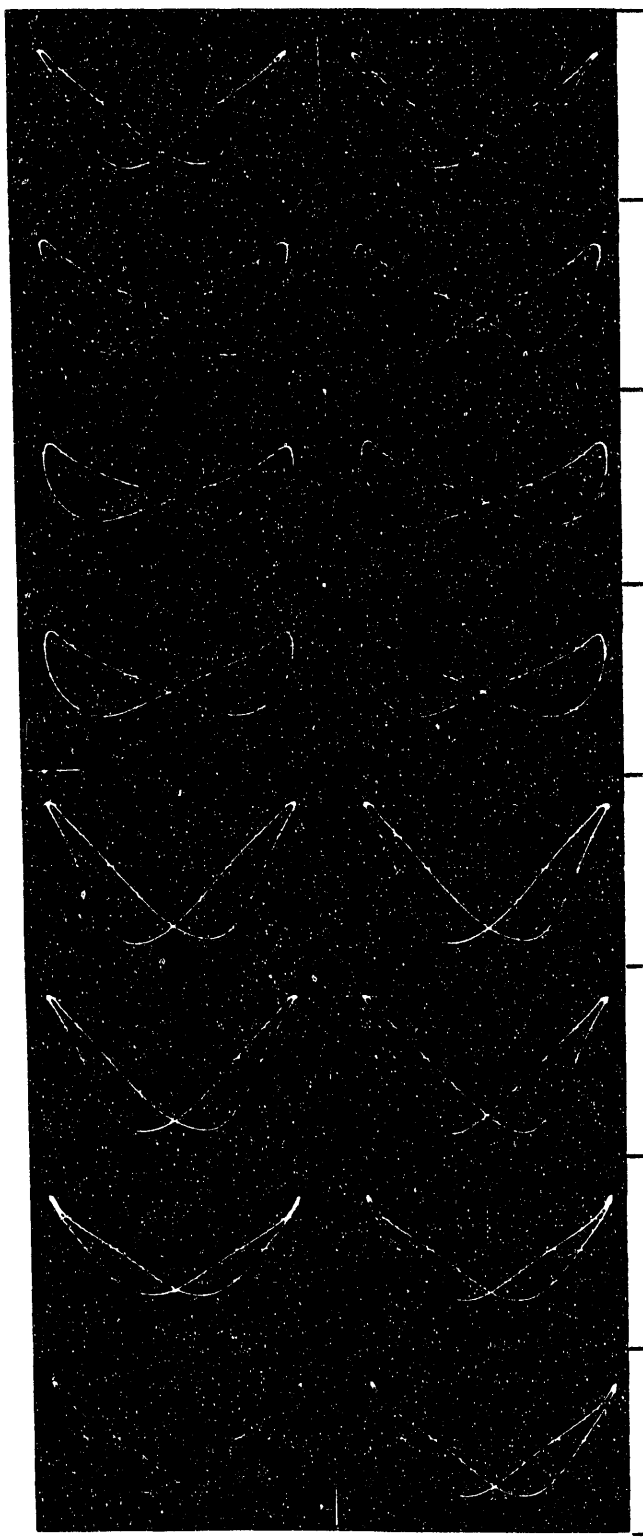

*Low Rad -- irradiation dose 7 x 10^{18} nvt
High Rad -- irradiation dose 15 x 10^{18} nvt

Fig. 11. Examples of magabsorption signals obtained from several different specimens [after ref. 33]

TABLE 6. Square of Correlation Coefficient (R^2) for Measured Magnetic Parameters (Note: $H_{max}1$ ~ 8 Oe, $H_{max}2$ ~ 15 Oe, $H_{max}3$ ~ 24 Oe, $H_{max}4$ ~ 41 Oe)

		Indian Point			*DC Cook Unit 2*		
Property	***Field Level***	***Fluence***	***Δ(USE)***	***ΔT_{NDT}***	***Fluence***	***Δ(USE)***	***ΔT_{NDT}***
Barkhausen Noise	—	0.50	0.38	0.52	0.06	0.04	0.08
Fund. Amp	H_{max} 1	0.57	0.35	0.58	0.00	0.00	0.00
	H_{max} 2	0.66	0.49	0.68	0.00	0.00	0.00
	H_{max} 3	0.59	0.43	0.61	0.00	0.00	0.00
	H_{max} 4	0.25	0.18	0.25	0.01	0.02	0.00
3rd Har. Amp.	H_{max} 1	0.57	0.34	0.57	0.00	0.00	0.00
	H_{max} 2	0.67	0.46	0.68	0.00	0.00	0.00
	H_{max} 3	0.69	0.52	0.72	0.00	0.00	0.00
	H_{max} 4	0.72	0.55	0.74	0.00	0.00	0.00
5th Har. Amp.	H_{max} 1	0.53	0.38	0.54	0.00	0.00	0.00
	H_{max} 2	0.60	0.33	0.60	0.00	0.00	0.00
	H_{max} 3	0.66	0.47	0.68	0.00	0.00	0.00
	H_{max} 4	0.70	0.53	0.72	0.00	0.00	0.00
H_c/H_{max}	H_{max} 1	0.00	0.00	0.00	0.00	0.01	0.00
	H_{max} 2	0.01	0.00	0.01	0.00	0.00	0.00
	H_{max} 3	0.00	0.39	0.00	0.00	0.00	0.00
	H_{max} 4	0.01	0.01	0.01	0.00	0.01	0.00
B_r/B_{max}	H_{max} 1	0.11	0.08	0.11	0.00	0.00	0.00
	H_{max} 2	0.03	0.03	0.04	0.00	0.00	0.00
	H_{max} 3	0.03	0.02	0.03	0.00	0.00	0.00
	H_{max} 4	0.02	0.02	0.02	0.00	0.00	0.00
B_{max}/H_{max}	H_{max} 1	0.35	0.29	0.36	0.00	0.01	0.00
	H_{max} 2	0.06	0.00	0.05	0.00	0.01	0.00
	H_{max} 3	0.19	0.02	0.17	0.01	0.04	0.00
	H_{max} 4	0.20	0.01	0.17	0.01	0.03	0.00
$\frac{dB}{dH}$ at H_c	H_{max} 1	0.18	0.24	0.20	0.03	0.06	0.01
	H_{max} 2	0.01	0.29	0.02	0.05	0.07	0.03
	H_{max} 3	0.13	0.04	0.13	0.06	0.09	0.04
	H_{max} 4	0.06	0.04	0.06	0.01	0.01	0.00

a) Indian Point Specimens

The data taken from Indian Point specimens showed moderate correlation (R^2 ~ 0.65) with fluence and ΔT_{NDT} for the non-linear harmonic amplitudes, and less than moderate correlation ($R^2 \leq 0.55$) with Δ(USE) for all magnetic parameters. The best results were obtained from the 3rd and 5th harmonic amplitudes, all of which had R^2 values ranging from a minimum of 0.54 to a maximum of 0.74 for ΔT_{NDT} and from 0.53 to 0.72 for fluence. For Δ(USE), the R^2 value ranged from 0.33 to 0.55. A slight trend in the correlation was observed for the different applied magnetic field levels (H_{max}) for these parameters, in that the highest level produced the best results in 3rd and 5th harmonic amplitudes. However, the fundamental showed poorest results for the highest level, and R^2 for the fundamental was otherwise similar to the 3rd and 5th harmonics at the lower levels. Magnetic parameters taken from hysteresis loops showed little correlation with embrittlement parameters.

The moderate correlation of R^2 ~ 0.65 represents a change from R^2 ~ 0.9, which characterized previous data obtained with three specimens per fluence level (as reported in our Interim Report of Jan. 1992). Increasing to five specimens clearly moderates the statistics. The decrease in R^2 value suggests that the high correlation obtained previously with three specimens per set was not an accurate reflection of the real situation. It is possible that the true correlation may be lower than that reported in Table 6. To clarify this, additional testing on an even larger sample set should be done.

To illustrate what the R^2 value represents in terms of scatter and trends in the data, the 3rd harmonic signal amplitude (H_{max} level 2) vs. fluence and ΔT_{NDT} are plotted in Figures 12 and 13 for the Indian point specimens. For this data, the corresponding R^2 values are 0.67 and 0.68 respectively. The 3rd harmonic increases with increasing fluence and ΔT_{NDT}, and although considerable scatter exists in the 3rd harmonic value, there is identifiable separation between the groups of 3rd harmonic values at each of the 3 values of fluence and ΔT_{NDT}. It is clear however, that with R^2 ~ 0.65, a single measurement is not enough to identify the embrittlement. One would need to use an average over many samples from the same set in order to expose the overall trends seen in the data in Figs. 12 and 13. This behavior is apparently associated with the statistical nature of the samples because each sample is irradiated a slightly different amount owing to its position in the irradiated capsule relative to the rest of the samples.

The plot of the 3rd harmonic vs. upper shelf energy change Δ(USE) for Indian Point samples (See Figure 14) did not show as good of a relationship as did the fluence and ΔT_{NDT}; the 3rd harmonic increased with increasing energy and then decreased somewhat. From Fig. 4 and 5, however, Δ(USE), measured for the specimens by Charpy tests, did not consistently increase with increasing fluence, as did ΔT_{NDT}. The three groups of specimens had Δ(USE) values of 22, 32.5, and 32, corresponding to fluence values of 2.55 x 10^{18}, 4.72 x 10^{18}, and 9.6x10^{18} and ΔT_{NDT} values of 120°K, 145°K, and 185°K respectively. If Δ(USE) had increased with increasing fluence, thus having the effect of reversing the last 2 energy values in the plot in Figure 14, the 3rd harmonic would have increased monotonically with increasing Δ(USE). It appears that the inconsistent behavior of the magnetic techniques with Δ(USE) may be caused by the inconsistent relationship between Δ(USE) and the fluence. Based solely on the Indian Point data, one would conclude that ΔT_{NDT} may be determined more accurately than Δ(USE) from these magnetic measurements.

Figs. 15, 16, and 17 show plots of Barkhausen noise amplitudes vs. fluence,

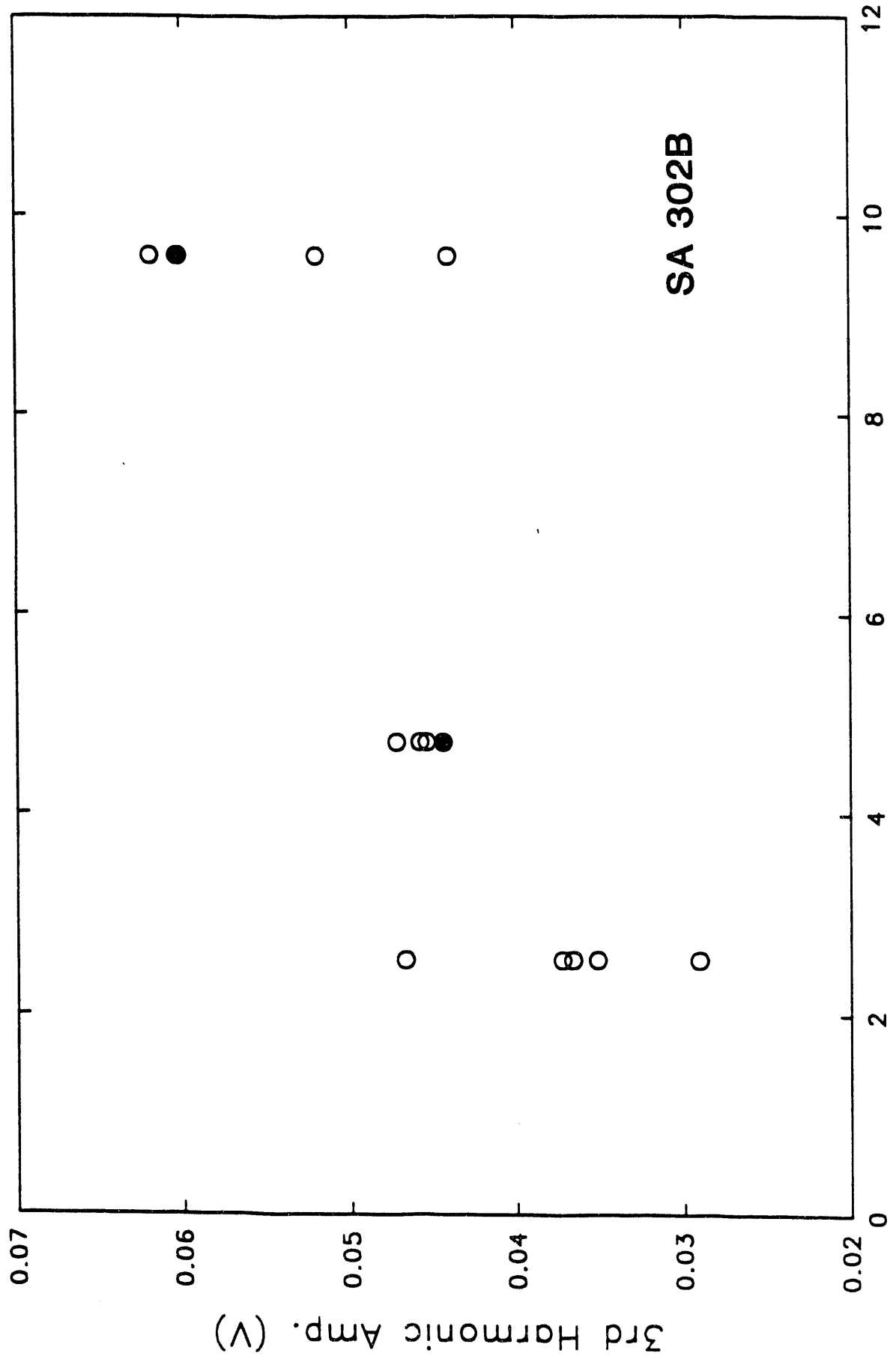

Fig. 12. Third harmonic amplitude vs. fluence for Indian Point specimens at level H_{max} 2. Solid circles show overlapping data points.

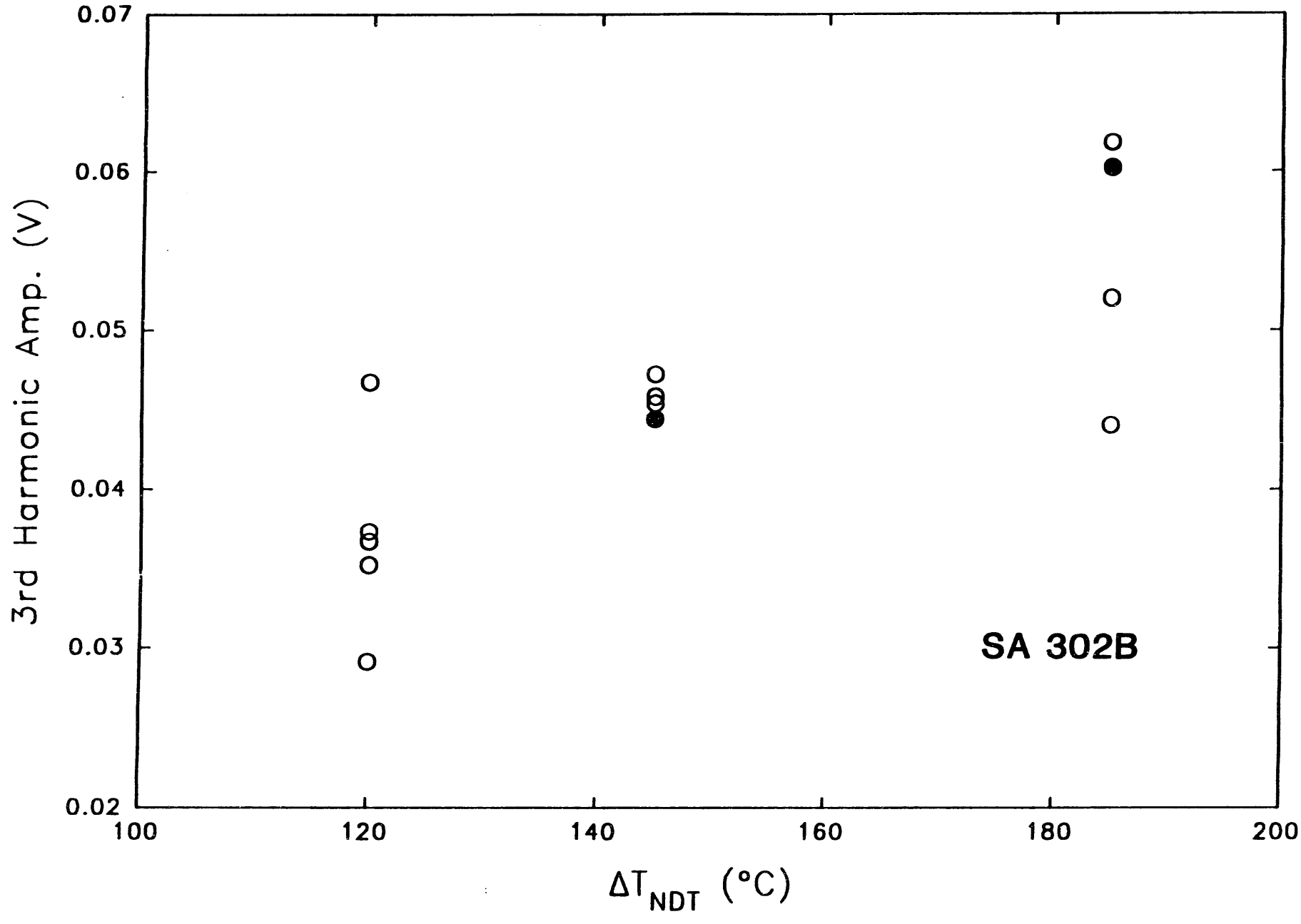

Fig. 13. Third harmonic amplitude vs. ΔT_{NDT} for Indian Point specimens at level H_{max} 2.

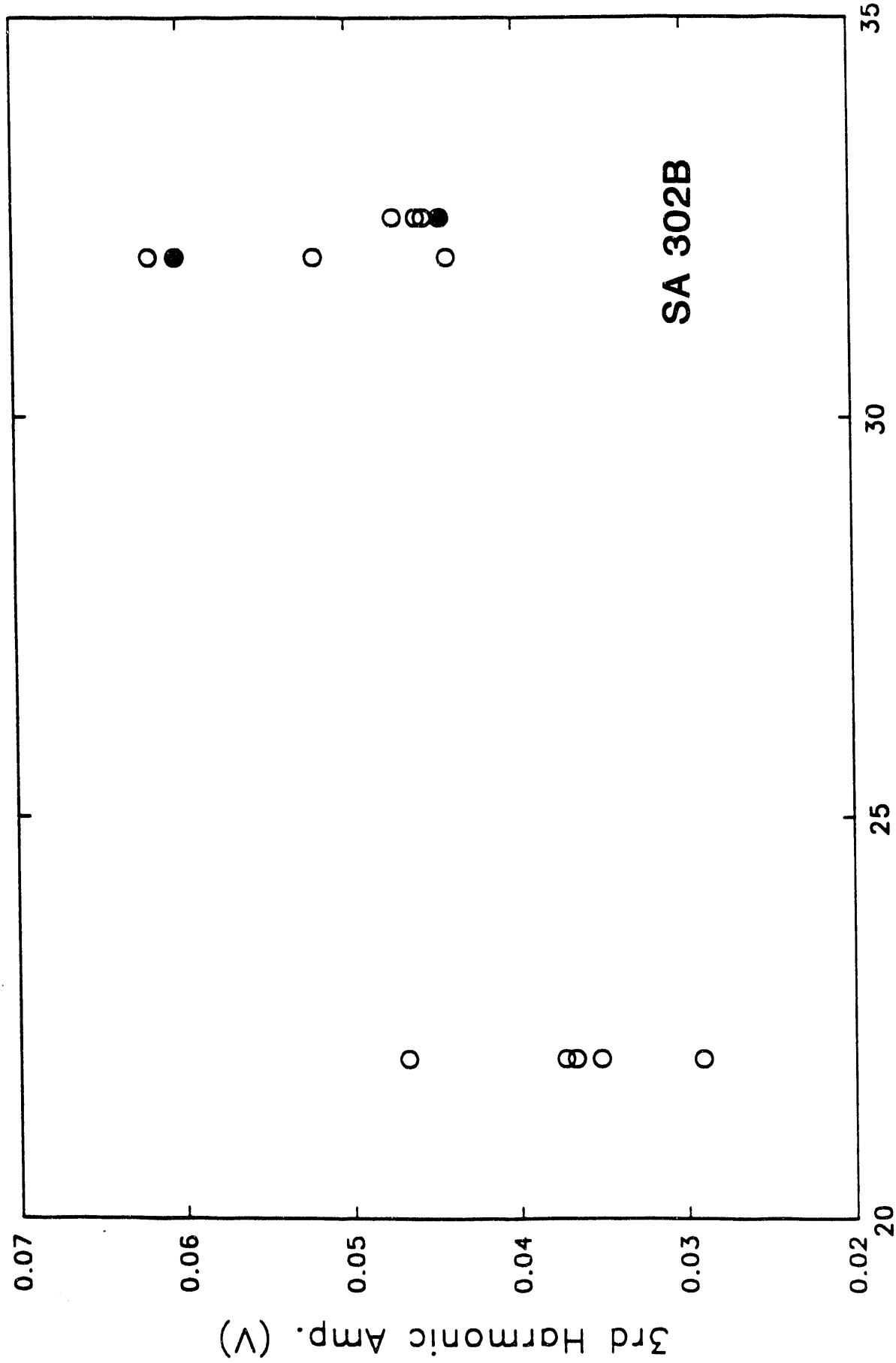

Fig. 14. Third harmonic amplitude vs. Δ(USE) for Indian Point specimens at level H_{max} 2.

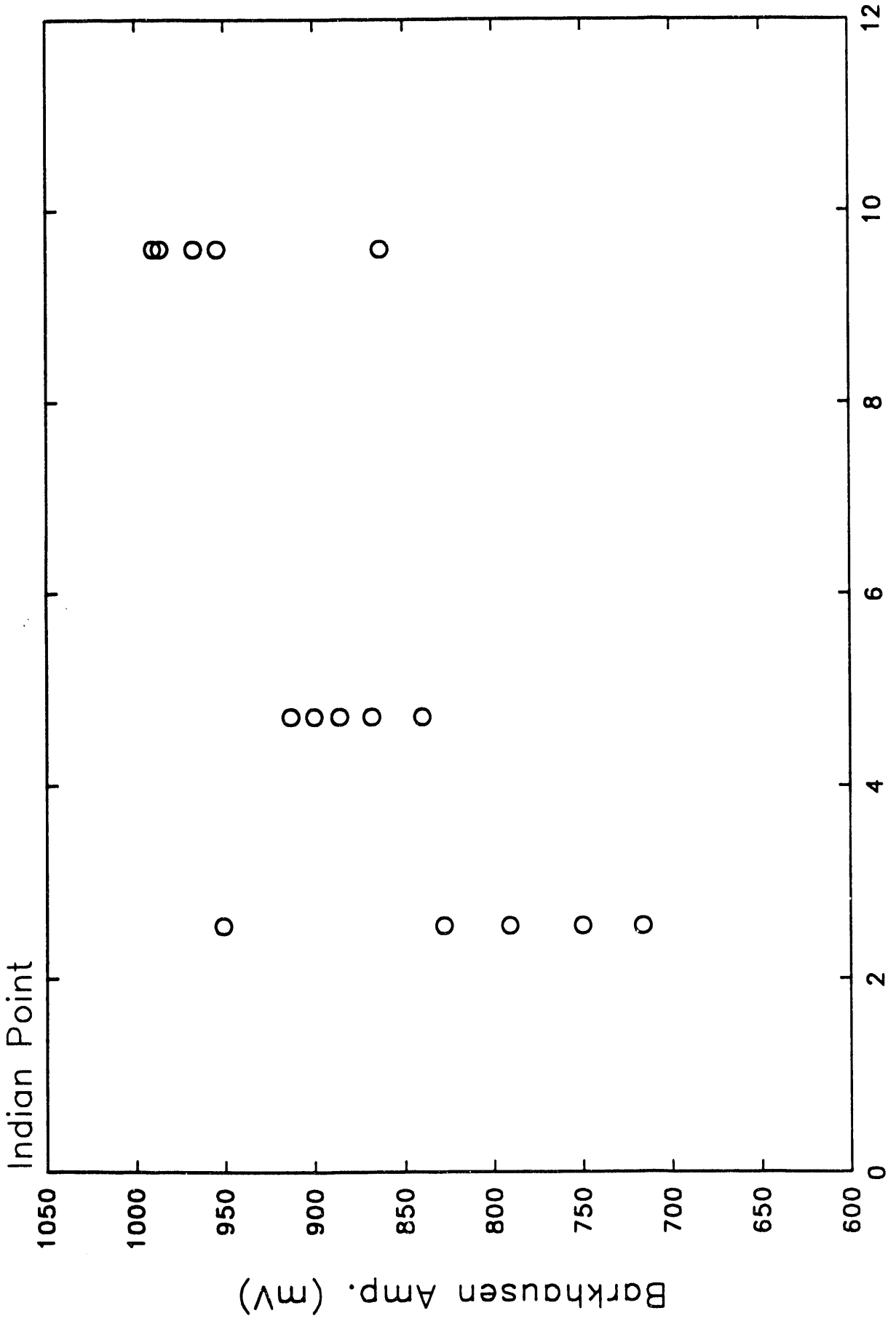

Fig. 15. Barkhausen noise (BN) amplitudes vs. fluence for Indian Point specimens.

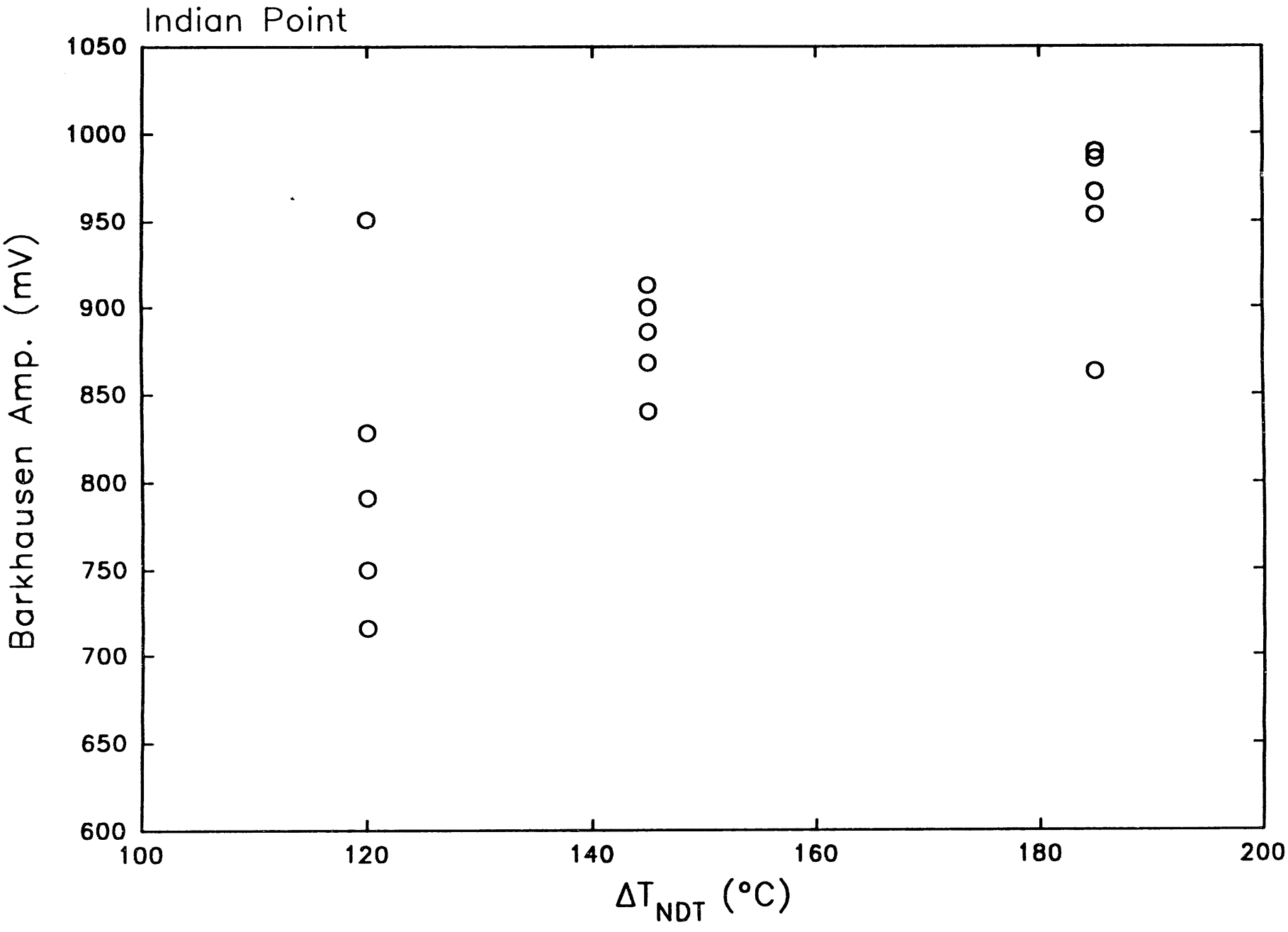

Fig. 16. BN amplitudes vs. ΔT_{NDT} for Indian Point specimens.

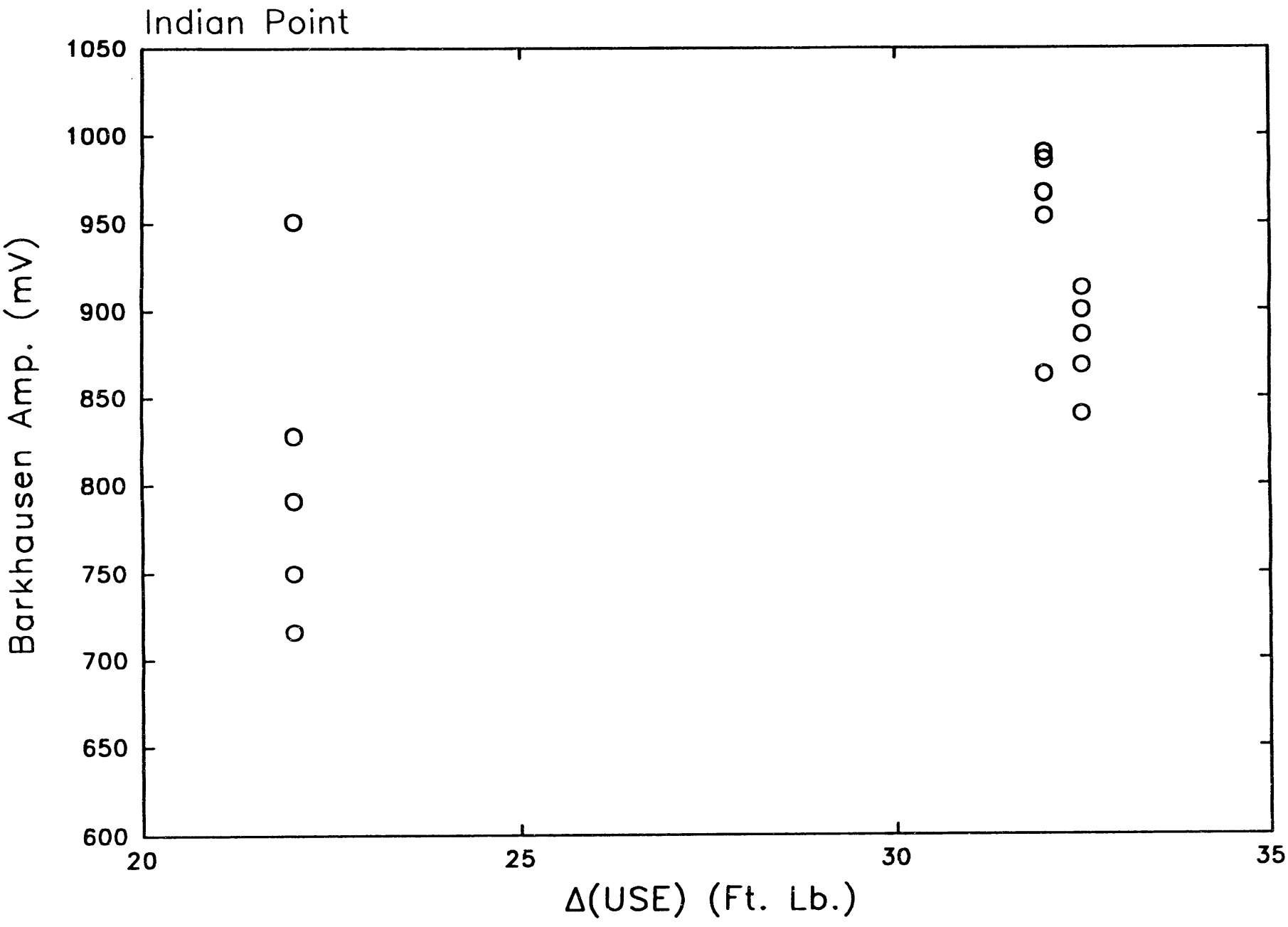

Fig. 17. BN amplitudes vs. Δ(USE) for Indian Point specimens.

ΔT_{NDT}, and Δ(USE) respectively. Clearly, the trends seen in Fig. 12 and 13 do not show up as clearly in the BN amplitudes. Perhaps, however, this can be understood in terms of the sensitivitity of Barkhausen noise to surface preparation. At the low frequencies used (~ 1Hz), the nonlinear harmonic amplitudes tend to reflect the condition of the bulk sample, whereas Barkhausen noise detection is much more influenced by the surface preparation. (The reason for the latter is that the Barkhausen noise detector filters out frequencies less than 1 kHz.) All irradiated samples have their surfaces buffed and sanded before Charpy tests are carried out. Thus, the buffed Charpy samples are less likely to show correlation of embrittlement with Barkhausen noise than the nonlinear harmonics.

b) D C Cook Unit 2 specimens

The response of the magnetic techniques to the specimens from the D.C. Cook 2 reactor did not correlate well with the fluence, Δ(USE), or ΔT_{NDT}. This is consistent with what we had reported in the interim report of Jan. 1992 for the smaller sample set of three (instead of five) samples per fluence level. The R^2 values for the D.C. Cook 2 reactor (see Table 6) are very low (in most cases zero) for all of the magnetic parameters. Typical data are shown in Figures 18, 19, and 20, which are plots of the third harmonic (magnetization level 2) vs. fluence, Δ(USE), and ΔT_{NDT}; the R^2 values are zero for all three parameters. (In contrast, the 3rd harmonic amplitude produced the best results for the Indian Point specimens). In all three plots, there is no discernable trend in the data compared to the degree of scatter in the 3rd harmonic values. Similar behavior is seen in plots of other magnetic properties vs. fluence, Δ(USE), and ΔT_{NDT} for the DC Cook Unit 2 specimens.

A possible reason for the low R^2 value for the D.C. Cook 2 (SA 533B steel) data, as compared to the Indian Point 2 (SA 302B steel) data, might be noticeable differences in chemical composition and heat treatment, which might result in lower levels of embrittlement. (Compare points 3 and points A in Figs. 4 and 5.) More importantly, such differences could also result in reduction of sensitivity of the magnetic parameters to embrittlement. Thus, for example, magnetic parameters for Indian Point 2 specimens show changes which are three to four times as large as that found for corresponding D.C. Cook 2 specimens. This is seen when comparing hysteresis loop changes for the two reactors for specimens at low and high fluence at the some H_{max} level (See Fig. 21 and 22). One sees that the changes in the hysteresis loop from low to high fluence are three to four times smaller for the DC Cook 2 reactor. When experimental error is added into consideration, one might expect D.C. Cook 2 specimens to have magnetic parameters which exhibit dramatically less correlation with fluence and embrittlement parameters.

Another point is that all the samples from a particular set of samples at a given fluence are assigned the same value of ΔT_{NDT} and Δ(USE), even though their individual embrittlements may actually differ in nature. The result is that the embrittlement factors that are assigned to individual samples should have a larger error in them than that assigned to the mean for the group. This is corroborated by the range of values found in the magnetic measurements, particularly in Fig. 18, 19, and 20, for groups of samples that are supposed to have the same ΔT_{NDT} or Δ(USE).

c) Summary of results

On a positive note, the moderate correlation found for the Indian Point 2 specimens suggests that for some pressure vessels, magnetic property measurement may be a potential way to monitor embrittlement in situ during down cycles or even possibly on an automated

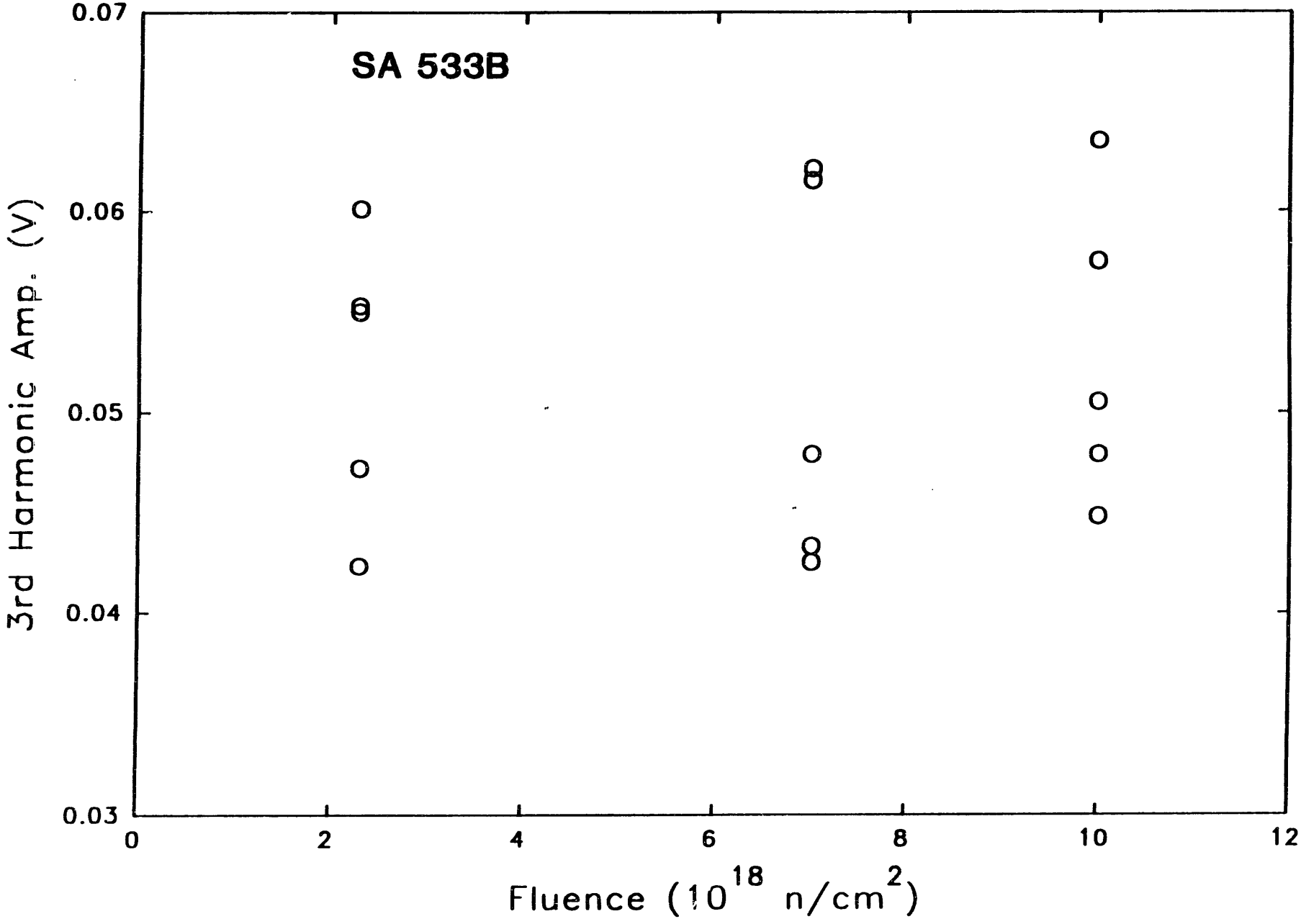

Fig. 18. Scatter plot for third harmoic amplitude (H_{max} level 2) vs. fluence for the DC Cook Unit 2 reactor.

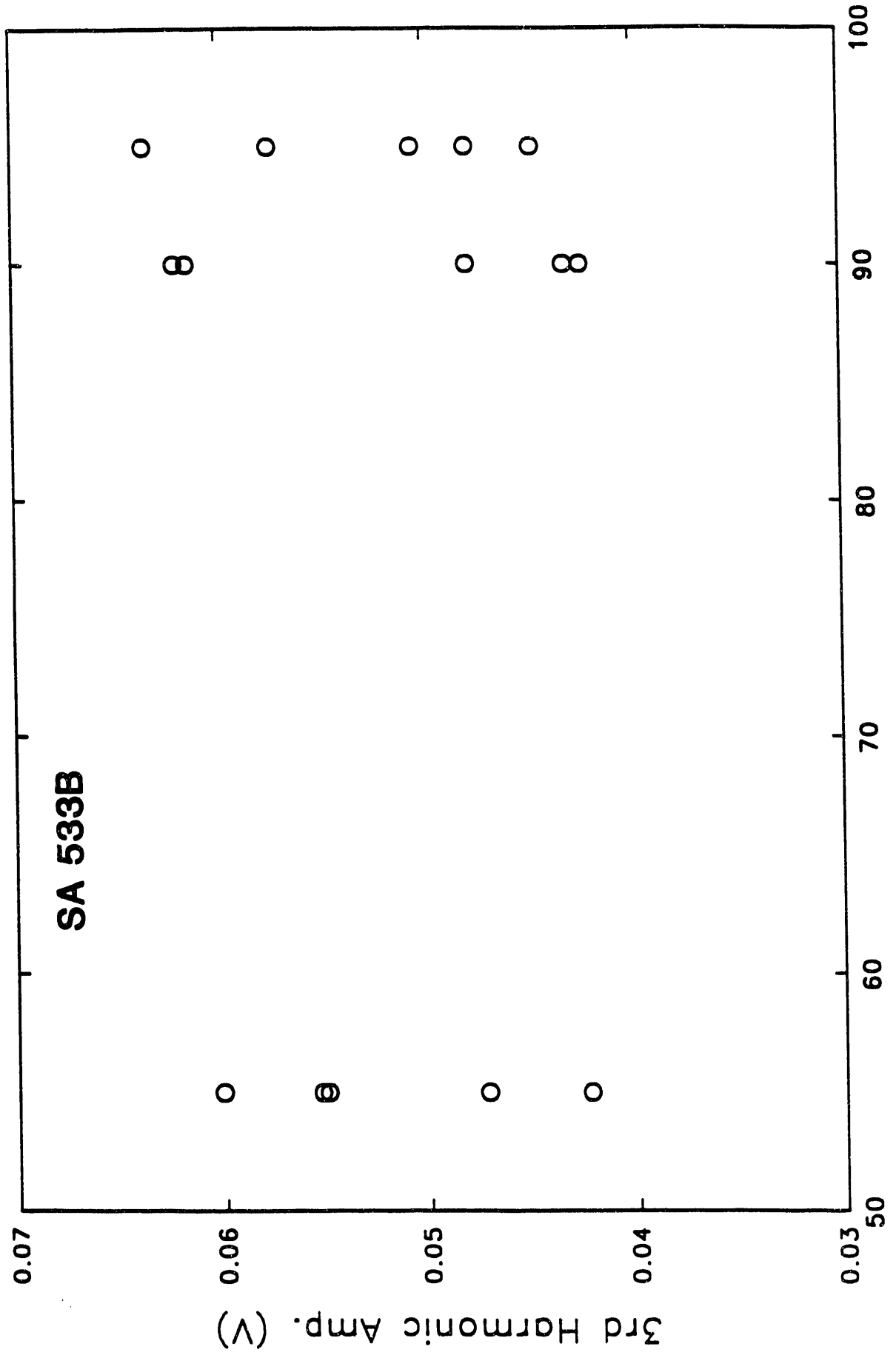

Fig. 19. Scatter plot for third harmonic amplitude (H_{max} level 2) vs. ΔT_{NDT} for the DC Cook Unit 2 reactor.

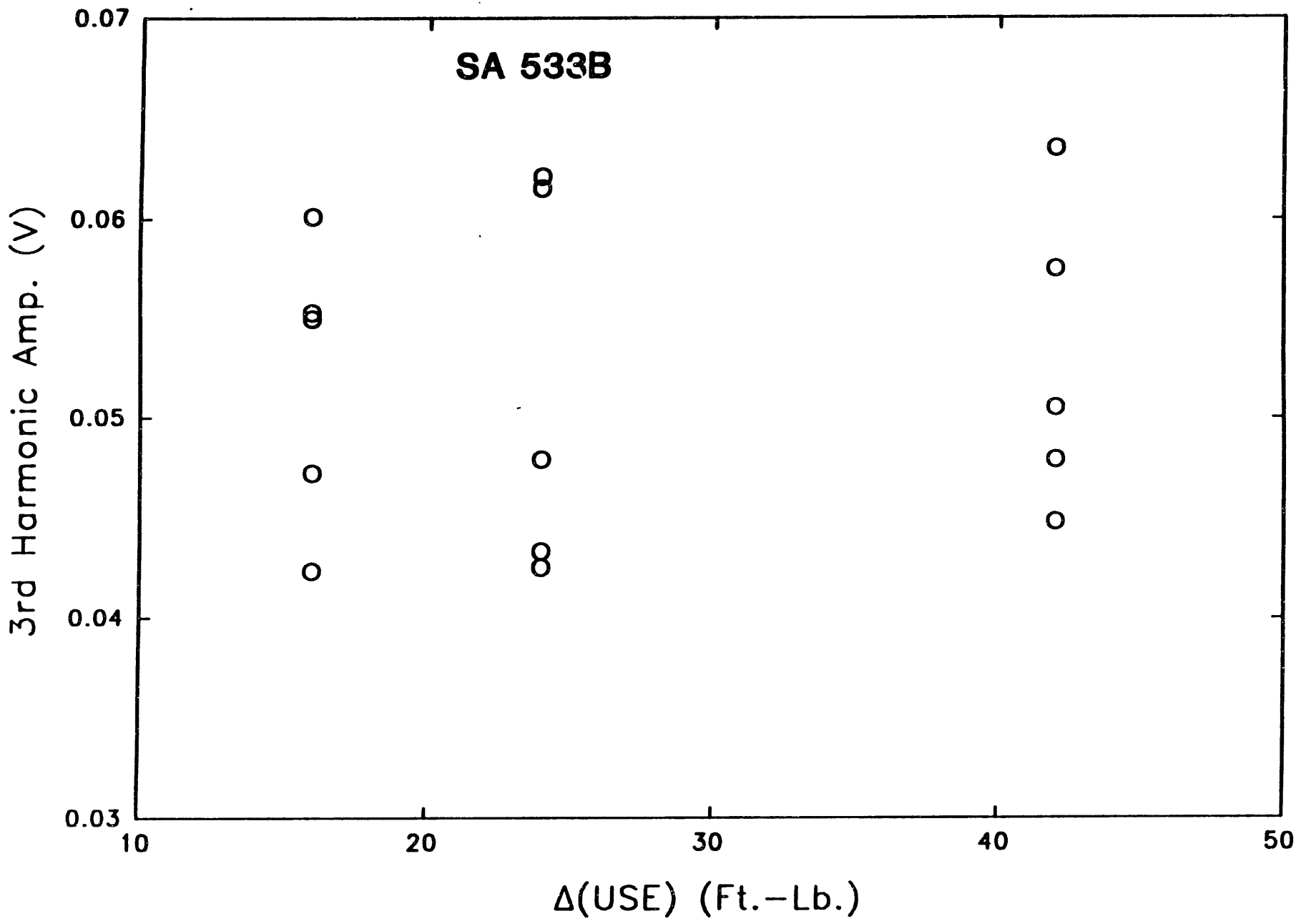

Fig. 20. Scatter plot for third harmonic amplitude (H_{max} level 2) vs. Δ(USE) for the DC Cook Unit 2 reactor.

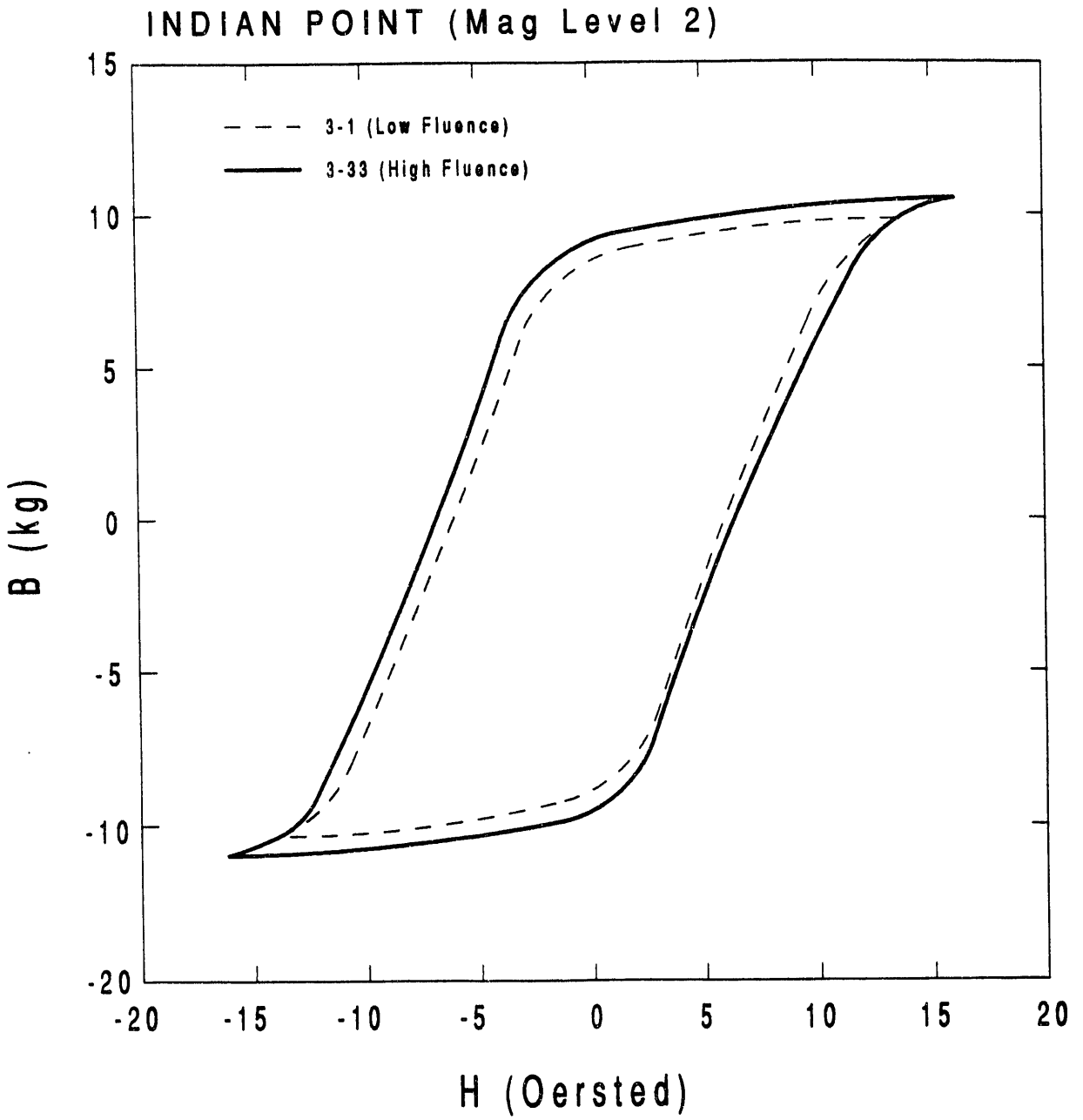

Fig. 21. Change in the hysteresis loop at H_{max} level 2 for the Indian Point 2 reactor in going from a specimen with low fluence to a specimen with high fluence.

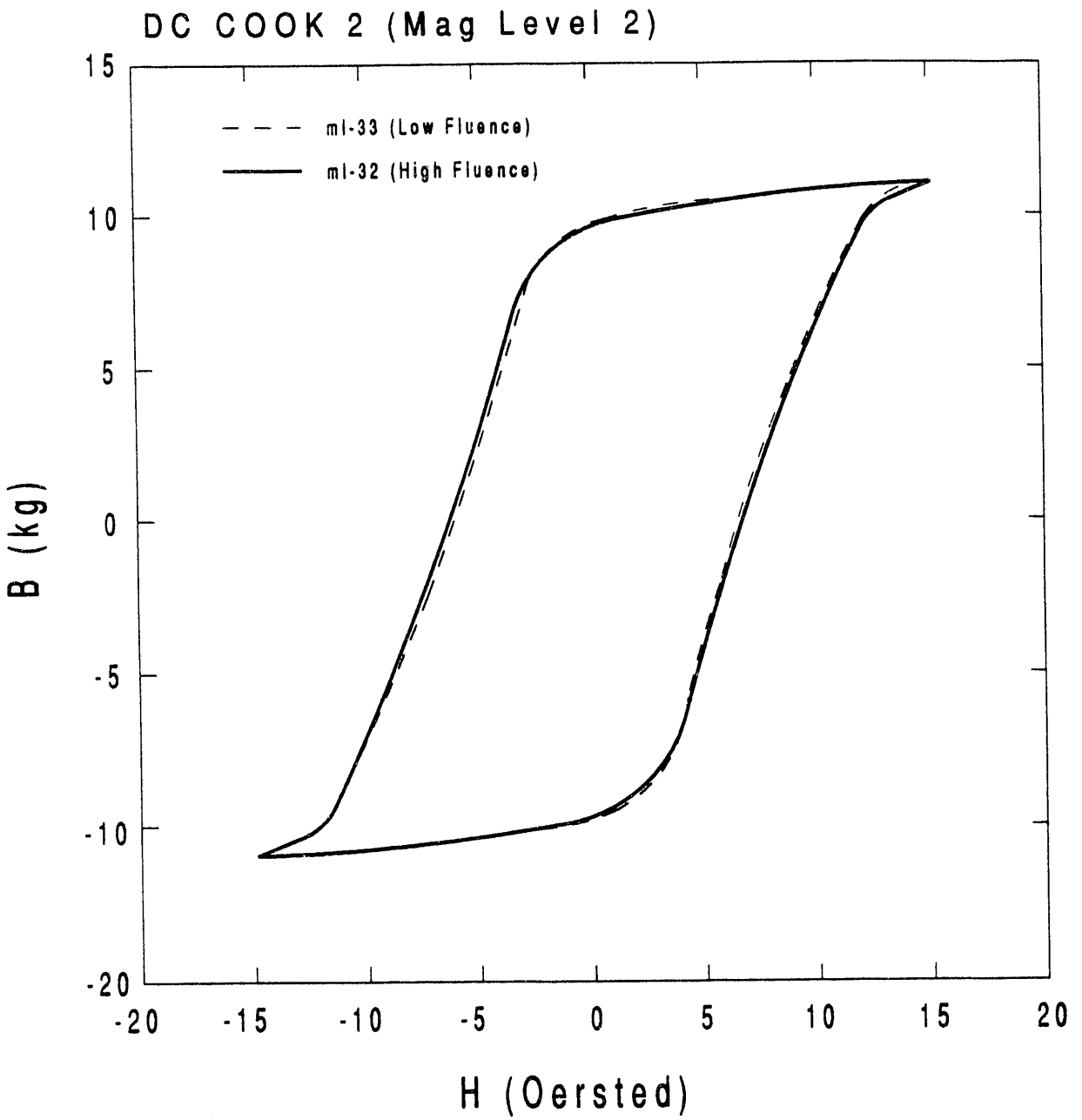

Fig. 22. Change in the hysteresis loop at H_{max} level 2 for the DC Cook 2 reactor in going from a specimen with low fluence to one with high fluence. Note that the change is considerably smaller than for the Indian Point 2 reactor.

basis while the reactor is running. However, a single measurement for a single sample will not be adequate. Average over a number of samples will be needed, at the very least.

The data so far suggests that the nonlinear harmonics technique (NLH) seems to offer the most potential for use in embrittlement monitoring. The physical theory is obviously challenged to explain why NLH is a better technique for monitoring embrittlement than hysteresis loop properties such as coercivity, remanence, or permeability at the coercive point.

A short paper on the hysteresis, NLH and BN measurements was presented at the Quantitative NDE Conference in San Diego, July 1992. A copy of this paper, which will be included in the conference proceedings, is given in Appendix 2.

2. Results from MIVC Measurements

Only the original 3 samples per fluence level were evaluated via MIVC measurements. Thus, in this case, 18 specimens were tested in all.

Examples of MIVC data acquired from irradiated specimens over a complete magnetic cycle are given in Figure 23 for longitudinal (top) and shear (bottom) waves, respectively. The data points represented by a solid line were from Indian Point specimen 3-1, and the data points represented by a dotted line were from D.C. Cook specimen ML-33. The MIVC data showed a hysteresis (which is caused by magnetic hysteresis of the material) and exhibited a typical butterfly shape (because the MIVC is dependent on the magnitude but not on the sign of applied magnetic field strength, H).

The MIVC data taken from all the other irradiated specimens were similar in shape and magnitude. Specimens from D.C. Cook Unit 2 generally showed a slightly higher MIVC magnitude than those from the Indian Point. Generally speaking, the MIVC magnitude at H = 100 Oe was on the order of 25 x 10^{-5} for S-waves and 9 x 10^{-5} for L-waves, respectively. Also, the repeatability of the MIVC measurements was $\pm 0.46 \times 10^{-5}$ for S-waves and $\pm 0.24 \times 10^{-5}$ for L-waves, respectively.

For the purpose of relating the measured MIVC data with the three properties of the irradiated specimens--namely, fluence, Δ(USE), and ΔT_{NDT}--the MIVC magnitudes at four different levels of H (20, 40, 60, and 80 Oersteds, respectively) were determined. To eliminate uncertainties associated with variations in shape of the MIVC curve and with offset from the zero point, all magnitudes were calculated from the minimum point of the MIVC curve. The values of the magnitudes are listed in Table 7.

Using a linear regression statistical model, the MIVC magnitudes were correlated with the properties of the irradiated specimens and the correlation coefficient, R , was calculated, again as in Appendix 1. Table 8 displays the R^2 values thus determined.

Overall, the MIVC data did not correlate well with all three properties of the irradiated specimens from both Indian Point and DC Cook reactors. All R^2 values were less than 0.5, and many were close to zero. The best correlation shown by the DC Cook specimens was between upper-shelf energy change Δ(USE) and L-wave MIVC magnitudes at H = 20 and 40 Oersteds, whose R^2 values were on the order of 0.4. As for the Indian Point specimens, the best correlation was between

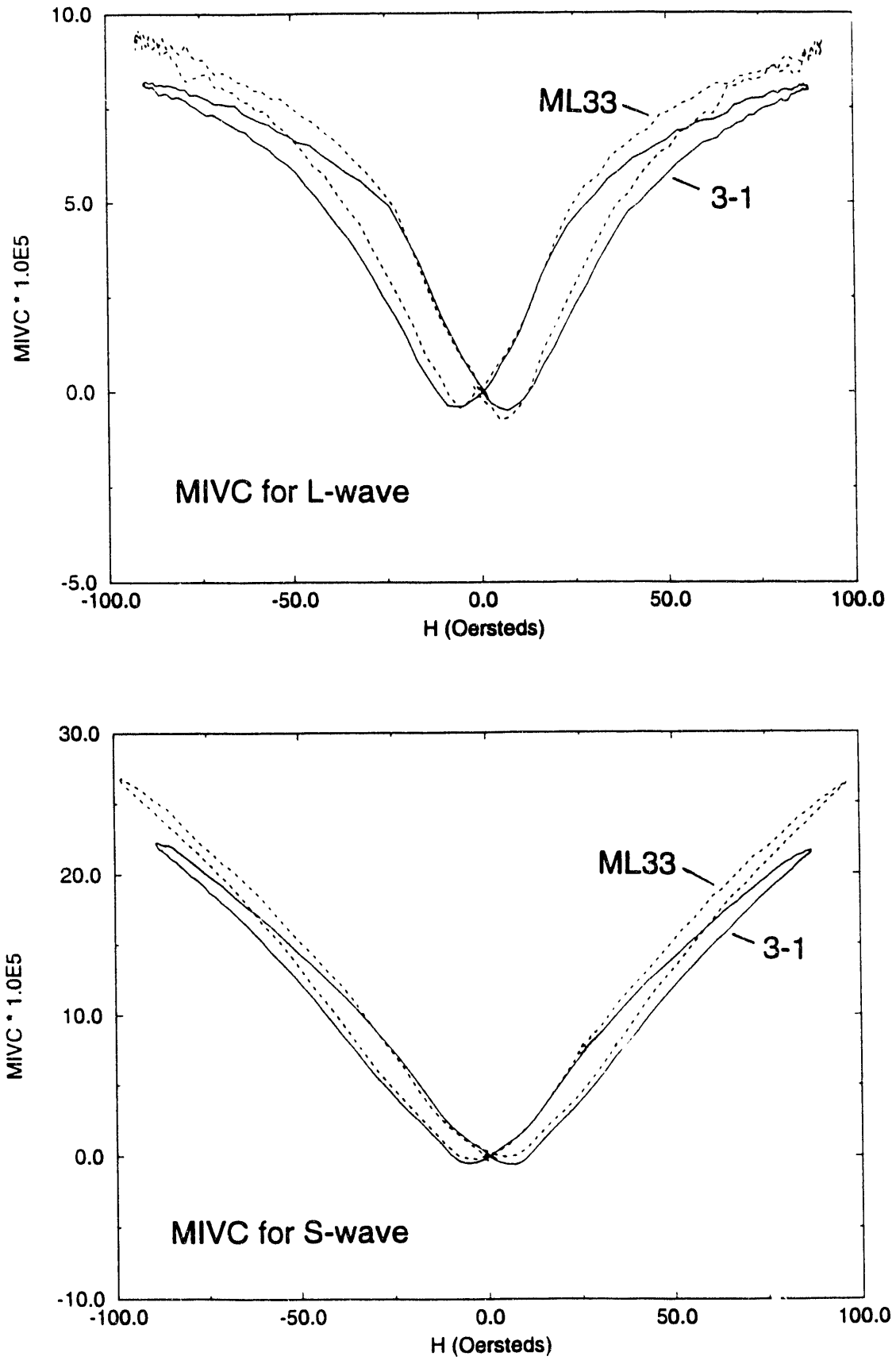

Fig. 23. MIVC plotted as a function of magnetic field strength H for L-waves (top) and S-waves (bottom). The dotted lines are the data taken from DC Cook 2 specimen ML33; The solid lines are the data taken from Indian Point specimen 3-1.

TABLE 7
MIVC MAGNITUDES AT FOUR LEVELS OF H

Reactor	Wave Mode	Specimen	H Level (Oe)			
			20	40	60	80
DC Cook Unit 2	S-Wave	ML25	4.31	11.98	18.84	24.39
		ML26	3.89	10.55	17.55	23.25
		ML32	4.26	11.24	17.97	23.53
		ML33	4.01	10.61	16.82	22.01
		ML39	4.21	11.23	17.74	23.14
		ML40	5.29	12.69	19.54	25.06
		ML52	4.68	11.67	18.02	23.29
		ML54	4.99	11.91	18.45	23.98
		ML55	5.12	12.47	18.61	23.71
	L-Wave	ML25	2.23	5.90	7.87	9.00
		ML26	2.07	5.78	7.88	9.00
		ML32	2.25	5.65	7.74	9.01
		ML33	2.53	5.95	8.05	9.10
		ML39	2.94	6.37	8.22	9.03
		ML40	2.38	5.93	7.80	8.77
		ML52	2.99	6.19	8.05	9.13
		ML54	2.47	5.89	7.77	8.95
		ML55	2.85	6.21	7.75	9.12
Indian Point	S-Wave	3-1	3.32	9.45	15.53	20.53
		3-3	4.28	10.56	16.69	21.61
		3-33	5.21	12.03	18.19	23.19
		3-36	3.62	9.57	15.55	20.53
		3-40	3.62	9.49	16.06	21.56
		3-41	5.45	12.33	18.51	23.54
		3-46	4.36	10.70	16.18	20.74
		3-47	4.79	11.54	17.44	22.26
		3-8	2.96	8.57	15.27	20.86
	L-Wave	3-1	1.84	5.24	7.10	8.17
		3-3	1.99	5.17	6.98	8.06
		3-33	1.85	5.22	6.91	8.01
		3-36	1.84	5.12	6.94	7.99
		3-40	1.37	4.48	6.65	7.99
		3-41	1.91	5.10	6.83	7.94
		3-46	2.54	5.43	6.81	7.75
		3-47	2.67	5.54	7.17	8.08
		3-8	1.54	4.68	6.68	7.85

*MIVC magnitudes are in 10^{-5} units

Table 8. SQUARE OF CORRELATION COEFFICIENT (R^2) FOR MIVC MAGNITUDES

Wave Mode	H Level (Oe)	Indian Point			DC Cook Unit 2		
		Fluence	Δ (USE)	ΔT_{NDT}	Fluence	Δ(USE)	ΔT_{NDT}
L-Wave	20	0.07	0.10	0.04	0.24	0.45	0.09
	40	0.05	0.04	0.04	0.28	0.42	0.15
	60	0.06	0.01	0.06	0.27	0.20	0.29
	80	0.00	0.08	0.00	0.04	0.00	0.08
S–Wave	20	0.03	0.35	0.06	0.05	0.18	0.00
	40	0.02	0.31	0.04	0.01	0.05	0.00
	60	0.03	0.25	0.05	0.00	0.00	0.01
	80	0.04	0.19	0.06	0.03	0.02	0.03

Fig. 24. Examples of correlation plots. Top is L-wave MIVC amplitude at H = 40 Oe vs. change in upper shelf energy of DC Cook 2 specimens. Bottom is S-wave MIVC ampliutde at H = 40 Oe vs. change in upper shelf energy of Indian Point 2 specimens. Change in upper shelf energy is in units of ft.-lbs.

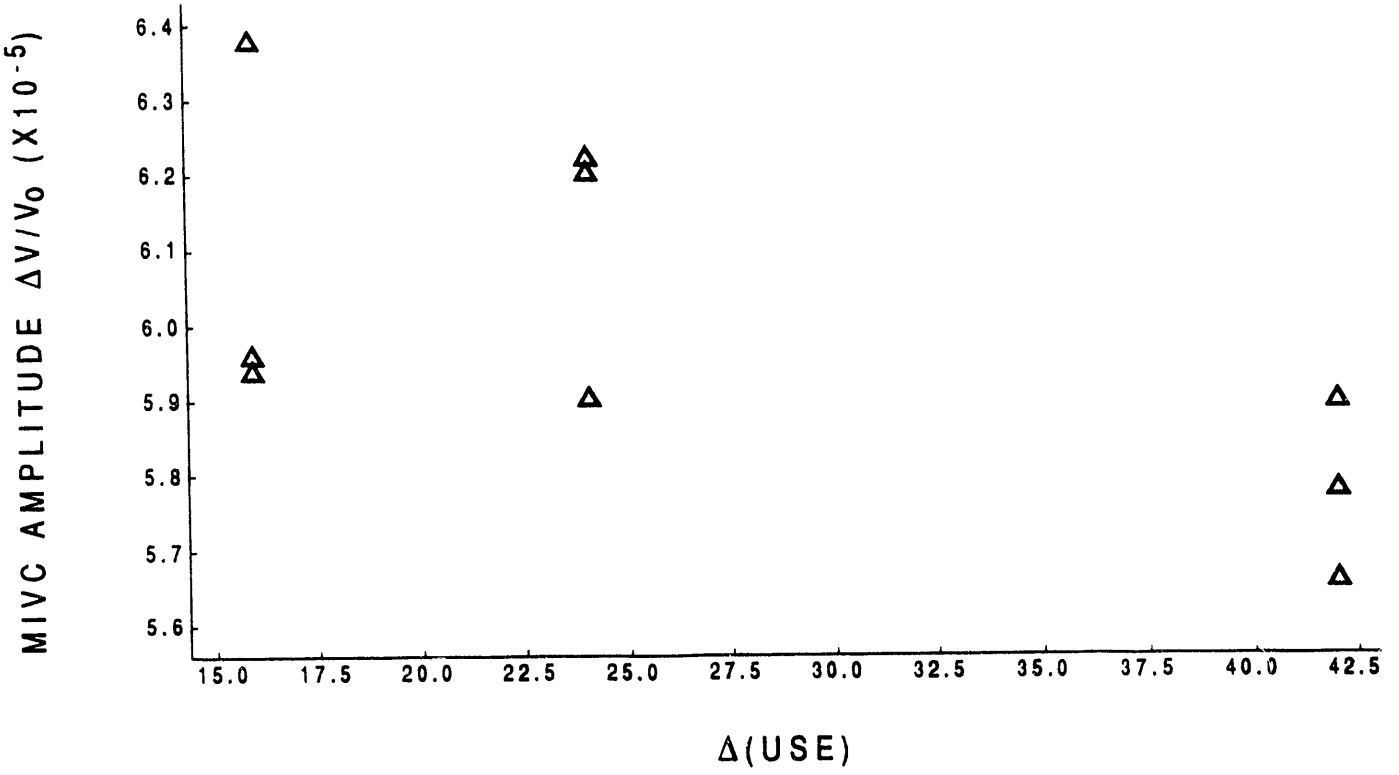

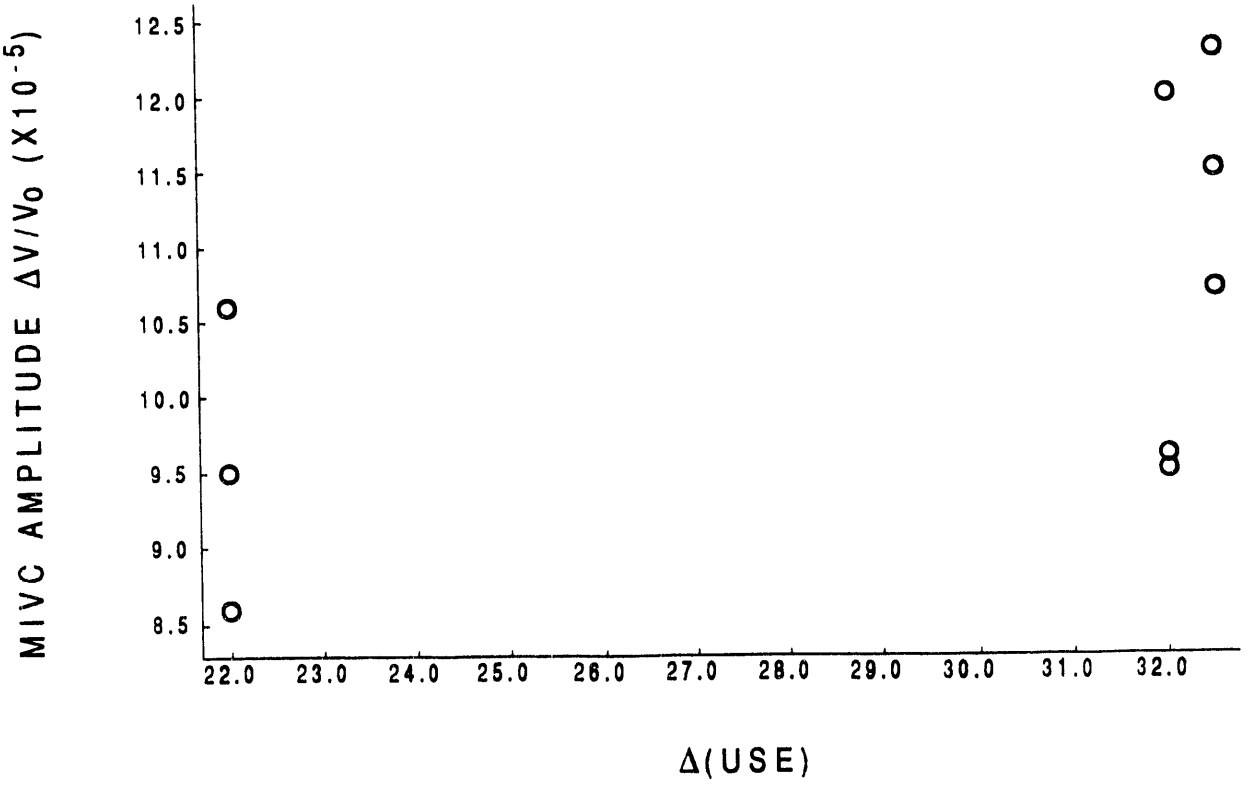

Δ(USE) and S-wave MIVC magnitudes at H = 20 and 40 Oersteds with R^2 values on the order of 0.3. Figure 24 shows some examples of the correlation plots. The top plot in Figure 24 shows the relation between the L-wave MIVC magnitude at H = 40 Oersteds and Δ(USE) of DC Cook specimens. The bottom plot in Figure 24 shows the relation between the S-wave MIVC magnitude at H = 40 Oersteds and Δ(USE) of Indian Point specimens.

In the examples shown in Figure 24, the L-wave MIVC amplitude decreases with increasing upper-shelf energy whereas the S-wave MIVC amplitude increases with increasing upper-shelf energy. Because of the large scatter in data among the specimen which experienced the same neutron fluence and the fact that the amount of change which could be attributable to the irradiation damage was only slightly larger than the measurement repeatability itself, the validity of the above trend is not conclusive.

It can be concluded from the above results that the MIVC appears nearly insensitive to irradiation-related changes in material properties.

3. Results from Magabsorption Measurements

In this case, the peak-to-peak amplitude of the waveform traced on the oscilloscope was recorded for each of the 30 specimens. The measurements were made three times, starting with the first specimen and working to the last specimen each time. Clearly, the probe was repositioned on the specimen for each measurement, and the three sets of measurements can be considered independent of each other.

Table 9 shows the data from the three sets of measurements. A peak-to-peak value is recorded for when the probe was aligned with its bias magnetic field (a) parallel and (b) perpendicular to the long axis of the specimen. The top half of the table (for specimens 3-xx) is for the Indian Point 2 reactor; the bottom half (for specimens ML-xx) is for DC Cook 2.

Table 10 displays the R^2 values for magabsorption amplitudes vs. fluence, ΔT_{NDT}, and Δ(USE) respectively for the two reactors. The R^2 values for the three independent runs are first shown separately and then for all the three runs together. Separate R^2 values are shown for when the probe was aligned with its bias field (a) parallel and (b) perpendicular to the long axis of the specimen.

The R^2 values are all relatively low, varying from a maximum of 0.46 (for the perpendicular peak-to-peak voltage (ppv) against Δ(USE) in run #3 for DC Cook 2) to 0.0 (for the parallel ppv against fluence in run #3 for Indian Point 2). The R^2 values for magabsorption amplitudes in the perpendicular case appeared to be slightly larger than for the parallel case.

Examples of magabsorption scatter plots are shown in Figs. 25 and 26. Fig. 25 is for Run #1 magabsorption peak-to-peak voltage (ppv) amplitudes against (a) fluence, (b) ΔT_{NDT}, and (c) Δ(USE) in the case where the bias magnetic field is parallel to the long axis of the specimen. Figs. 26 displays similar Run #1 plots for the case where the bias field is perpendicular to the long axis of the specimen. Both Indian Point 2 points (circles) and DC Cook 2 points (triangles) are plotted on the same plot. Hashed lines are drawn to show the overall trend of the Indian Point 2 data. Dotted lines are used to show the trend of the limits of the DC Cook 2 data. It should be clear that in Run #1 the scatter in the DC Cook 2 data is greater than in the Indian Point 2 data, both for the

Table 9. Peak-to-peak magabsorption amplitudes for irradiated broken Charpy samples from Indian Point 2 (3-n specimens) and DC Cook 2 (ML-n specimens). Peak-to-peak amplitudes are given for when the bias magnetic field of the probe is aligned parallel and perpendicular to the long axis of the specimen. Results from 3 independently performed sets of measurements are shown.

Specimen	Run #1		Run #2		Run #3		Fluence
	ppv (‖) (mv)	ppv (⊥) (mv)	ppv (‖) (mv)	ppv (⊥) (mv)	ppv (‖) (mv)	ppv (⊥) (mv)	(n/cm^2)
3–1	1.225	0.955	1.245	0.920	1.230	0.930	
3–3	1.185	0.980	1.175	1.040	1.205	0.965	
3–6	1.110	1.000	1.125	1.110	1.150	1.010	2.55×10^{18}
3–7	1.160	1.085	1.130	1.075	1.155	0.935	
3–8	1.180	0.960	1.130	1.010	1.205	0.940	
3–33	1.270	0.955	1.270	0.945	1.255	0.945	
3–34	1.200	0.915	1.200	0.940	1.205	0.860	
3–35	1.165	1.010	1.180	0.875	1.140	0.890	4.72×10^{18}
3–36	1.265	0.930	1.260	0.930	1.245	0.890	
3–40	1.215	0.910	1.165	0.975	1.145	0.870	
3–41	1.260	0.955	1.260	0.910	1.265	0.945	
3–45	1.150	0.985	1.160	1.045	1.155	0.850	
3–46	1.230	0.910	1.190	0.995	1.195	0.900	9.6×10^{18}
3–47	1.225	0.920	1.235	0.940	1.250	0.945	
3–48	1.130	0.945	1.145	1.015	1.155	0.855	
ML–25	1.230	0.980	1.230	0.965	1.220	0.870	
ML–26	1.095	0.610	1.090	0.660	1.085	0.655	
ML–28	1.050	0.890	1.010	0.805	1.005	0.780	2.3×10^{18}
ML–30	1.045	1.010	1.010	0.730	1.015	0.755	
ML–32	1.170	0.815	1.160	0.805	1.155	0.740	
ML–33	1.190	0.825	1.200	0.820	1.155	0.845	
ML–36	1.055	1.050	1.075	0.900	1.095	0.935	
ML–37	1.085	1.030	1.050	0.905	1.080	0.900	7.01×10^{18}
ML–39	1.170	0.980	1.155	0.945	1.160	0.865	
ML–40	1.230	0.885	1.210	0.855	1.215	0.850	
ML–49	1.070	1.105	1.050	0.910	1.020	0.900	
ML–52	1.205	0.815	1.210	0.750	1.180	0.775	
ML–53	1.145	1.085	1.110	0.900	1.130	0.845	
ML–54	1.145	0.865	1.150	0.830	1.135	0.825	1.0×10^{19}
ML–55	1.220	0.975	1.190	0.885	1.225	0.900	

Table 10. R^2 values for magabsorption peak-to-peak amplitudes for three independent sets of measurements (15 specimens total for each reactor) and for the total of the three sets (45 measurements total per reactor) as correlated against fluence, ΔT_{NDT} and Δ(USE).

Parallel		Run #1	Run #2	Run #3	Total
Indian Point 2	vs. fluence	0.18	0.17	0.00	0.09
	vs. ΔT_{NDT}	0.19	0.18	0.01	0.10
	vs. Δ(USE)	0.14	0.18	0.02	0.10
DC Cook 2	vs. fluence	0.02	0.04	0.06	0.04
	vs. ΔT_{NDT}	0.01	0.02	0.03	0.02
	vs. Δ(USE)	0.04	0.06	0.08	0.03
Perpendicular		Run #1	Run #2	Run #3	Total
Indian Point 2	vs. fluence	0.16	0.36	0.28	0.20
	vs. ΔT_{NDT}	0.18	0.38	0.31	0.22
	vs. Δ(USE)	0.30	0.28	0.41	0.24
DC Cook 2	vs. fluence	0.07	0.20	0.39	0.13
	vs. ΔT_{NDT}	0.03	0.15	0.28	0.09
	vs. Δ(USE)	0.12	0.22	0.46	0.17

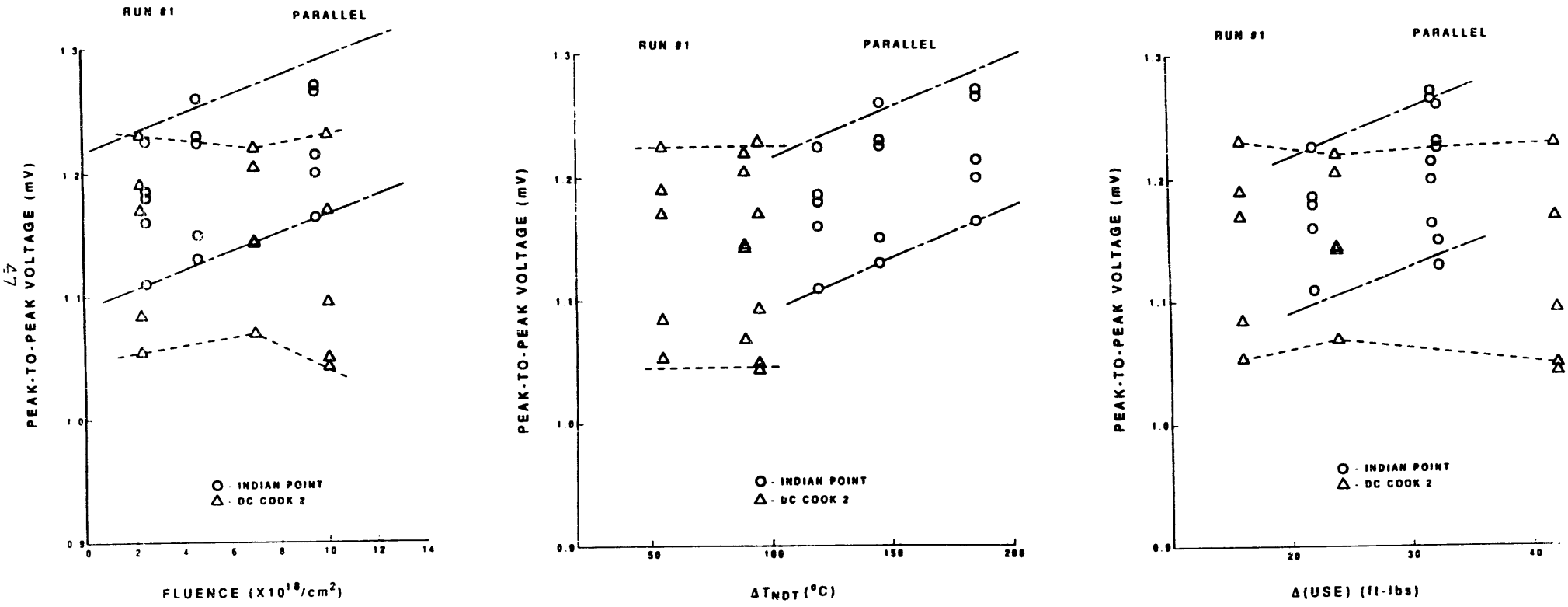

Fig. 25. Scatter plots for Run #1 for magabsorption peak-to-peak voltage (ppv). Hashed lines show the limits found for Indian Point 2 data; dashed lines, DC Cook 2 data. The data is for the case where the probe is parallel to the long axis of the specimen. The three plots represent magabsorption ppv vs. (a) fluence, (b) ΔT_{NDT}, and (c) Δ(USE).

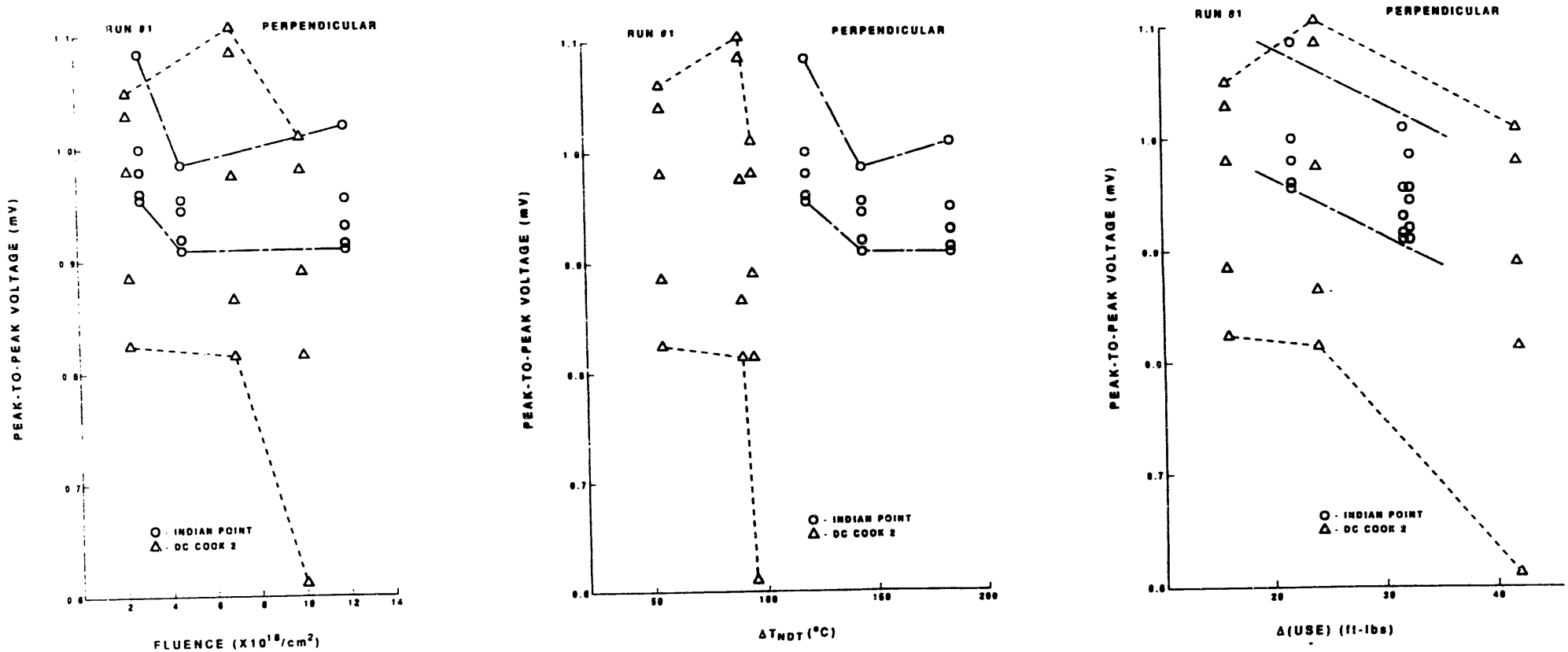

Fig. 26. Scatter plots for magabsorption ppv. Here the probe is aligned perpendicular to the long axis of the specimen. Data is again for Run #1. Again, the three plots represent magabsorption ppv vs. (a) fluence, (b) ΔT_{NDT}, and (c) Δ(USE).

parallel case and the perpendicular case. Also, a clearer trend is seen in the ppv amplitude vs. Δ(USE) data for Indian Point 2 than is seen in ppv amplitude vs. ΔT_{NDT} or ppv amplitude vs. fluence, which accounts for why R^2 is larger for the Δ(USE) case. In all cases, however, there is too much scatter in the data for the magabsorption technique to be considered a reliable indicator of amount of embrittlement.

One reason why magabsorption did not exhibit a good indication of embrittlement is that the modulated rf signal is at 225 kHz. The signal therefore senses only what is at the surface because of the skin depth effect. Too much had happened to the surface of the broken Charpy sample by the time the magabsorption measurement was done. The surface had been buffed and sanded prior to Charpy testing. The surface stresses had changed under Charpy impact. Thirdly, the surface had to be buffed again to remove traces of the honey couplant used for MIVC measurements.

These measurements can be contrasted with the previous work done earlier at SwRI[33] which indicated magabsorption as a potential indicator of embrittlement. The irradiated samples used for the previous measurements had been unbroken Charpy samples. The surfaces of those specimens were untreated after removal from the reactor. Fig. 27 exhibits a plot of parallel vs. perpendicular magabsorption amplitudes for the previous samples tested at SwRI; a distinct shift in the data is seen for the irradiated samples. Fig. 28 shows the same plot for Run #1 data. In the present data (Fig. 28), no distinct separation occurs for different amounts of radiation, nor is there a distinct separation between DC Cook 2 data (triangles) and Indian Point 2 data (circles). The magabsorption measurements would therefore potentially be useful only in testing unbroken, unbuffed Charpy samples. This might be said actually for all the magnetic measurements. It would be important to repeat all of the previous magnetic tests, but this time on unbroken, unbuffed, irradiated Charpy samples if enough of these samples can be secured from other sources.

D. Summary of Experimental Observations and Recommendations

Our major conclusions, based on the experimental data on broken Charpy specimens, are the following:

1) For SA533B specimens from the DC Cook 2 reactor, magnetic properties did not correlate well with fluence or other embrittlement parameters. This is probably due to (a) the scatter in the embrittlement parameters from one individual specimen to the next and (b) the relative insensitivity of the magnetic properties of SA533B steel to embrittlement.

2) For SA302B specimens from the Indian Point 2 reactor, a moderate correlation ($R^2 \sim 0.6 - 0.7$) was found for nonlinear harmonic amplitudes. The correlation needs to be checked with a yet larger sample set, since even better correlation was found originally ($R^2 \sim 0.9$) with a small sample set. The correlation of $R^2 \sim 0.6 - 0.7$ means that a single measurement would not be a reliable measure of embrittlement, but an average over a number of samples with nominally the same fluence may turn out to be a fairly good indicator of embrittlement for the whole set of samples.

3) Also, for the SA302B specimens, typical hysteresis parameters such as coercivity, remanence, or permeability at the coercive point (which is determined with least

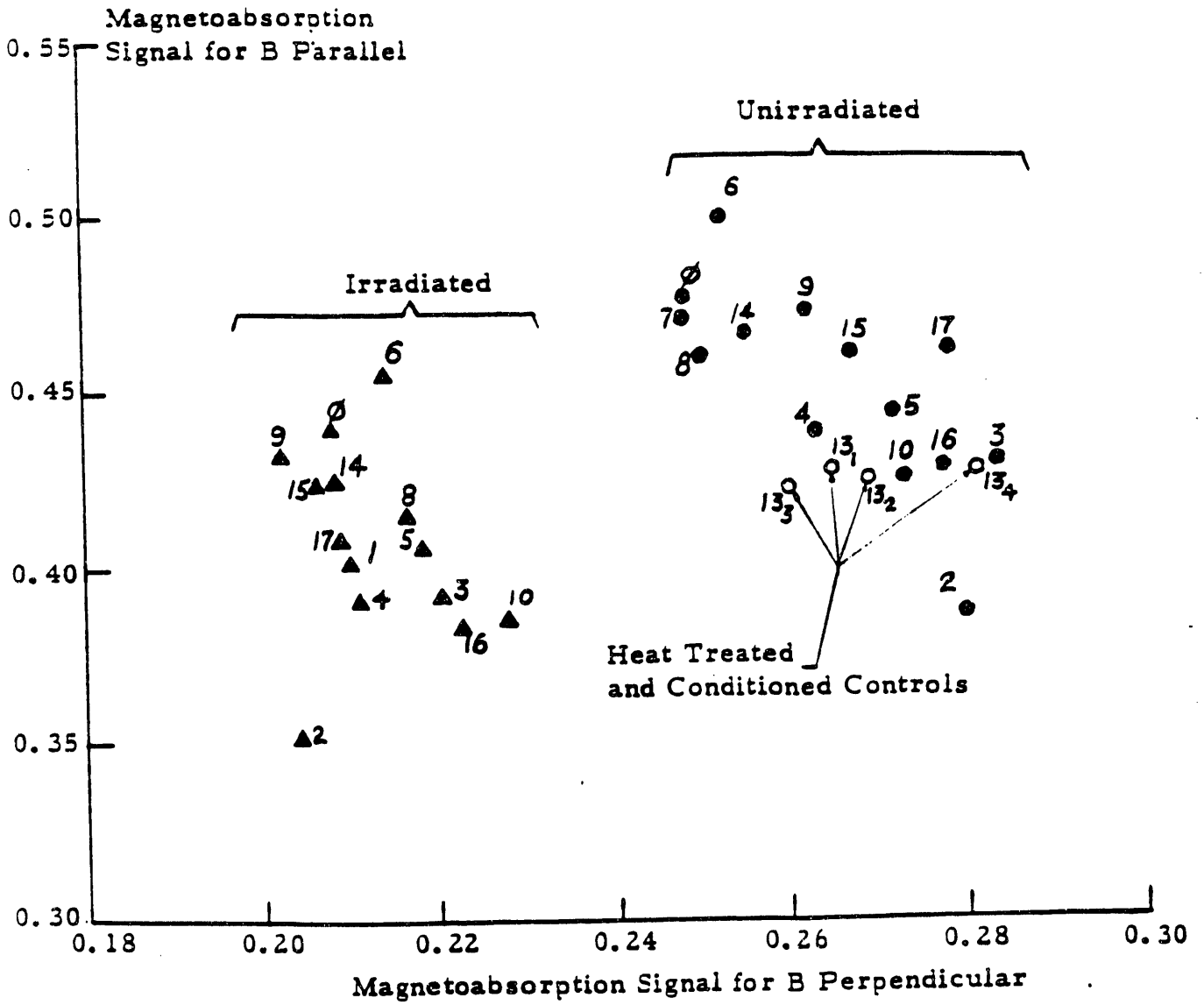

Fig. 27. Graph of the magabsorption signals in ref. 33 for the bias flux density B both parallel and perpendicular to the face of Charpy specimens taken before and after irradiation of the same samples.

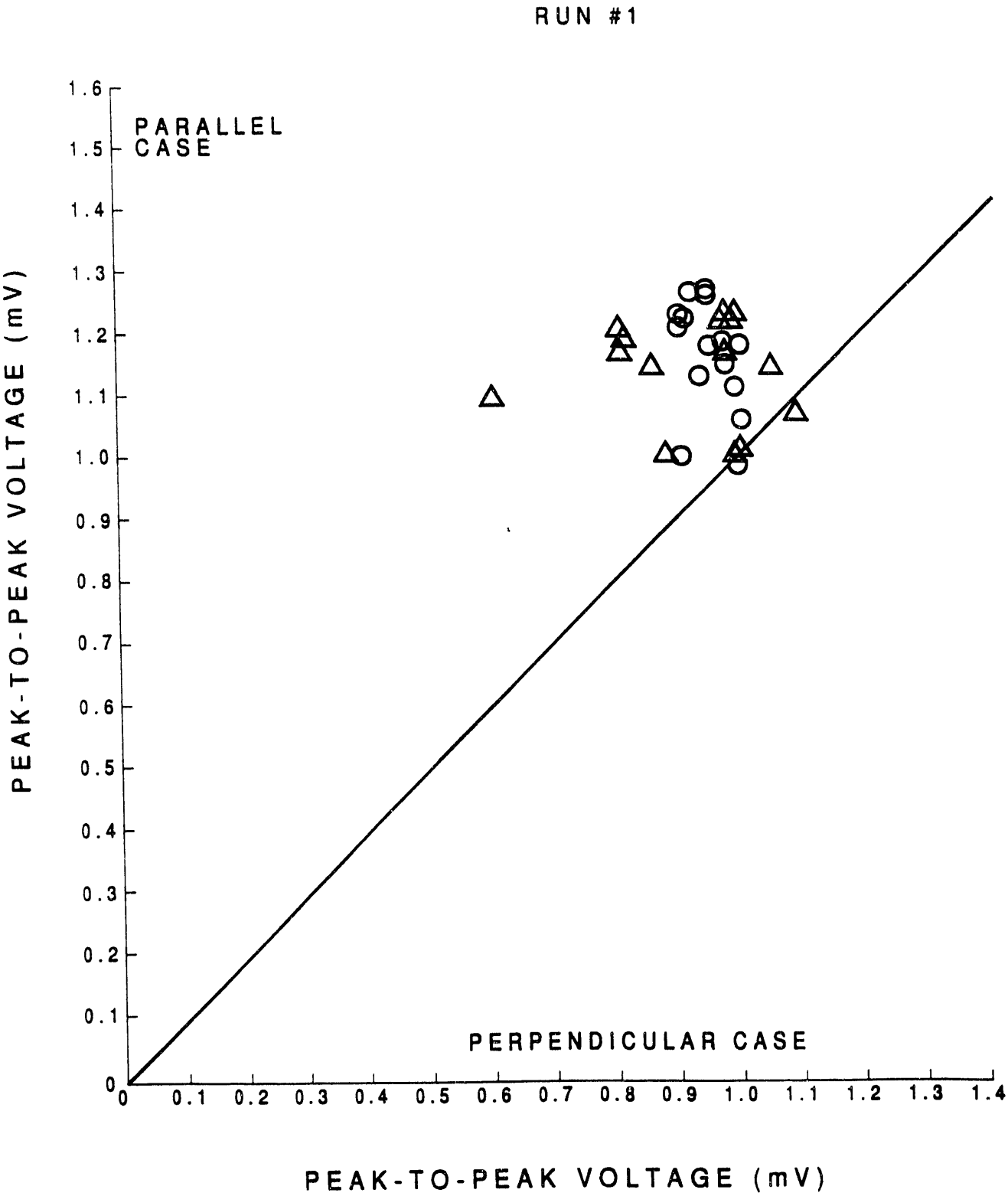

Fig. 28. Scatter plot displaying magabsorption ppv magnitudes in the parallel case vs. magabsorption ppv magnitudes in the perpendicular case. Circles are for Indian Point 2 data; triangles, DC Cook 2 data. No distinct separation occurs between specimens from the different fluence levels nor between Indian Point 2 and DC Cook 2 data. This is attributed to treatment sustained by the sample surface subsequent to irradiation.

precision) did not correlate well at all with embrittlement parameters. Barkhausen noise exhibited less than the moderate correlation seen with the nonlinear harmonic amplitudes possibly because Barkhausen noise is more sensitive to the buffed and sanded surface preparation of the Charpy samples.

4) Magnetization level did not significantly affect the correlation results.

5) Two other techniques - MIVC and magabsorption - did not show significant correlation with embrittlement for either of the reactors.

It should be emphasized that our results should be considered preliminary. Even though our measurements spanned a much larger set of specimens than any other work up to now, it is still possible that conclusions could change if a still larger number of specimens were evaluated. Only three fluences were available for each reactor and only five specimens per fluence level were evaluated. More specimens are still available at SwRI per fluence level, but the DC Cook 1 reactor is the only other reactor for which we have specimens at three different fluence levels. It would be useful if specimens could be measured for perhaps five fluence levels for one reactor. A fit to five fluence levels would serve as a very good test for correlation with embrittlement. At our facility, however, we do not have specimens from one reactor at five different fluence levels.

An important point is that all our tests were done on broken Charpy samples. The Charpy impact itself should have an effect on magnetic properties, owing to the introduction of residual stresses. To test for correlation of magnetic properties with embrittlement itself, it would be better to work with unbroken Charpy samples which have been irradiated to measured fluence levels but which have not been subject to Charpy impact. All of the magnetic parameters investigated might be very much affected by impact and fracture.

In addition, the specimens were never characterized magnetically prior to irradiation. If the original magnetic data were available for each Charpy specimen, it would have been much easier to check for correlation of magnetic properties with embrittlement.

Our recommendations for future experiments therefore are to further investigate in the following way:

(1) Check correlation of embrittlement with magnetic properties, using
   a) more samples per fluence level,
   b) more fluence levels per reactor,
   c) more reactors.

(2) Run tests on unbroken irradiated Charpy specimens.

(3) If possible, find a reactor set for which unbroken, unirradiated Charpy specimens are set aside as a control.

(4) If possible, use unbroken irradiated Charpy specimens that were characterized magnetically prior to irradiation.

The issue as to whether magnetic measurements can characterize neutron embrittlement can only be clearly settled if recommendations (2), (3), and (4) are followed.

IV. THEORETICAL RESULTS

Modeling concentrated on the nonlinear harmonics technique and on the Barkhausen technique, since these were the magnetic measurement techniques that seemed to offer the most promise for neutron embrittlement detection. A model for each technique was employed in connection with the basic magnetomechanical hysteresis model.[6,7,16,42,43]

A. Nonlinear Harmonics

The basic model for the third order nonlinear harmonics amplitude had been developed previously by us.[16] The model can be summarized as follows.

Using the magnetomechanical hysteresis model,[43] the total magnetization is evaluated for a sinusoidally varying magnetic field $H(t)=H_{max}\sin \omega t$ at successive time increments. The resulting points trace out an initial magnetization curve followed by a hysteresis loop. The points on the hysteresis loop are fitted, using a least-squares Newton-Raphson fitting procedure,[44] to the expression

$$M(t) = m_1 \sin(\omega t + \theta_1) + m_3 \sin(3\omega t + \theta_3), \tag{1}$$

where parameters m_1 and m_3 represent the first and third order harmonic amplitudes of the magnetization and θ_1 and θ_3 represent the phase angles of the harmonics relative to the phase of the external field H(t). Of the four parameters m_1, m_3, θ_1 and θ_3, only two are free to vary in the fit. The other two are fixed by the constraints that

$$(1)\ B_{max} = \mu_o (H_{max} + M_{max}), \tag{2a}$$

$$(2)\ dM/dt = 0 \ \textit{for}\ t = \tau/4,\ 3\tau/4,\ 5\tau/4,\ \textit{etc}, \tag{2b}$$

where $\tau = 2\pi/\omega$ is the period of time variation of the first harmonic (of fundamental). In order for the second constraint to be appropriate, the hysteresis loop must be taken to an H_{max} well beyond the H corresponding to the knee of the magnetization curve. With the constraints, the Newton-Raphson fit reduced to a two-parameter fit. The corresponding harmonic amplitudes b_1 and b_3 in the flux density B can then be computed from m_1, m_3, θ_1 and θ_3. In some cases, the system must be cycled twice before it settles into a steady loop. In all cases, the harmonic amplitudes are computed from the steady loop.

Since neutron irradiation is known to produced dislocation climbing and vacancy clusters in the embrittled material,[45-48] numerical modeling concentrated on changes in the material parameters of the magnetomechancial hysteresis model and their effect on the harmonic amplitudes. In the experimental results, the harmonic amplitudes increased with embrittlement, in the case of the Indian

Point steel Charpy samples. The study here was to see if the increase in the harmonic amplitudes could be correlated with changes in the material parameters.

The effects of variation of four different parameters were investigated. The four parameters were M_s (saturation magnetization in A/m), c (the ratio of the slopes of the initial magnetic susceptibility to the anhysteretic magnetic susceptibility), k/μ_o (the pinning parameter, in A/m) where the pinning parameter is known to be proportional to the density of pinning sites), and *a* (where *a* is proportional to domain density in the unmagnetized state).

Fig. 29 shows harmonic amplitudes computed with the model for an 8 Hz signal with H_{max} = 15 kA/m and with elastic and magnetoelastic constants for the material given as $c_{11} = 1.26 \times 10^4$ kN/cm^2, $c_{12} = 0.48 \times 10^4$ kN/cm^2 and b = -0.242 kN/cm^2 (appropriate to iron). In Fig. 29, the top two plots are for the (a) third order and (b) first order amplitudes b_3 and b_1 respectively as a function of k/μ_o, with families of curves shown for different values of *a*, and with values of c = 0.1 and $M_s = 1.0 \times 10^6$ A.m. The bottom plots are for b_3 and b_1 vs. k/μ_o for families of different *a*, but with M_s now changed to 1.25×10^6 A/m. The effect of increasing M_s is to increase the harmonic amplitudes. The effect of decreasing *a* (and hence domain density in the unmagnetized state) is to increase the harmonic amplitudes. Variation with k/μ_o is more complicated. At smaller values of *a*, the harmonic amplitudes increase as k/μ_o (and hence density of pinning sites) decreases. When *a* is large enough, a maximum in the third order harmonic amplitude is reached when k/μ_o gets small enough, and for smaller k/μ_o, the third order amplitude decreases.

Fig. 30 shows computed harmonic amplitudes, this time for c = 0.4, but with all else the same as in Fig. 29. Changes with respect to c are relatively small and nonmonotonic. The first order harmonic amplitude increases slightly with increase in c, but the third order amplitude, in the case of $a > 4500$ A/m, decreases.

As seen in Fig. 31, plots of the harmonic amplitudes against *a* exhibit the inverse behavior mentioned earlier, with the amplitudes decreasing as the parameter *a* increases.

Other plots for $M_s = 1.50 \times 10^6$ A/m and 1.75×10^6 A/m display similar behavior to that already mentioned above.

Physically, this would appear to suggest that if harmonic amplitudes increase with embrittlement, then this could be due to several effects - (1) increase of saturation magnetization M_s, (2) decrease in domain density in the unmagnetized state, or (3) decrease in pinning site density. If competing changes in these physical quantities occur due to embrittlement, as might be the case in the SA533B steel of the D C Cook 2 reactor, then the result might be that little change occurs in the harmonic amplitudes.

At this writing, it is not clear how the production of vacancy clusters and of dislocation climbing could produce lower domain densities and smaller pinning site densities; however, the following speculation is offered. If the clustering of vacancies into voids promotes reduction of the number of pinning sites, both pinning site densities and domain densities could decrease. Such a reduction would occur if at reactor temperatures, the vacancy clusters tend to migrate to grain boundaries. The process would be similar to what happens in creep damage[49] in which vacancy clusters migrate from grain interiors to the grain boundaries to produce cavitation and voids at the

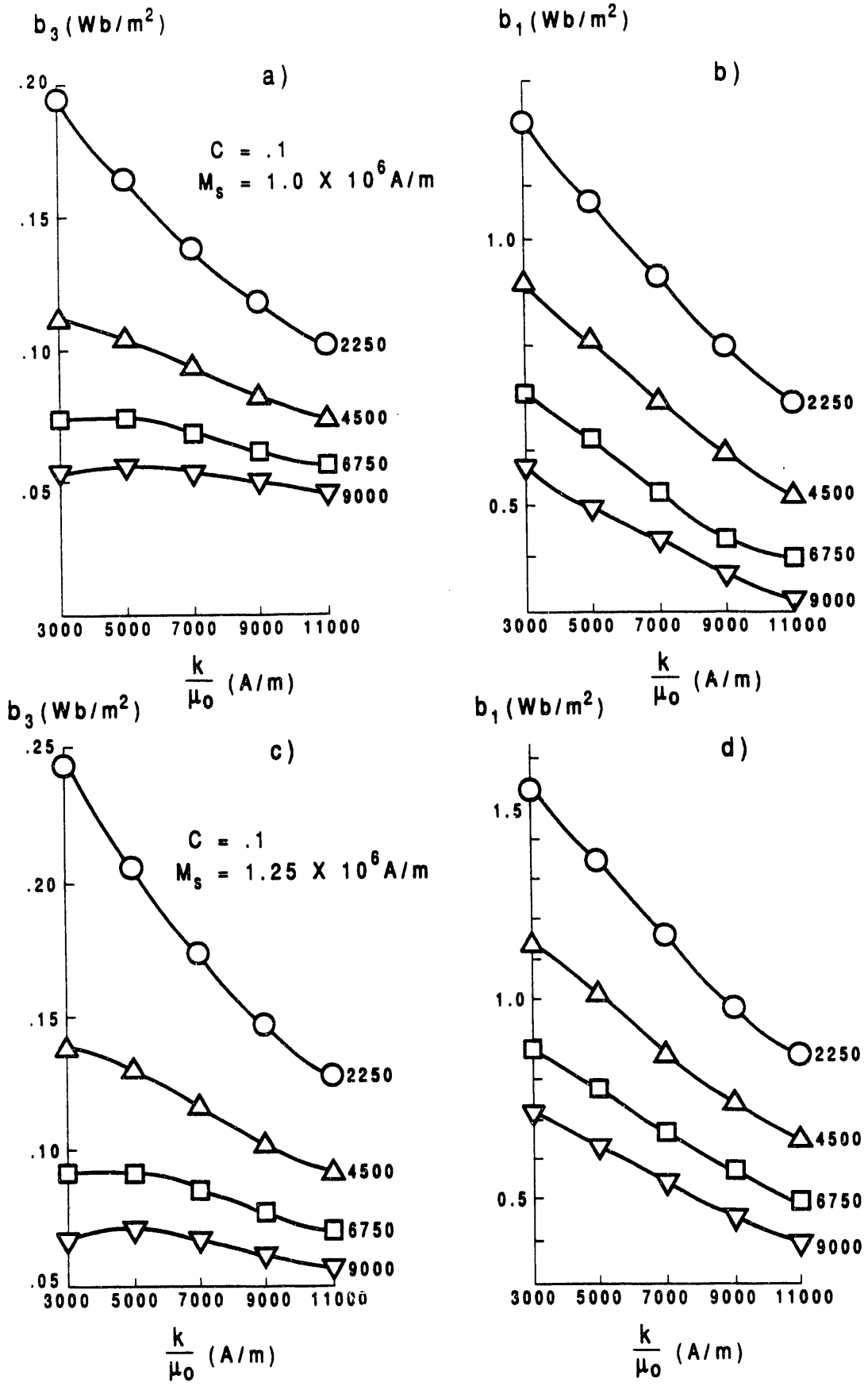

Fig. 29. Computed harmonic amplitudes vs. pinning constant k/μ_o. The top two plots are for the (a) third order and (b) first order harmonic amplitudes b_3 and b_1 respectively for the case of initial susceptibility ratio parameter c = 0.1 and saturation magnetization $M_s = 1.0 \times 10^6$ A/m. The different curves are for different values (in A/m) of effective field normalization parameter *a*. The bottom plots show (c) b_3 and (d) b_1 for c = 0.1, $M_s = 1.25 \times 10^6$ A/m. An 8 Hz signal with H_{max} = 15 kA/m is used for this computation.

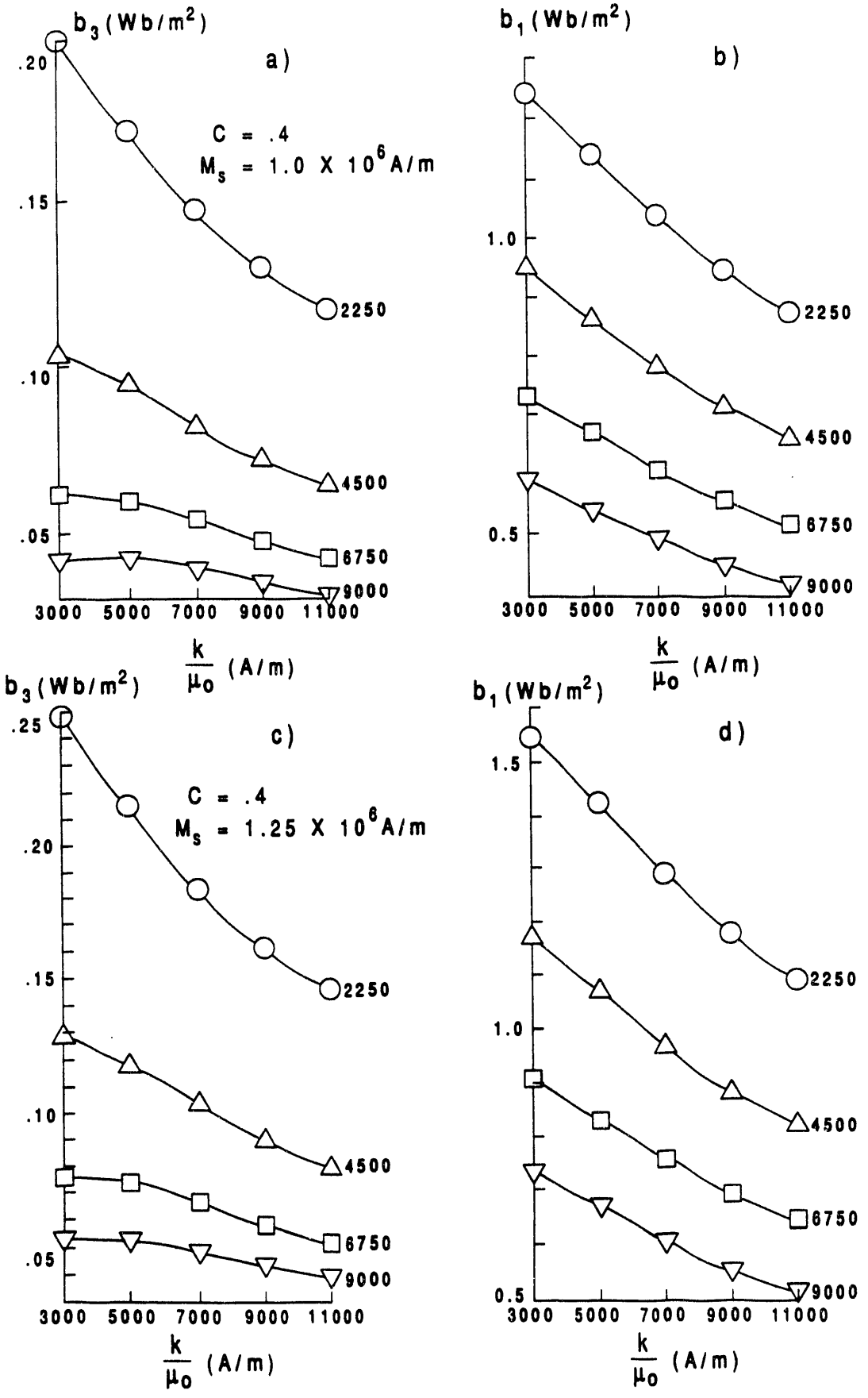

Fig. 30. Computed harmonic amplitudes vs. k/μ_o, but his time for c = 0.4, with all else the same as before.

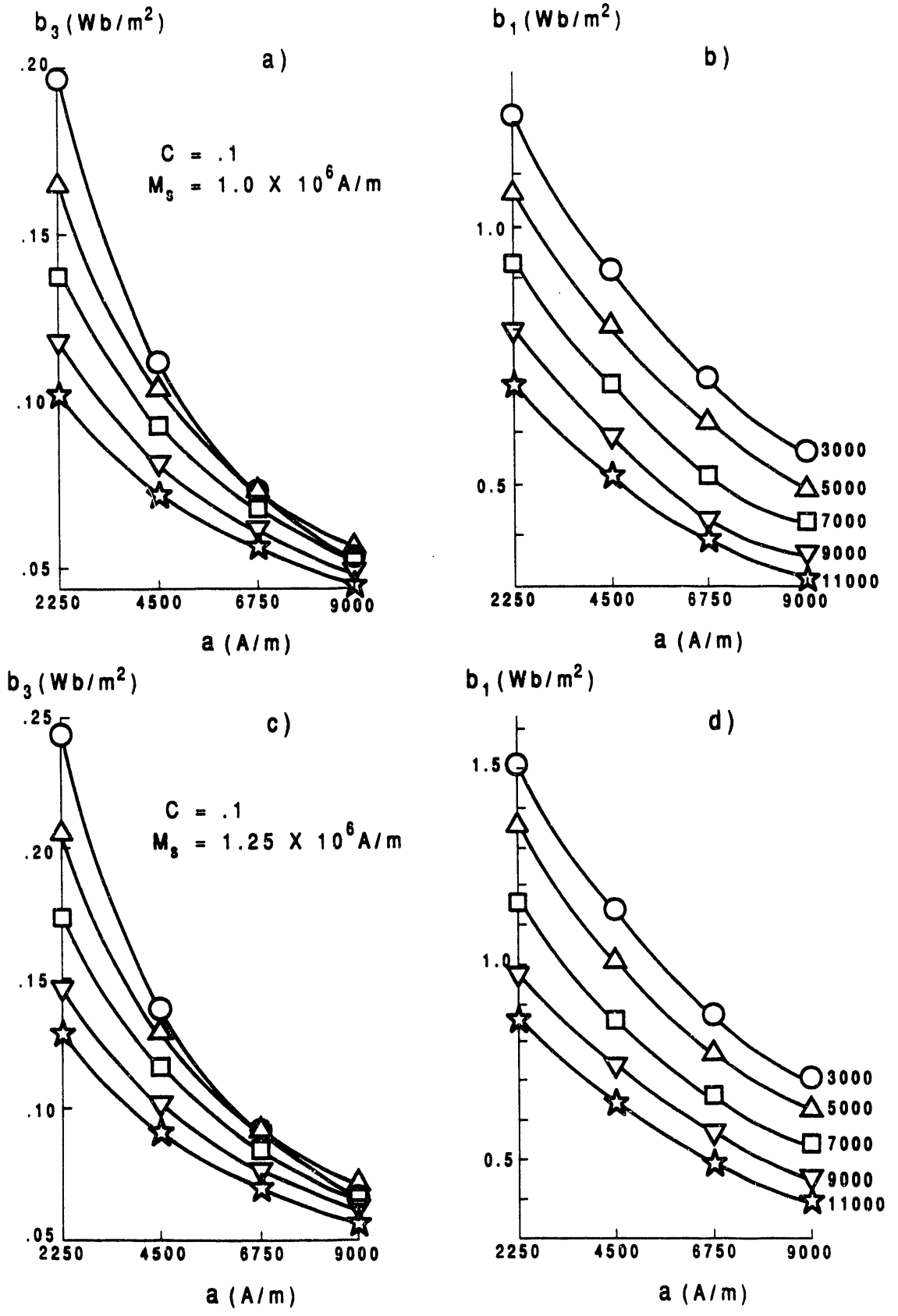

Fig. 31. Computed harmonic amplitudes vs. effective field normalization parameter *a*. Third order amplitudes are on the left and first order amplitudes are on the right. The different curves in each plot are for different values of k/μ_o (in A/m). Top curves are for c = 0.1, $M_s = 1.0 \times 10^6$ A/m; bottom curves are for c=0.1, $M_s = 1.25 \times 10^6$ A/m. An 8 Hz signal with H_{max} = 15 kA/m is again used.

grain boundaries.

B. Barkhausen Noise Amplitudes

The model for Barkhausen noise amplitudes devolves from the model of Alessandro et al[50,51] for the Barkhausen power spectral function, which is given as

$$F(\omega) = 4S\dot{M}_{irr}A\left(\frac{\rho}{G}\right)^2 \frac{\omega^2}{(\omega^2+\tau^{-2})(\omega^2+\tau_c^{-2})} \tag{3}$$

where, using a statistical description, it is assumed that domain walls move across a wide metallic slab of thickness d and cross-section S. The dimensionless coefficient G = 0.1356, provided that [52] the slab is wide enough that $S>>d^2$. In eq. (3), ρ is the electrical resistivity, ω is the angular frequency, and A is a parameter that is a measure of short-range domain wall interactions.[50,51] The time constants, τ and τ_c, are given as

$$\tau = GS\mu_{irr}/\rho, \tag{4a}$$

$$\tau_c = \xi/S\dot{M}_{irr}, \tag{4b}$$

where τ_c governs the decay of local coercive field correlations, and ξ is the corresponding correlation length. Barkhausen noise is caused by domain wall motion, which specifically produces changes not in the total magnetization but in the irreversible part of the magnetization. Therefore, the part of the magnetic permeability that enters into eq. (4a) is the irreversible part. Similarly, the time rate of change of magnetization M_{irr} involves only the irreversible part of the magnetization, namely

$$\dot{M}_{irr} = (\mu_{irr} - \mu_o)\dot{H}/\mu_o. \tag{5}$$

If a ramp function is used to generate the Barkhausen data, then $\dot{H}$ is constant. By defining

$$\gamma = S\dot{M}_{irr}(G/\rho)^2/A\tau, \tag{6}$$

and by using eq. (4b), the expression F(ω) can be further written as:

$$F(x) = 4\left(\frac{\xi^2\tau}{\gamma\tau_c^2}\right)\frac{x^2}{\left[1+\left(\frac{\tau^2}{\tau_c^2}\right)x^2\right](1+x^2)} \tag{7}$$

where $x = \omega\tau_c$.

To obtain the Barkhausen pulse amplitude in units of power, one writes:[53]

$$I_B = \frac{1}{2\pi}\int_0^\infty F(\omega)\,d\omega = \frac{1}{2\pi\tau_c}\int_0^\infty F(x)\,dx, \tag{8}$$

$$= \left(\frac{\xi^2}{\gamma\tau\tau_c}\right)[1/(1+(\tau_c/\tau))], \tag{8a}$$

$$= \left(\frac{A\xi}{(G/\rho)^2}\right)\frac{\frac{\mu_{irr}}{\mu_o}(\mu_{irr}-\mu_o)\dot{H}}{\frac{\mu_{irr}}{\mu_o}(\mu_{irr}-\mu_o)\dot{H}+[\xi/(S^2G/\rho)]} \tag{8b}$$

The dependence of I_B on H enters through permeability μ_{irr} (H), since $\dot{H}$ is constant. As noted in the paper in Appendix C, the Barkhausen pulse power amplitude peaks when μ_{irr} peaks. The peak in the irreversible part of the permeability μ_{irr} occurs at a larger H than that of the total permeability μ. Hence, Barkhausen noise amplitudes peak at H larger than the H at which the total permeability peaks.

Fig. 1 in the paper in Appendix C shows modeling results for the Barkhausen pulse power amplitude as a function of H and compares that result to that of the total permeability vs. H. A similar comparison but for experimental data may be found in Bozorth.[54] The model is seen to produce behavior which is seen also in the experimental data.

In this project, the focus was on how the Barkhausen pulse power amplitude behaves as a function of material parameters M_s, c, k/μ_o, and a. Plotted as a function of these parameters were two different quantities - (a) the magnitude $(BN)_{max}$ of the Barkhausen power amplitude maximum and

(b) $H_{max}^{(BN)}$, the field values at which the Barkhausen maximum occurs. The two quantities turn out to be independent of c because c affects only the behavior of the total permeability and not the irreversible part of the permeability, and the Barkhausen power amplitude depends not on the total permeability, but only the irreversible part of the permeability.

In our numerical calculations of the Barkhausen power amplitude, we have used $\sigma = 1/\rho = 2x10^7\ \Omega^{-1}m^{-1}$, $\xi = 3x10^{-2}$ A•m, $S = 1x10^4 m^2$, $\dot{H} = 1910$ (A/m)/sec, and $A = 4.15x10^7\ A^2m^{-3}\ Wb^{-1}$ sec. The elastic and magnetoelastic constants are the same as for the harmonic amplitudes.

Fig. 32 displays computed plots of (a) $(BN)_{max}$ vs. a, (b) $H_{max}^{(BN)}$ vs. a, (c) $(BN)_{max}$ vs. k/μ_o, and (d) $H_{max}^{(BN)}$ vs. k/μ_o, with families of curves appropriately labeled, for the case of $M_s = 1.0x10^6$ A/m. Fig. 33 displays the same kinds of plots for $M_s = 1.5x10^6$ A/m. The figures reveal interestingly that $H_{max}^{(BN)}$ is independent of M_s as well as c. Another trend is that the Barkhausen amplitude $(BN)_{max}$ increases with increasing M_s, with the larger values of k and a exhibiting much larger increases of $(BN)_{max}$ with M_s than the smaller values of k and a. The general tendency is for $(BN)_{max}$ to decrease with increasing k and a and constant M_s, and for $H_{max}^{(BN)}$ to increase with increasing k and a.

Since increasing pinning site density (increasing k/μ_o) and increasing domain density (increasing a) will result in smaller magnetization changes produced by each domain wall motion, it is reasonable that the Barkhausen noise amplitude tends to decrease with increasing k/μ_o and a. For the same reason, the peak should spread and move to a higher maximum value $H_{max}^{(BN)}$ with increasing pinning site density (k/μ_o) and increasing domain density (a). Higher M_s should produce larger magnetization changes with each domain wall motion at constant k/μ_o and a, and hence the Barkhausen amplitude $H_{max}^{(BN)}$ should be larger.

It was suggested earlier that neutron embrittlement reduces pinning site density (viz. k/μ_o) and domain density (viz. a). The above plots suggest therefore that the Barkhausen amplitude should increase with embrittlement, a trend that was seen in the Indian Point data.

As noted however in the earlier discussion of the experimental data, the Barkhausen measurements will tend not to be as reliable as the harmonic amplitudes because of the sensitivity of the Barkhausen measurement to surface conditions. (See Section C.1.a.)

C. Modeling Conclusions

The magnetomechanical hysteresis modeling is able to account for the general trends seen in the dependence of harmonic amplitude and Barkhausen amplitudes on embrittlement. However, mathematical details of the microstructural relationships between neutron damage and material parameters contributing to magnetic changes need to be yet further developed and elucidated.

One of the insights deduced from the modeling is the possible relationship of neutron embrittlement to creep damage. The neutrons are known to produce vacancy clusters.[45-48] These vacancy clusters at reactor temperatures and over a long period of time would tend to migrate to grain

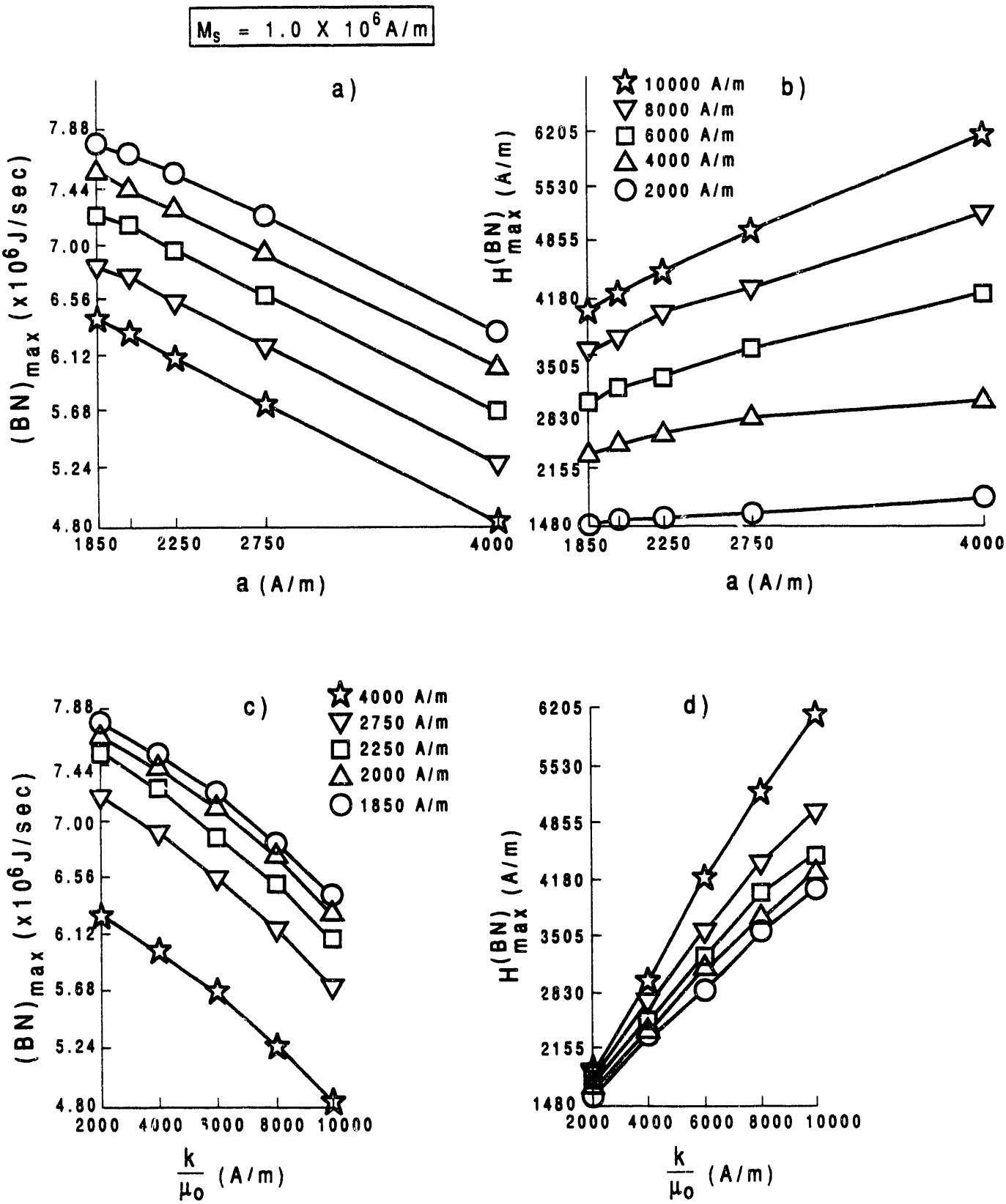

Fig. 32. Computer plots of (a) $(BN)_{max}$ vs. *a*, (b) $H^{(BN)}_{max}$ vs. *a*, (c) $(BN)_{max}$ vs. k/μ_o, and (d) $H^{(BN)}_{max}$ vs. k/μ_o for the case of M_s = 1.0x10^6 A.m. The top plots show curves parameterized for different values of k/μ_o; the bottom plots show curves for different *a*. Curves do not depend on c. Barkhausen model parameters used are listed in the text.

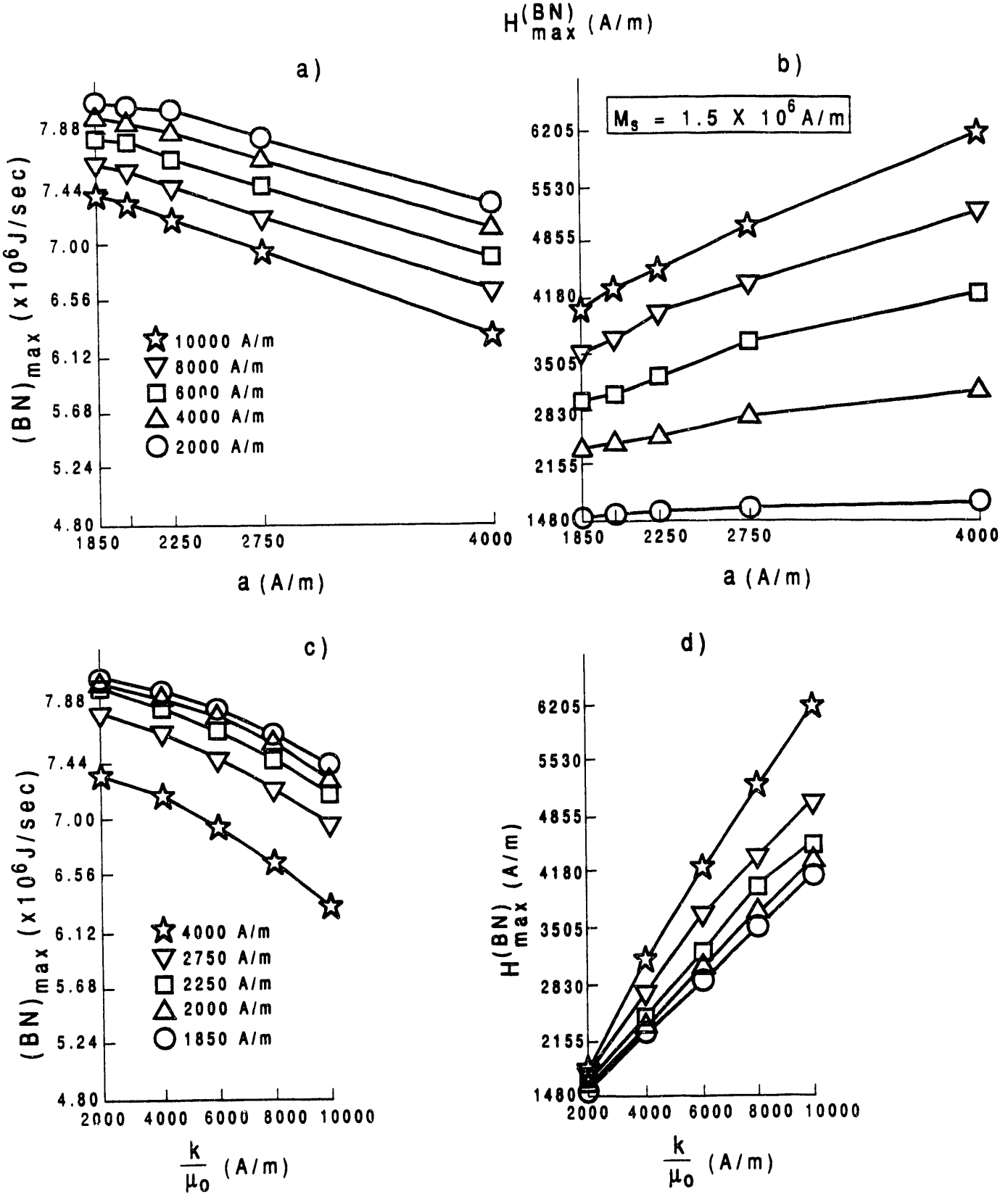

Fig. 33. Same plots as in Fig. 32, but for $M_s = 1.5 \times 10^6$ A/m.

boundaries, producing a reduction in pinning site densities and domain densities, and a resultant increase in Barkhausen noise amplitudes and nonlinear harmonic amplitudes. The increase in amplitudes is seen in the experimental data that we have accumulated on the Indian Point specimens. The migration of vacancy clusters to grain boundaries also occurs in creep damage in steam pipes, in which cavitation and void clustering is seen at grain boundaries in pipes operating at steam temperatures over a long period of time. Creep-damaged pipes are also known to be increased in embrittlement, just as is the case with the neutron-irradiated steels. It thus appears likely that magnetic procedures for detecting creep damage ought to also be applicable to detecting neutron embrittlement.

REFERENCES

1. L.E. Steele, "Neutron Irradiation Embrittlement of Reactor Pressure Vessel Steels," Nuclear Safety 17, 327 (1976).

2. D.G. Cadena, Jr., "Neutron Embrittlement of Steels in Nuclear Pressure Vessels," Nondestr. Test. Eval. 6, 95 (1991).

3. ASTME 185-79, "Standard Recommended Practice for Surveillance Tests for Nuclear Reactor Vessels," 1981 Annual Book of ASTM Standards.

4. G.L. Burkhardt, H. Kwun, A.E. Crouch, and D.A. DesNoyer, "Review of Stress Measurement Techniques for Pipelines," in Damage Assessment, Reliability, and Life Prediction of Power Plant Components, ed. R.N. Pangborn (ASME, 1990), PVP, Vol. 193/NDE, Vol. 8, from Proc. Pressure Vessels and Piping Conference, Nashville TN (June 1990), pp. 95-103.

5. Patrick Porter, Vetco Pipeline Services, Houston, TX, private communication

6. M.J. Sablik, "Modeling Stress Dependence of Magnetic Properties for NDE of Steels," Nondestructive Testing and Evaluation 5, 49 (1989).

7. M.J. Sablik and H. Kwun, "Hysteretic Model for Barkhausen Noise and the Magnetically Induced Velocity Change of Ultrasonic Waves in Ferromagnets Under Stress," J. Appl. Phys. 69, 5791 (1991).

8. H. Kwun and G.L. Burkhardt, "Electromagnetic Techniques for Residual Stress Measurements," in Metals Handbook Vol. 17, Nondestructive Evaluation and Quality Control, ed. S.R. Lampman and T.B. Zorc (ASM International, 1989) pp. 159-163.

9. W.L. Rollwitz, "Magabsorption NDE," in Metals Handbook, Vol. 17, Nondestructive Evaluation and Control, ed. S.R. Lampman and T.B. Zorc (ASM International, 1989), pp. 143-158.

10. D.C. Jiles, "Review of Magnetic Methods for Nondestructive Evaluation," NDT International 21, 311 (1988).

11. H. Kwun and G.L. Burkhardt, "Effects of Grain Size, Hardness, and Stress on the Magnetic Hysteresis Loops of Ferromagnetic Steels," J. Appl. Phys. 61, 1576 (1987).

12. M.J. Sablik, H. Kwun, G.L. Burkhardt, and D.C. Jiles, "A Model for the Effect of Tensile and Compressive Stress on Ferromagnetic Hysteresis," J. Appl. Phys. 61, 3799 (1987).

13. H. Kwun and G.L. Burkhardt, "Effects of Stress on the Harmonic Content of Magnetic Induction in Ferromagnetic Material," Proc. 2nd Natl. Seminar on NDE of Ferromagnetic Materials, Houston TX (March 1986), available from Dresser Industries, Houston TX.

14. H. Kwun and G.L. Burkhardt, "Nondestructive Measurement of Stress in Ferromagnetic Steels Using Harmonic Analysis of Induced Voltage," NDT International 20, 167 (1987).

15. G.L. Burkhardt and H. Kwun, "Application of the Nonlinear Harmonics Method to Continuous Measurement of Stress in Railroad Rail," in Proc. of the 1987 Review of Progress in Quantitative NDE, Vol. 7B, ed. D.O. Thompson and D.E. Chimenti (Plenum Press, 1988), p. 1413.

16. M.J. Sablik, G.L. Burkhardt, H. Kwun, and D.C. Jiles, "A Model for the Effect of Stress on the Low-Frequency Harmonic Content of the Magnetic Induction in Ferromagnetic Materials," J. Appl. Phys. 63, 3930 (1988).

17. R.L. Pasley, "Barkhausen Effect -- An Indication of Stress," Mater. Eval. 28, 157 (1970).

18. J.C. McClure, Jr., and K. Schroder, "The Magnetic Barkhausen Effect," CRC Crit. Rev. Solid State Sci. 6, 45 (1976).

19. G.A. Matzkanin, R.E. Beissner, and C.M. Teller, "The Barkhausen Effect and Its Applications to Nondestructive Evaluation," State of the Art Report, NTIAC-79-2, Nondestructive Testing Information Analysis Center, Southwest Research Institute (1979).

20. H. Kwun, "Investigation of the Dependence of Barkhausen Noise on Stress and the Angle Between the Stress and Magnetization Directions," J. Magn. Magn. Mater. 49, 235 (1985).

21. G.L. Burkhardt and H. Kwun, "Measurement of Residual Stress Around a Circular Patch Weld Using Barkhausen Noise," in Rev. Progr. in Quantitative NDE, ed. D.O. Thompson and D.E. Chimenti (Plenum, NY, 1989), Vol 8A, pp. 1053-1060.

22. H. Kwun and C.M. Teller, "Tensile Stress Dependence of Magnetically Induced Ultrasonic Shear Wave Velocity Change in Polycrystalline A-36 Steel," Appl. Phys. Lett. 41, 144 (1982).

23. H. Kwun and C.M. Teller, "Stress Dependence of Magnetically Induced Velocity Change in Polycrystalline A-36 Steel," J. Appl. Phys. 54, 4856 (1983).

24. H. Kwun, "Effects of Stress on Magnetically Induced Velocity Changes for Ultrasonic Longitudinal Waves in Steels," J. Appl. Phys. 57, 1555 (1985).

25. H. Kwun, "A Nondestructive Measurement of Residual Bulk Stresses in Welded Steel Specimens by Use of Magnetically Induced Velocity Changes for Ultrasonic Waves," Mater. Eval. 44, 1560 (1986).

26. H. Kwun, "Measurement of Stress in Steels Using Magnetically Induced Velocity Changes for Ultrasonic Waves," in Nondestructive Characterization of Materials II, ed. J.F. Bussiere, J.R. Monchalin, C.O. Ruud, and R.E. Green, Jr. (Plenum Press, 1987), p. 633.

27. M. Namkung and D. Utrata, "Nondestructive Residual Stress Measurements in Railroad Wheels Using the Low-Field Magnetoacoustic Test Method", in Proc. 1987 Review of Progress in Quant. NDE, ed. D.O. Thompson and D.E. Climenti (Plenum Press, 1988), p. 1429.

28. M.J. Sablik, W.L. Rollwitz, and D.C. Jiles, "A Model for Magabsorption as an NDE Tool for

Stress Measurement," In Proc 17th Symposium on NDE, San Antonio, TX, Apr 17-20, 1989, ed. F.A. Iddings (NTIAC, Southwest Research Institute, San Antonio, TX 1989), p. 212-223.

29. D.J. Buttle, G.A.D. Briggs, J.P. Jakubovics, E.A. Little, and C.B. Scruby, "Magnetoacoustic and Barkhausen Emission in Ferromagnetic Materials," Phil. Trans. Roy. Soc. London A320, 363 (1986).

30. D.J. Buttle, E.A. Little, C.B. Scruby, G.A.D. Briggs, and J.P. Jakubovics, "A Study of Neutron Irradiation Damage in α-Iron with Magnetoacoustic and Barkhausen Emission," Proc. Roy. Soc. London A414, 221 (1987).

31. E.A. Little, D.J. Buttle, and C.B. Scruby, "Radiation Damage Studies in Model Ferritic Alloys Using Micromagnetic Techniques," Phys. Stat. Sol. (a) 112, 55 (1989).

32. O.Y. Kwon and K. Ono, "Detection of Irradiation Effects on Reactor Vessel Steels by Magneto-Acoustic Emission," J. Acoust. Emiss. 9 (4), 227 (1990).

33. J.R. Barton and R.D. Wylie, "Development of Nondestructive Testing Instrumentation for Reactor Pressure Vessels," Sixth Quarterly Report, Contract No. AT(11-1)-1243, prepared for Joint US/Euratom Research and Development Program (July 1964).

34. M.S. Wechsler and R.G. Berggren, "Radiation Embrittlement of Reactor Pressure Vessels," Nuclear Safety 4, 42 (1962).

35. M.K. Devine, D.C. Jiles, P.K. Liaw, R.D. Rishel and D.S. Drinon, "Magnetic Property Changes in Various Structural Steels due to Irradiation," presented at the Quantitative NDE Conf., La Jolla, CA, July 1992.

36. A. Zentko, M. Timko, and P. Duhaj, "Effect of Neutron Irradiation on the Magnetic Properties of Amorphous $Fe_{47}Ni_{25}B_{18}Si_{10}$ Alloys," Phys. Stat. Sol. (a) 66, K125 (1981).

37. R.D. Brown, J.R. Cost, and J.T. Stanley, "Irradiation-Induced Decay of Magnetic Permeability of Metglas 26055-3 and Mumetal," J. Nucl. Mater. 131, 37 (1985).

38. H. Soffel, "The Effect of Radiation with Fast Neutrons on the Saturation Remanence of a Basalt," Z. fur Geophysik 37, 519 (1971).

39. D.J. Buttle, Harwell Research Laboratory, private communication.

40. L.E. Steele, "Radiation Embrittlement of Reactor Pressure Vessels," Nucl. Eng. Des. 3, 287 (1966).

41. ENDF/B-IV, Dosimetry Tape 412, Mat. No. 6417 (26-Fe-54), July 1974, and L.E. Steele and C.Z. Serpan, Jr., "Analysis of Reactor Pressure Vessel Effects Surveillance Programs," ASTM STP 481, Dec. 1970.

42. M.J. Sablik and S.W. Rubin, "Relationship of Magnetostrictive Hysteresis to the ΔE Effect," J. Magn. Magn. Mater. 104-7, 392 (1992).

43. See Appendix A of the original proposal for this project, "Application of Magnetomechanical Hysteresis Modeling to Magnetic Techniques for Monitoring Neutron Embrittlement and Biaxial Stress.", M.J. Sablik, H. Kwun, W.L. Rollwitz, and D. Cadena, Proposal No. 15-9841, Southwest Research Institute.

44. D.D. McCracken and W.S. Dorn, Numerical Methods and Fortran Programming (Wiley, NY, 1968), p. 133.

45. A. Kohyama, K. Asakura, Y. Kohno, K. Komamura, K. Suziki, M. Kiritani, T. Fujita, and N. Igata, "Low Fluence Neutron Irradiation Response of Ferritic Stainless Steels," J. Nucl. Mater. 133 & 134, 628 (1985).

46. K. Kitajima, E. Kuramoto, and N. Yoshida, "Correlation Among Damage Structures Irradiated with Cascades of Various PKA Energy Spectra," J. Nucl. Mater. 108 & 109, 267 (1982).

47. J.L. Straalsund, R. W. Powell and B.A. Chin, "An Overview of Neutron Irradiation Effects in LMFBR Materials," J. Nucl. Mater. 108 & 109, 299 (1982).

48. P.J. Maziasz, D.N. Braski, J.M. Vitek, F.W. Wiffen, R. L. Klueh, M. L. Grossbeck, and E. E. Bloom, "Progress in Alloy Development in the Fusion Materials Program," J. Nucl. Mater. 108 & 109, 296 (1982).

49. Private communication, S.B. Biner, Iowa State Univeristy.

50. B. Alessandro, C. Beatrice, G. Bertotti, and A. Montorsi, "Domain Wall Dynamics and Barkhausen Effect in Metallic Ferromagnetic Materials. I. Theory," J. Appl. Phys. 68 (6), 2901 (1990).

51. B. Alessandro, C. Beatrice, G. Bertotti, and A. Montorsi, "Domain Wall Dynamics and Barkhausen Effect in Metallic Ferromagnetic Materials. II. Experiments," J. Appl. Phys. 68 (6), 2908 (1990).

52. G. Bertotti, "Physical Interpretation of Eddy Current Losses in Ferromagnetic Materials. I. Theoretical Considerations," J. Appl. Phys. 57, 2110 (1985).

53. I.S. Gradshteyn and I.M Ryzhik, Table of Integrals, Series and Products, corrected and enlarged edition by A. Jeffrey (Wiley, NY, 1980), p. 300.

54. R.M. Bozorth, Ferromagnetism (Van Nostrand, Princeton, NJ, 1978), p. 529.

Preprints Removed

APPENDIX 1

Linear Correlation Coefficient

Appendix 1

Linear Correlation Coefficient

Consider n number of samples for the two parameters X and Y which are $(X_1, Y_1), (X_2, Y_2), \ldots$, and (X_n, Y_n). The linear correlation coefficient R between the two parameters is defined by

$$R = \frac{\Sigma_i x_i y_i}{(\Sigma_i x_i^2 \Sigma_i y_i^2)^{1/2}} \qquad (1)$$

where Σ_i is the summation over $i = 1$ to n, and x_i and y_i represent the deviations of the ith sample (X_i, Y_i) from the sample mean of the two parameters $(\overline{X}, \overline{Y})$, i.e.

$$x_i = X_i - \overline{X}, \text{ where } \overline{X} = \frac{\Sigma_i X_i}{n}, \text{ and}$$

$$y_i = Y_i - \overline{Y}, \text{ where } \overline{Y} = \frac{\Sigma_i Y_i}{n}. \qquad (2)$$

The linear correlation coefficient R varies between -1 and +1, depending on the closeness of the relationship between the samples. Positive values of R indicate a tendency to have a linear relationship with positive slope. Conversely, negative values of R indicate a tendency to have a linear relationship with a negative slope. When $|R| = 1$, the two parameters are said to be perfectly related. In this case, any change in one parameter is always accompanied by a proportional change in the other. When $R = 0$, two parameters are said to be unrelated. In this case, two parameters vary randomly.

Figure A1 shows examples of scatter diagrams of two parameters with a range of linear correlation coefficients. It can be seen that the higher $|R|$, the smaller the degree of scatter from the lines drawn in the figure. The two lines in each diagram represent a least square fit of the linear relationship between the two parameters. One of the lines (indicated by A) is obtained by assuming the parameter on the Y axis is dependent on the parameter on the X axis, and the other line (indicated by B) by assuming the parameter on the X axis is dependent on the parameter on the Y axis.

Equation (1) can be rewritten as:

$$R = \left[\frac{(\Sigma_i x_i y_i)^2}{(\Sigma_i x_i^2 \Sigma_i y_i^2)} \right]^{1/2}$$

$$= \left[\left(\frac{\Sigma_i x_i y_i}{\Sigma_i x_i^2} \right) \left(\frac{\Sigma_i x_i y_i}{\Sigma_i y_i^2} \right) \right]^{1/2}$$

$$= (b_{xy} b_{yx})^{1/2}$$

where $b_{xy} = \frac{\Sigma_i x_i y_i}{\Sigma_i y_i^2}$ *and*

$$b_{xy} = \frac{\Sigma_i x_i y_i}{\Sigma_i x_i^2}. \qquad (3)$$

Note that b_{yx} is the slope of the least square fitted line obtained by assuming parameter X is a function of parameter Y. Similarly, b_{xy} is the slope of the least square fitted line obtained by assuming parameter Y is a function of parameter X. In statistics, this slope is usually called the linear regression coefficient. Therefore, equation (3) states that the correlation coefficient, R, is the geometric mean of the slope of the two least square fitted lines.

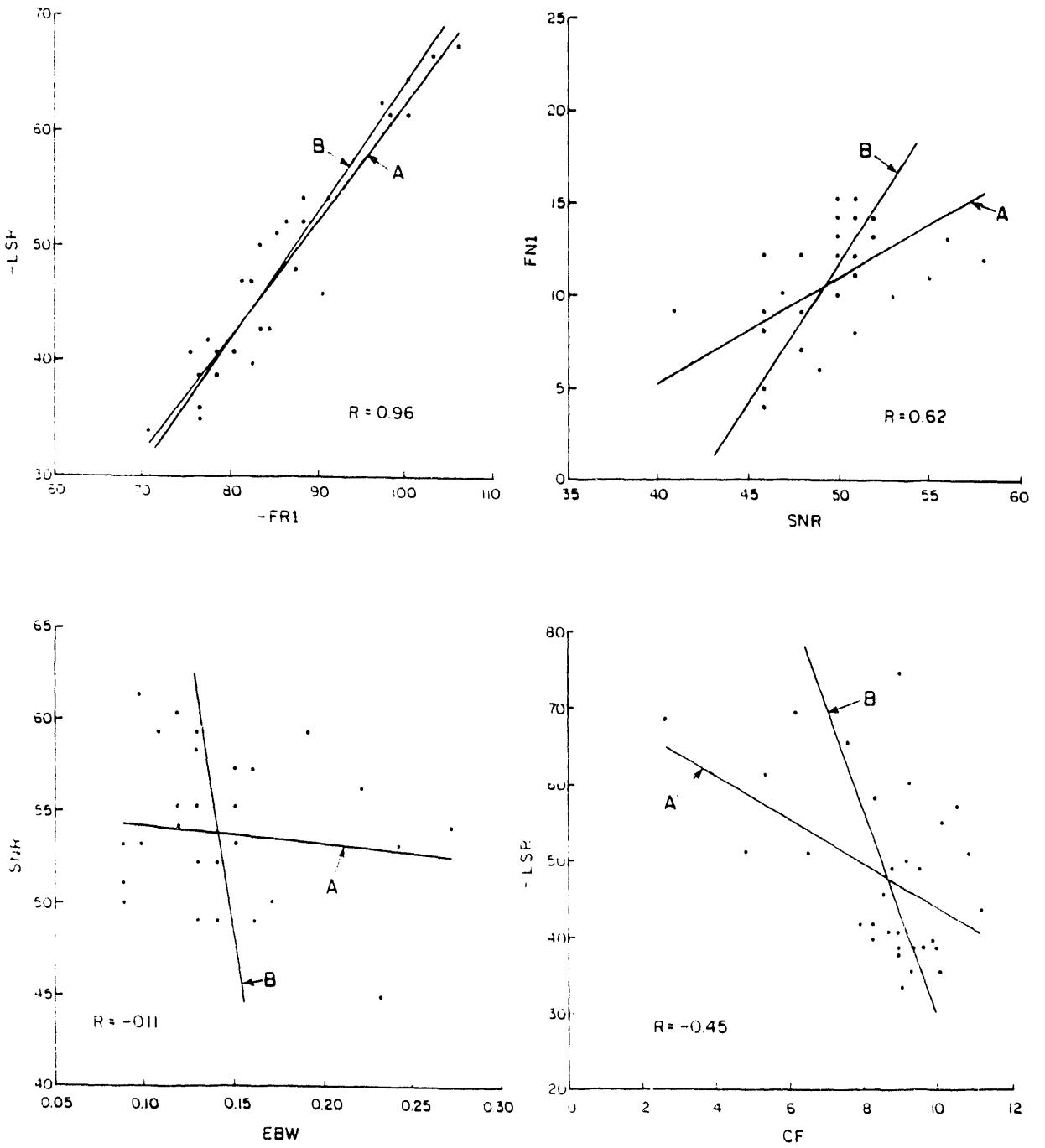

Fig. A1 Examples of scatter plots for data having various R values. R is the linear correlation coefficient. A represents the least square fit line obtained by assuming the parameter of the Y axis is dependent on the parameter of the X axis. B represents the least square fit line obtained by assuming the parameter of the X axis is dependent on the parameter of the Y axis. (Ref. 59).

END

DATE FILMED

5/12/93